eman ta zabal zazu

Universidad del País Vasco
Euskal Herriko Unibertsitatea

Injection, transport and manipulation of pure spin currents in metallic lateral spin valves

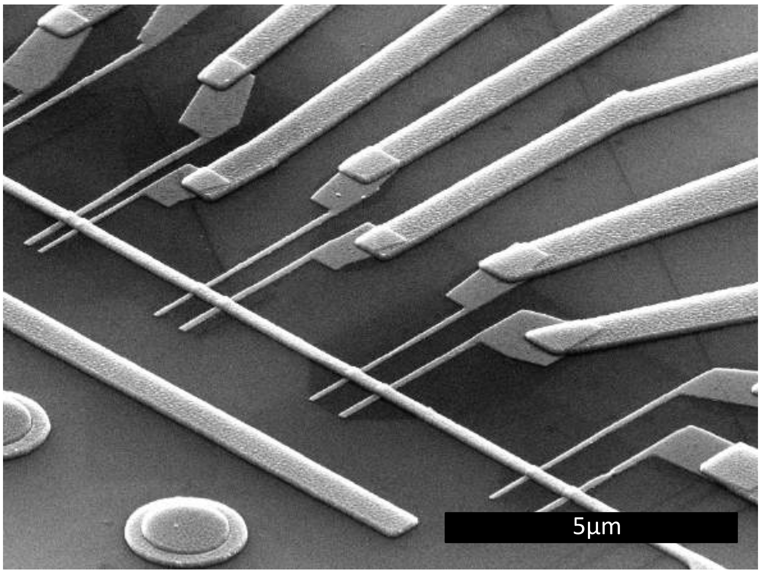

Estitxu Villamor Lomas

PhD Thesis

Supervisor: Prof. Fèlix Casanova

2014

CIC
nanoGUNE
nanoscience cooperative research center

"If I can't dance, it's not my revolution."

Emma Goldman

Laburpena

1947. urtean trantsistorea asmatu zenetik, gailu elektronikoak etengabe ari dira txikitzen, Moore-n legeari jarraituz zirkuitu integratu batean geroz eta unitate logiko gehiago sartu eta hauen data prozesaketa abiadura handituz doalarik. Halere, miniaturizaizo joera honek ezin du betirako iraun, gailu hauek bero moduan disipaturiko energia geroz eta altuagoa baita eta, atomoen tamainara hurbiltzen garen heinean, fluktuazio kuantikoek garrantzia handiagoa baitute. Hau guztia dela eta, aldaketa baten beharra dago eta aukera bat spintronikan datza, hau elektroiaren kargaz baliatzeaz gain bere spin-az ere baliatzen den elektronikaren alor berria izanik.

Spin-a oinarrizko partikulen propietate kuantiko bat da, momentu angeluar intrintseko eta kuantizatu gisa irudika daitekeena, $\vec{S}$. Norabide preferentzial bat dauka, zeinetan balio konkretu batzuk baino ezin dituen hartu, elektroiaren kasuan $S_Z = \hbar/2$ eta $S_Z = -\hbar/2$ direnak, goranzko spin-a eta beheranzko spin-a alegia. Elektroia partikula kargaduna denez, momentu angeluar honi loturiko momentu magnetiko bat du, $\vec{\mu} = -\frac{g_s \mu_B}{\hbar}\vec{S}$, non $\hbar = h/2\pi$ eta h Planck-en konstantea, $g_s \simeq 2$ spinaren g faktorea eta $\mu_B = \frac{e\hbar}{2m}$ Bohr-en magnetoia diren, e eta m elektroiaren karga eta masa izanik. Elektroiaren momentu magnetikoa, atomo batean, nukleoarena baino askoz handiagoa denez, hau da material ferromagnetikoen (FM) magnetizazioaren eragile nagusia. Izan ere, material FM-ek norantza konkretu batean (goruntz edo beheruntz) spin gehiago dituzte. Spin guztien momentu magnetikoen baturak ematen die material FM-ei magnetizazio makroskopikoa, beraz. Truke elkarrekintzaren eraginez, goranzko eta beheranzko elektroiek eroankortasun elektriko desberdinak dituzte, $\sigma_\uparrow$ eta $\sigma_\downarrow$, material FM-en spin polarizazioa eragiten dutenak: $\alpha_F = (\sigma_\uparrow - \sigma_\downarrow)/(\sigma_\uparrow + \sigma_\downarrow)$. Horregatik material FM-ak spin korronteen sorburu elektriko bikainak dira.

Spintronika formalki 80. hamarkadako amaieran sortu zen, magnetoerresistentzia erraldoiaren eskutik (GMR ingelesezko izenetik). Hau multigeruza magnetikoetan, aplikaturiko eremu magnetiko baten aldaketaren ondorioz, sortzen den erresistentzia aldaketa nabarmena da eta 90. hamarkadan merkaturatu ziren disko gogorren irakurgailuen oinarrian dago (ikusi 1.1 atala). GMR-ari jarraitu dion tunel magnetoerresistentziak, ondoren, beste hainbat aplikazio ekarri ditu, hauen artean memoria magnetikoak (MRAM ingelesetik) adibidez.

Nahiz eta teknologikoki hain garrantzitsuak izan, aipatu berri ditugun adibideak polarizatutako karga korronteen garraioan oinarritzen dira. Spintronikaren garapena ordea, bigarren belaunaldiko gailuak sortu eta erabiltzeak ekarriko du. Gailu hauek spin korronte puruak (kargarik gabeak) sortu eta distantzia luzeetan (> 100 nm) garraiatzea dute helburu, errendimendu egoki bat izateko hiru osagai nagusi behar direlarik: (*i*) spin korronte puruen sorrera eta detekzioa, (*ii*) garraioa distantzia luzeetan zehar eta (*iii*) garraiaturiko spin-en manipulazioa.

Hainbat era daude spin korronte hauek sortu edota detektatzeko, ponpaketa optikoa, erresonantzia ferromagnetikoaren bidezko ponpaketa edota spin injekzio termikoa, besteak beste. Halere, elektronika arruntarekin duen bateragarritasuna dela eta, tesi honetan zehar spin injekzio elektrikoan oinarrituko gara, horretarako spin balbula lateralak (LSV-ak ingelesetik) erabiliko ditugularik.

LSV-ak bi elektrodo FM-z eta berauek lotzen dituen kanal ez magnetiko (NM ingelesetik) batez osaturik dauden gailuak dira (ikusi 1.3 irudia), euren geometria ez lokala dela eta, spin korronte puruen sorrera ahalbidetzen dutenak. Gailu hauetan korronte elektriko bat (I) injektatzen da elektrodo FM-etako batetik (injektorea) kanal ez magnetikora (ikusi 1.3 irudia), korrontea FM-an zehar polarizaturik dagoelarik. Material NM-aren elektroiak polarizaturik ez daudenez, spinek erresistentzia bat aurkitzen dute FM-aren eta NM-aren arteko gainazalean, bertan pilaturik gelditzen direlarik desoreka egoera batean. Sistema orekatzeko, pilaturiko spin horiek difusioz injektore FM-aren bi aldeetarantz garraiatzen dira, karga garraiorik ez dugun aldean spin korronte puru bat sortuz (ikusi 2.1 atala). Bigarren elektrodo FM bat jarriz (detektorea), kanal NM-aren eta detektore FM-aren artean spin pilaketa bat sortzen da berriro, voltaia elektriko baten moduan (V_S) neur daitekeena. Voltaia hau, bereziki, material FM-aren spin polarizazioaren (α_F), material NM-aren spin difusio luzeraren (λ_N) eta bi elektrodo FM-en arteko distantziaren (L) menpekoa da, eta dimentsio bakarreko spin difusio ekuazioa ebatziz, berau deskribatzeko ondoko espresioa lor daiteke (testu nagusiko 2.7 ekuazioa):

$$V_S = I \frac{2R_N \left[\frac{P_{I1}}{1-P_{I1}^2} \left(\frac{R_{I1}}{R_N} \right) + \frac{\alpha_{F1}}{1-\alpha_{F1}^2} \left(\frac{R_{F1}}{R_N} \right) \right] \left[\frac{P_{I2}}{1-P_{I2}^2} \left(\frac{R_{I2}}{R_N} \right) + \frac{\alpha_{F2}}{1-\alpha_{F2}^2} \left(\frac{R_{F2}}{R_N} \right) \right] e^{-L/\lambda_N}}{\left[1 + \frac{2}{1-P_{I1}^2} \left(\frac{R_{I1}}{R_N} \right) + \frac{2}{1-\alpha_{F1}^2} \left(\frac{R_{F1}}{R_N} \right) \right] \left[1 + \frac{2}{1-P_{I2}^2} \left(\frac{R_{I2}}{R_N} \right) + \frac{2}{1-\alpha_{F2}^2} \left(\frac{R_{F2}}{R_N} \right) \right] - e^{-2L/\lambda_N}},$$

non $R_N = \rho_N \lambda_N / w_N t_N$ kanal NM-aren spin erresistentzia, $R_{Fi} = \rho_F \lambda_F / w_N w_{Fi}$ injektore ($i = 1$) eta detektore ($i = 2$) FM-en spin errsistentziak eta R_{Ii} FM/NM gainazalen erresistentzia elektrikoak diren. t_N kanal NM-aren lodiera da, w_N eta w_{Fi} kanal NM-aren eta elektrodo FM-en zabalerak dira, λ_F metal FM-aren spin difusio luzera da eta ρ_N eta ρ_F metal NM eta FM-en erresistibitate elektrikoak dira.

Neurtzen dugun voltaia korronte elekrtikoaz normalizatuz, erresistentzia ez lokala deritzoguna lortuko dugu: $R_{NL} = V_S/I$. Elektrodo FM-ekiko paraleloa den eremu magnetikoaren balioa positibotik negatibora aldatuz (ikusi 1.3 irudia), euren magnetizazioa egoera paralelotik (P) antiparalelora (AP) aldatuko da, erresistentzia ez lokalaren zeinu aldaketa eragingo duena (ikusi 2.3 irudia). Modu honetan LSV-en ezaugarria den $R_{NL}(H)$ kurba lortuko dugu. Erresistentzia ez lokalaren balio positiboaren eta negatiboaren arteko desberdintasunari spin seinalea deritzo, ΔR_{NL}.

Gailu bakoitzean hainbat LSV ditugu, FM-en arteko distantzia ezberdinak (L) dituztenak. Horrela, L-rekiko neurturiko spin seinalea 2.7 ekuazioarekin doitu dezakegu α_F eta λ_N-ren balioak lortzeko. Teknika hau oso fidagarria izan arren, badu desabantaila nagusi bat: spin injekzioari eta garraioari buruzko informazioa lortzeko, LSV ugari behar ditugula gailu bakoitzean, euren fabrikazioa eta neurketa tribialak ez direlako (esterako, oso erraza da neurketa elektrikoak egiterakoan elektrodo FM-ak apurtzea, euren dimentsio txikia eta erresistibitate altua dela eta). Hau ekiditeko posible da Hanle efektuaz baliatzea (2.2.1 atala), planoaz kanpoko eremu magnetiko baten menpe spin-ek duten prezesioan oinarritzen dena (ikusi 2.4 irudia). Kanpo eremu magnetiko baten menpean neurtzen den erresistentzia ez lokala honako hau da (2.18 ekuazioa):

$$R_{NL} = \frac{2R_N^{\omega}\left[\frac{P_{I1}}{1-P_{I1}^2}\left(\frac{R_{I1}}{R_N^{\omega}}\right)+\frac{\alpha_{F1}}{1-\alpha_{F1}^2}\left(\frac{R_{F1}}{R_N^{\omega}}\right)\right]\left[\frac{P_{I2}}{1-P_{I2}^2}\left(\frac{R_{I2}}{R_N^{\omega}}\right)+\frac{\alpha_{F2}}{1-\alpha_{F2}^2}\left(\frac{R_{F2}}{R_N^{\omega}}\right)\right]\left(\frac{Re\left[\lambda_N^{\omega}e^{-L/\lambda_N^{\omega}}\right]}{Re\left[\lambda_N^{\omega}\right]}\right)}{\left[1+\frac{2}{1-P_{I1}^2}\left(\frac{R_{I1}}{R_N^{\omega}}\right)+\frac{2}{1-\alpha_{F1}^2}\left(\frac{R_{F1}}{R_N^{\omega}}\right)\right]\left[1+\frac{2}{1-P_{I2}^2}\left(\frac{R_{I2}}{R_N^{\omega}}\right)+\frac{2}{1-\alpha_{F2}^2}\left(\frac{R_{F2}}{R_N^{\omega}}\right)\right]-\left(\frac{Re\left[\lambda_N^{\omega}e^{-L/\lambda_N^{\omega}}\right]}{\left[\lambda_N^{\omega}\right]}\right)^2},$$

non $\lambda_N^{\omega} = \frac{\lambda_N}{\sqrt{1+i\omega_L\tau_{sf}}}$ spin difusio luzera efektiboa den eta $R_N^{\omega} = R_N\mathrm{Re}\left[\lambda_N^{\omega}/\lambda_N\right]$ kanal NM-aren spin erresistentzia efektiboa den. Spin injekzio eta garraioari buruzko informazioa emateaz gain, Hanle efektua spin-ak manipulatzeko tresna erabilgarria da.

Tesi honen helburu nagusia LSV-etan spin injekzioari eta garraioari doagozkien mekanismo nagusiak ulertzea da eta, honetaz baliatuz, spin manipulazio metodo ezagunak (Hanle) sakonkiago aztertzea eta baita spin manipulazio metodo berriak proposatzea ere.

Horretarako, Co/Cu eta Py/Cu LSV-ak erabili ditugu, elektroi kanoi bidezko litografiaz fabrikatu ditugunak (eBL ingelesetik). Teknika hau sustratu batean (normalean Si/SiO$_2$) dagoen polimero baten gainean elektroi kanoi batekin idaztean oinarritzen da, idatzi dugun zonaldean polimeroa ezabatuko delarik eta bertan metala lurrundu dezakegularik. Lagina azetonan sartzen dugunean, polimeroa disolbatuko da, eta zuzenean gure sustratuaren gainean zegoen metala baino ez da geratuko (azalpen zehatz baterako ikusi 3.1 atala eta 3.2 irudia). Gure gailuak fabrikatzeko, bi pausutako litografia prozesua erabili dugu: lehenengo pausuan elektrodo FM-ak fabrikatu ditugu eta bigarrenean kanal NM-a (ikusi 3.1 atala). Bi pausuen artean, elektrodo FM-aren gainazala Ar ioien bidez garbitzea ezinbestekoa da, kalitate oneko FM/NM kontaktua izateko. Nanofabrikazio teknika optimizatzearen ondorioz, gailu hauetan burutu ditugun neurketak oso errepikakorrak izatea lortu dugu (ikusi 4. Kapitulua), literaturan aurkitu daitezkeen spin polarizazio ($\alpha_{Co} = 0.12$ eta $\alpha_{Py} = 0.40$) eta spin difusio luzera altuenak ($\lambda_{Cu} = 1000$ nm) lortu ditugularik. Honek, ondoren aurkeztuko ditugun emaitzen fidagarritasuna bermatzen du.

Gure azterketan, lehenik eta behin, Co/Cu eta Py/Cu gainazal ohmikoak erabiliz, Py eta Co-aren spin polarizazioak lortu ditugu tenperaturaren menpe (ikusi 5. Kapitulua eta 5.2 irudia). Py-aren polarizazioa handiagoa da eta tenperaturaren menpe aldaketa nabarmena aurkezten du. Aldaketa honen menpekotasuna ulertzeko, Mott-en bi kanalen ereduan oinarritu gara, zeinaren arabera material FM batean gertatzen den karga garraioa bi kanal independentetan zehar gertatzen den, goranzko spin-ena ($\rho_{\uparrow}$ erresistibitateduna) eta beheranzko spin-ena ($\rho_{\uparrow}$ erresistibitateduna). Gainera, elektroi-magnoi sakabanaketa dela eta, tenperatura zero ez denean, bi kanalen artean momentu transferentzia bat dago, FM-aren spin polarizazioa txikituko duena. Momentu transferetzia horren neurria spin-nahaste erresistibitateak emango digu: $\rho_{\uparrow\downarrow}$.

Py-aren spin polarizazioa zein eroankortasun elektrikoa magnitude hauen menpe adieraz daitezke (5.2 eta 5.3 ekuazioak):

$$\alpha_F = \frac{\rho_\downarrow - \rho_\uparrow}{\rho_\uparrow + \rho_\downarrow + 4\rho_{\uparrow\downarrow}} \;;\; \sigma_F = \frac{\rho_\uparrow + \rho_\downarrow + 4\rho_{\uparrow\downarrow}}{\rho_\uparrow\rho_\downarrow + \rho_{\uparrow\downarrow}(\rho_\uparrow + \rho_\downarrow)} \;.$$

5.2 atalean adierazten den bezala, esperimentalki lorturiko α_F eta σ_F ekuazio hauekin aldi berean doituz, $\rho_\uparrow$, $\rho_\downarrow$ eta $\rho_{\uparrow\downarrow}$-ren tenperaturarekiko menpekotasunak lor daitezke. Gure emaitzen arabera, bi doiketak bateragarriak dira soilik α_F-ren balioak ~ 2 faktore batez biderkatuz zuzentzen direnean. Horrela erakutsi dugu LSV-ak darabiltzaten esperimentuetatik lortzen dugun α_F Mott-en ereduarekin azal daitekeela baina gutxietxita dagoela, ziurrenik, dimentsio bakarreko ereduaren hurbilketak direla eta.

Sistema hauetan α_{Py} eta α_{Co} lortzeaz gain, λ_{Cu} ere tenperaturaren menpe lortu dugu. 6.5 irudian ikusten den bezala, erabiltako material FM-ak ez die Cu-aren spin garraio propietateei eragiten. Bestalde, tenperatura baxuetan λ_{Cu}-k maximo harrigarri bat aurkezten du. Izan ere, λ_{Cu} erresistibitatearekiko (ρ_{Cu}) alderantziz proportzionala da, eta azken honek ez du minimorik tenperatura baxuetan.

Elliott eta Yafet-en teoriaren arabera, ezpurutasun magnetikorik ez duten metaletan, spin erlaxazioa spin-orbita elkarrekintzak eragindakoa da, spin erlaxazio denbora momentu erlaxazio denborarekiko proportzionala delarik: $1/\tau_{sf} = a/\tau_e$ (eta horregatik $\lambda_N \propto 1/\rho_N$). Aipatzekoa da $\lambda_N = \sqrt{D\tau_{sf}}$ dela, non D difusio konstantea den. Momentu erlaxazioa, aldi berean, ekarpen desberdinek osatzen dute, fonoiengandik (ph) eta defektuengandik (def) datozenak. Horrela, spin erlaxazio denborak bi gai izango ditu (6.5 ekuazioa):

$$\frac{1}{\tau_{sf}} = \frac{a_{ph}}{\tau_e^{ph}} + \frac{a_{def}}{\tau_e^{def}} \;,$$

a_{ph} eta a_{def} fonoiengandik eta defektuengandik datozen spin iraultze probabilitateak izanik.

Momentu zein spin erlaxazioan eragin handiena duten ekarpenak aztertzeko, dimentsio ezberdineko Cu kanalak dituzten Py/Cu LSV-ak neurtu ditugu, ρ_{Cu} (6.2 figura) eta λ_{Cu} (6.3 figura) tenperaturaren menpe lortzeko. Modu honetan, erresistibitatearen ekarpen nagusia ale mugak direla ondorioztatu dugu (6.1.1 atala). Spin erlaxazioari dagokionez, fonoiek eta defektuek eragindako spin iraultze mekanismoak (a_{ph} eta a_{def}-en balioek emanak) tenperatura eta kanal NM-aren dimentsioenkiko independenteak direla ondorioztatu dugu (ikusi 6.1 taula). Aldi berean, tenperaturarekiko menpekotasuna fonoiengandik datorren momentu erlaxazioak (τ_e^{ph}) ematen digula egiaztatu dugu.

Orain ere, dimentsio guztietako kanal NM-dun LSV-etan aurkitu dugu tenperatura baxuko λ_{Cu}-ren maximoa, Elliott-Yafet-en teoriak azaldu ezin duena. Ezpurutasun magnetikoei egozten diegu maximoa, berauen jatorria lurruntzen dugun Cu-an dagoelarik (6.3 atala).

Spin manipulazioari dagokionez, Hanle efektua sakonki aztertu dugu (ikusi 7. Kapitulua). Lehenago aipatu dugun bezala, honen abantaila nagusia LSV bakar batetik α_F eta λ_N-ren balioak eskura ditzakegula da. Halere, eztabaida sakona dago metodo honen baliagarritasunaren inguruan, batez ere kontaktu ohmikodun (hau da, FM/NM gainazal ohmikodun) LSV-ei dagokienez. Horregatik, metodo honetatik lorturiko emaitzak eta metodo tradizionaletik (L-ren menpe neurturiko ΔR_{NL}-ren doiketatik) lorturikoak alderatu ditugu kontaktu ohmikodun Py/Cu

LSV-etan eta kontaktu erresistentzia finitu bat zuten Co/Cu LSV-etan. Kontaktuak ohmikoak ez diren kasuan bi metodoek bat egiten duten arren, bien arteko desadostasun handia dago kontaktu ohmikoen kasuan, gaur egungo teoriak azaldu ezin duen interferentzia efektu gehigarri bat identifikatu dugularik.

Azkenik, spin manipulaziorako metodo berri bat proposatzen dugu (8. Kapitulua), spin-en eta material FM isolatzaile (FMI) baten arteko elkarrekintzan oinarritzen dena, horretarako, LSV-ak FMI-en gainean fabrikatuz. Ideia nagusia 8.1 irudian adierazirik dago: NM/FMI gainazalaren spin-nahaste konduktantzia (G_r) dela eta, spin korronte puruaren polarizazioa ($\vec{s}$) eta FMI-aren magnetizazioa ($\vec{M}$) perpendikularrak direnean, FMI-ak spin-ei eragindako torkearen ondorioz berauek xurgatuko ditu, detektorera iristen den korrontea (eta, beraz, neurturiko erresistentzia ez lokala) txikituz. $\vec{s}$ eta $\vec{M}$ paraleloak direnean, ordea, detektoreak neurtuko duen erresistentzia ez lokala, FMI-rik gabeko kasuan neurtuko lukeen bera da. Metodo honek, spin-ak manipulatzeko tresna egokia izateaz gain, NM/FMI gainazalak aztertzeko balio digu, euren G_r balioa lortzea ahalbidetzen duelarik.

Horretarako $Y_3Fe_5O_{12}$ (YIG) FMI-a erabili dugu, ferromagnetikoki biguna izanik, eremu magnetiko txikiak (250 Oe) nahikoa direlako bere magnetizazioa kontrolatzeko (8.3(a) irudia). Bestalde, Co/Cu LSV-ak erabili ditugu (8.3(b) irudia), Co-a ferromagnetikoki gogorra delako. LSV-en ezaugarria den $R_{NL}(H)$ kurban ikusten den moduan (8.3(c) irudia), 400 Oe baino handiagoa den eremu magnetiko bat behar da euren magnetizazioa aldatzeko. Spin korrontea manipulatzeko, eremu magnetikoaren norabidea aldatu dugu, elektrodo FM-ekiko α angelua osatuz (8.3(b) irudian adierazita dagoena). $R_{NL}(\alpha)$ neurtuz, erresistentzia ez-lokalean %8-ko bariazio bat neurtu dugu $\vec{s} \parallel \vec{M}$ eta $\vec{s} \perp \vec{M}$ kasuen artean (8.3(d) eta 8.4 irudiak). Sistema konkretu honetarako, dimentsio bakarreko spin difusio ekuazioa ebatziz, erresistentzia ez lokalarentzako honako espresioa lortu dugu (8.14 ekuazioa):

$$R_{NL} = \frac{P_I^2 R_N}{2}\left[\cos^2\alpha e^{-L/\lambda_N} + \sin^2\alpha \mathrm{Re}\left(\frac{\lambda_1}{\lambda_N}e^{-L/\lambda_1}\right)\right] \ ,$$

λ_1 honela definitu dugularik:

$$\lambda_1 = \frac{\lambda_N}{\sqrt{1 + \frac{t_N\lambda_N^2}{2\rho_N G_r} + i\frac{2\mu_B B\lambda_N^2}{D\hbar}}} \ .$$

Erro karratuaren barruko lehenengo gaia NM/FMI gainazalaren spin-nahasteari dagokio eta bigarrena, aldiz, Hanle efektuaren ondorioz gerta daitekeen spin korrontearen modulazioari. Azken hau, G_r-ri dagokiona baino magnitude orden bat txikiagoa izanik, ikusten dugun %8-ko modulazioa spin korrontea eta YIG-aren arteko elkarrekintzak azal dezake soilik. $R_{NL}(\alpha)$ kurba 8.14 ekuazioarekin doituz, $G_r \sim 4 \times 10^{11}\ \Omega^{-1}\mathrm{m}^{-2}$ balioa lortzen dugu.

Gure ustetan, tesi honetan aurkezturiko emaitzek interes handia daukate spintronika eta magnetismo arloetan dabiltzan zientzilarientzat eta ziur gaude esperimentu eta garapen berriak bideratuko dituela, spin korronte puruak zirkuitu logikoen mundura hurbilduz.

Abstract

Spintronics is a rapidly growing field that aims at using and manipulating not only the charge, but also the spin of the electron, as an alternative to conventional electronics. The objective of this field is to provide an answer to the constant miniaturization of silicon-based transistors, which cannot continue indefinitely due to increasing power dissipation and the emergence of quantum fluctuations when fewer atoms are involved. After the success of spintronics applications such as the hard-disk read head or the magnetic random access memory, based on the giant magnetoresistance effect in magnetic multilayers, the goal is to develop a second generation of spintronic devices, in which pure spin currents can be created and manipulated. These devices would provide a faster data processing, due to the added degree of freedom of the spin, together with a lower power consumption and heat dissipation related to the absence of charge transport. In such second generation of spintronic devices, achieving spin transport over long distances is crucial, for which materials with a long spin-diffusion length are needed.

In this thesis, we study the three key parameters for an optimum performance of these spintronic devices: spin injection, transport and manipulation. With this purpose, we use metallic lateral spin valves (LSVs), nanoscaled devices consisting of two ferromagnetic (FM) electrodes bridged by a non-magnetic (NM) channel, which, by using a non-local geometry, allow the electrical creation of pure spin currents as well as their transport over a long distance, easily enabling their manipulation.

After proving the reproducible performance of our devices due to a nanofabrication based on two consecutive electron-beam lithography processes, where the FM/NM interface quality is carefully optimized, the spin-injection properties of Co and Py are studied and compared by obtaining the spin polarization of both materials as a function of temperature in Co/Cu and Py/Cu LSVs with transparent interfaces. The spin polarization of Py is higher than that of the Co, and it presents a clear variation with temperature, which is in good agreement with the two-channel model if the detected correction factor of ~ 2 is applied.

The spin transport properties of Cu are also studied as a function of temperature. On the one hand, by using Co and Py electrodes, we show that the used FM metal does not affect the spin transport properties of Cu. On the other hand, the resistivity and the spin-diffusion length of Cu are obtained as a function of temperature and the dimensions of the Cu channel, identifying different sources of spin scattering. Whereas the spin-flip mechanisms coming from phonons and defects (which are dominated by the grain boundaries rather than the surface) are both independent of the temperature and the dimensions of the Cu channel, the temperature dependence of the spin relaxation in Cu arises from the contribution of the phonons to the momentum relaxation.

The most widely employed spin manipulation technique in LSVs is the Hanle effect, which is based on the precession of spins under an out-of-plane magnetic field. In this thesis, we use the Hanle effect as a tool for spin manipulation and also for obtaining information regarding the spin-injection and spin-transport properties of the LSVs. Devices with transparent interfaces and with a non-zero interface resistance are compared. Whereas the spin currents are effectively modulated in LSVs with a non-zero interface resistance and a reliable information is obtained, in the case of LSVs with transparent interfaces interference effects are observed, which cannot be explained with the current theory.

Finally, a novel method for spin manipulation is proposed by magnetically gating pure spin currents. This is possible with the fabrication of LSVs on top of a ferromagnetic insulator (FMI) and taking advantage of the concept of the NM/FMI spin-mixing interface conductance. A theory is proposed in order to explain a modulation of the pure spin currents, which is experimentally proven in Co/Cu LSVs fabricated on top of YIG. The value of the spin-mixing conductance of the Cu/YIG interface is obtained for the first time and clues for improving such value, as well as the spin current modulation itself, are presented.

Contents

Chapter 1

Introduction to Spintronics

Digital revolution has changed society in a way that was unimaginable when the electronic transistor was discovered in 1947. Electronic devices are continuously improving in performance and size, following Moore's law. However, the miniaturization of silicon-based (CMOS) transistors cannot continue indefinitely due to increasing power dissipation and the emergence of quantum fluctuations when fewer atoms are involved, and a new paradigm is needed. One of the alternatives to conventional electronics is spintronics, a rapidly growing field that aims at using and manipulating not only the charge, but also the spin of electron [1]. For instance, sophisticated applications such as the hard-disk read head or the magnetic random access memory have been introduced in the last two decades using spin-polarized currents. After this early success, a second generation of devices is now envisioned in which pure spin currents, a diffusive flow of spins with no net charge flow [1], could be used instead. Pure spin currents would carry more information (spin up or down) than charge currents and without the critical drawback of heat dissipation at a reduced scale. These spin-only circuits [2], which would lead to low-power circuit architectures and a data processing speed unachievable by ordinary charge-based information processing, could represent a post-CMOS paradigm in electronics industry, with its enormous social and economic impact.

1.1 Spin and ferromagnetism

If spintronics lies on spin currents, in order to understand its basis we first need to define what spin is. Spin is a quantum property of elementary particles, with no classical analogue, which can be visualized as an intrinsic and quantized angular momentum, $\vec{S}$. Since the electron is a charged particle, it has a magnetic moment associated to the spin angular momentum, in the form $\vec{\mu_s} = -\frac{g_s \mu_B}{\hbar}\vec{S}$, where $\hbar$ is Planck's constant divided by 2π, $g_s \simeq 2$ is the spin g factor and $\mu_B = \frac{e\hbar}{2m}$ is the Bohr magneton, a natural unit for expressing an electron magnetic moment; e and m are the elementary charge and the rest mass of the electron, respectively. There is a preferential direction in which the component of the spin is quantized as $S_z = m_s\hbar$, where m_s is the quantum number related to S_z, and can only have the values $m_s = \frac{1}{2}$ or $m_s = -\frac{1}{2}$. These are the so-called "spin-up" or "spin-down" states [3]. The magnetic moment associated to the spin of electron is, in general, much larger than the one associated to the nucleus of an atom and, therefore, it is the responsible of the magnetization of ferromagnetic (FM) materials, which is originated from an excess of spin-up (or spin-down) electrons.

The magnetization of the FM materials is originated from the exchange interaction. This is a quantum-mechanical effect based on Pauli's exclusion principle, which states that the wave function of a many-electron system has to be antisymmetric. Such antisymmetry might be originated either from the spatial part or from the spin part of the wave function. In ferromagnets, it is energetically more favorable to minimize the overlap of the spatial component of the wave function in order to minimize their repulsive Coulomb interaction, which is obtained by a parallel alignment of the spins [4].

What tells us whether a metal will present ferromagnetic order or not is the Stoner criterion. In metals, only the inner shell electrons account for the exchange interaction, these are the *3d* electrons in elemental ferromagnetic elements (Ni, Co and Fe). The Stoner model of ferromagnetism [5] assumes that, in these metals, the *3d* spin sub-bands are shifted with respect to each other (see Fig. 2.1(a)), which happens because the relative gain in exchange energy is larger than the increase of kinetic energy due to the band shifting. This results in the previously mentioned excess of spin-up (or spin-down) electrons, where more electrons posses a favored spin orientation (we will call the electrons with the favored spin orientation the majority electrons). The sum of all the magnetic moments associated to each electron gives a finite macroscopic magnetization of the FM material at thermodynamic equilibrium.

The two-channel model

As a result of the energy shift of the spin sub-bands, the electronic density of states (DOS) at the Fermi energy (E_F) becomes different for different spin sub-bands (see Fig. 2.1(a)). Due to the difference in DOS, and considering that the spin-flip scattering is negligible (*i.e*, the distance over which the spin is lost is much longer than the electronic mean free path), there is a difference in Fermi velocities and mean free paths, and therefore in conductivities, for spin-up and spin-down electrons:

$$\sigma_\uparrow = \frac{1}{3} N_\uparrow(E_F) e^2 \uparrow v_\uparrow l_{e\uparrow} \ , \tag{1.1}$$

$$\sigma_\downarrow = \frac{1}{3} N_\downarrow(E_F) e^2 \downarrow v_\downarrow l_{e\downarrow} \ , \tag{1.2}$$

where $N_{\uparrow,\downarrow}(E_F)$ are the spin-dependent DOS at E_F, and $v_{\uparrow,\downarrow}$ and $l_{e\uparrow,\downarrow}$ are the average spin-dependent Fermi velocities and electron mean free paths. Hence, the conduction in a FM metal can be visualized as spin-up and spin-down electrons being independently carried by two parallel channels, as introduced by Mott in 1936 [6, 7]. This leads to a net spin polarization α_F, which makes FM materials an excellent source of spin-polarized currents:

$$\alpha_F = \frac{\sigma_\uparrow - \sigma_\downarrow}{\sigma_\uparrow + \sigma_\downarrow} \ . \tag{1.3}$$

Please note that the majority electrons are not necessarily the ones with a higher electrical conductivity, since the dependence of the electrical conductivity with the DOS is not trivial and depends on each metal [7].

In addition, it is remarkable that, even if the electrical current is mainly carried by s-electrons, the band splitting occuring in the *3d* sub-bands is the responsible for the two independent conduction channels for spin-up and spin-down electrons. What happens is that, in *3d*-metals including FM metals such as Ni, Co or Fe, a hybridization between s and d bands occurs and the s-electrons are scattered into the density of states of the d bands. One of the s sub-bands, thus, suffers more scattering, leading to a conductivity imbalance and, as a consequence, to a net spin polarization of the current [7].

1.2 Historical perspective and state-of-the-art

1.2.1 GMR and TMR

It is generally recognized that spintronics as scientific and technological field properly started in the late 1980s with the discovery of giant magnetoresistance (GMR) in metallic multilayers by Albert Fert and Peter Grünberg [8, 9]. GMR is defined as a dramatic change in electrical resistance under an applied magnetic field in magnetic multilayers.

The most basic structures where GMR can be observed are the spin valves. These are trilayered structures composed by a non-magnetic (NM) conductor sandwiched between two FM metals. When an electrical current is driven through the spin valve, its electrical resistance will change depending on the relative magnetization of the FM layers. This can be easily understood if one thinks of the previously explained Mott's two-channel model.

Figure 1.1 shows a spin valve for the cases where the relative magnetization of the FM electrodes is parallel (Fig. 1.1(a)) and antiparallel (Fig. 1.1(b)). Let us consider that the low resistance channel in FM metals is the one of the majority electrons. These are the spin-up electrons in the first FM. When an electrical current is applied through the spin valve, a spin-polarized current will be driven from the first FM metal into the NM (*i.e.*, mostly spin-up electrons will cross into the NM). When the spin-polarized current enters the second FM, two things can occur: (*i*) the majority electrons of the second FM are also spin up (parallel magnetizations); therefore, spin-up electrons encounter a low resistance in the second FM and the overall resistance state of the spin valve will be low (see equivalent circuit sketched in Fig. 1.1(c)). (*ii*) the majority electrons of the second FM are spin down (antiparallel magnetizations); therefore, spin-up electrons will encounter a high resistance, leading to an overall high resistance of the spin valve (see equivalent circuit sketched in Fig. 1.1(d)).

The interest from the magnetic recording industry was of paramount importance for the spintronics take off and commercial applications of GMR arose in the 1990's with the introduction of hard-disk read heads based on this technology. Fert and Grünberg were awarded with the Nobel Prize in Physics in 2007 for such discovery.

When the NM conductor is replaced by an insulator, the resulting trilayered structure is called magnetic tunnel junction (MTJ) [10–13]. The effect arising in such devices is called tunneling magnetoresistance (TMR) and it works in a similar manner to GMR. It is based on the fact that the spin is conserved during tunneling and that the tunnelling current is, in general, proportional to

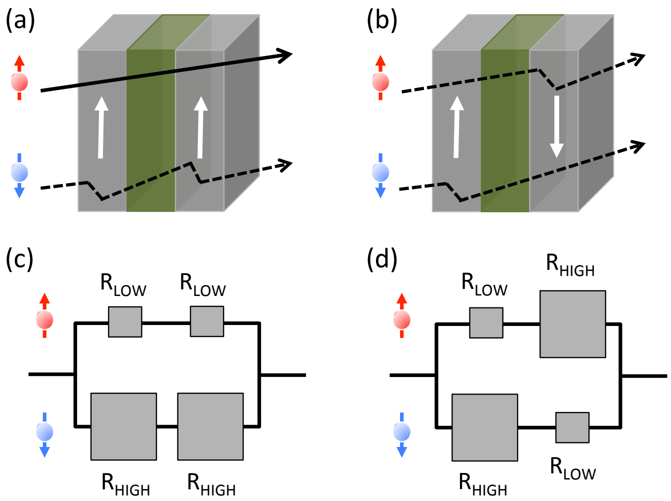

Figure 1.1: Schematic representation of the transport of spin-polarized current in a spin valve with (a) parallel and (b) antiparallel ferromagnetic layers. (c)-(d) Equivalent circuit taking into account the two-channel model. In (c) the overall resistance of the device is low, whereas in (d) is high.

the interfacial density of states at the Fermi level of the two FM metals [14]. MTJs represented a step forward in the field of spintronics, due to the sophisticated applications it brought, such as the magnetic random access memory (MRAM) [15], or due to the discovery of spin filtering when using magnesium oxide (MgO) as an insulating layer, which allowed to measure magnetoresistances of the order of 200% at room temperature in 2004 [11, 12]. More recently, TMR effects up to 600% were obtained at room temperature [13].

1.2.2 Generation of pure spin currents

The previously mentioned devices exploit spin-polarized currents, transported at small distances (around 1-10 nm) where no direct spin manipulation is involved. However, as mentioned in the beginning of this Chapter, a second generation of spintronic devices is now envisioned in which pure spin currents are used instead. This type of devices should be suitable for spin transport over a significantly longer distance (>100 nm), which would enable the manipulation of the transported spin information.

Figure 1.2 shows the key ingredients for the performance of a second generation of spintronic devices: (*i*) Injection and detection of pure spin currents; (*ii*) spin transport over long distances (>100 nm); (*iii*) manipulation of the transported spin information.

Although there are several approaches to generate pure spin currents into a NM material such as optical pumping [16], spin pumping *via* ferromagnetic resonance [17, 18] or thermal spin injection [19, 20], this thesis is focused on electrical spin injection, since it is the most convenient method for integration with electronics. Electrical spin injection was first obtained in metals using lateral spin

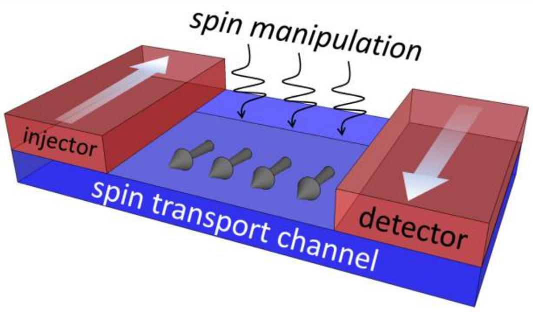

Figure 1.2: Sketch of a second generation spintronic device. Key ingredients for the performance of the device are shown: (*i*) Injection and detection of pure spin currents from a FM; (*ii*) spin transport over long distances; (*iii*) manipulation of the transported spin information.

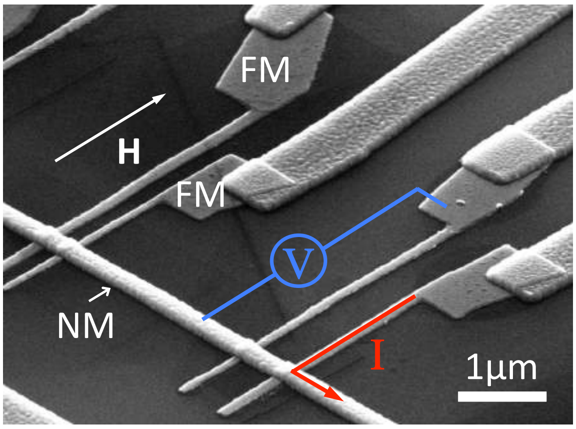

Figure 1.3: Scanning electron microscopy (SEM) image of one of our devices where two lateral spin valves are seen. NM and FM materials, measurement configuration and direction of the applied magnetic field are tagged.

valves (LSV). These devices consist of two FM electrodes bridged by a NM channel (see Fig. 1.3). They work in a similar way to conventional spin valves but, due to their geometry, non-local measurements can be performed: a current is injected from one of the FM electrodes (the injector) to the NM, and the voltage between the other FM electrode (the detector) and the NM is measured. This way, the spin is decoupled from the charge, enabling the creation of a pure spin current. Further details on how LSVs work are given in Chapter 2.

The first spin injection experiment using LSVs was done in 1985 by Johnson and Silsbee [21]. They injected a pure spin current into a 50-μm-thick, 100-μm-wide and 1.5-cm-long aluminum single crystal, using 15-μm-wide permalloy electrodes. It was not until 2001 that the pioneering work by Johnson and Silsbee was continued, when Jedema and coworkers performed spin injection experiments in metallic nanometric LSVs [22, 23], similar to the ones used nowadays (see Fig. 1.3). After this work, spin injection into metals has been studied in detail [22–35] and LSVs have been used for injecting pure spin current into several materials, such as semiconductors [36, 37], superconductors [38, 39] and carbon-based materials such as carbon nanotubes [40] or graphene [41, 42].

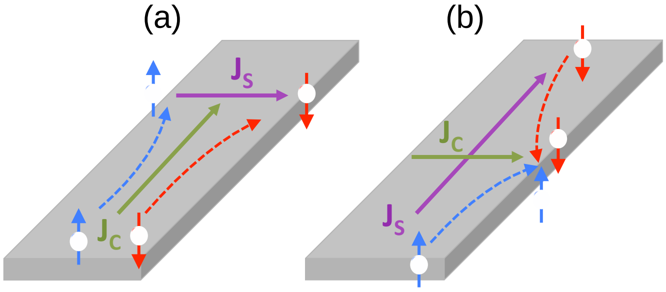

Figure 1.4: (a) Schematic representation of the spin Hall effect, where a charge current ($\vec{J}_C$) creates a transverse spin current ($\vec{J}_S$) due to SOC in a NM metal. (b) Schematic representation of the inverse spin Hall effect, where a spin current ($\vec{J}_S$) creates a transverse charge current ($\vec{J}_C$) due to SOC in a NM metal.

Finally, it is worth mentioning the spin Hall effect (SHE), which allows the creation of pure spin currents electrically by using NM materials with large spin-orbit coupling (SOC) and avoiding the use of FM metals and magnetic fields [43–47]. The SHE is the equivalent in a NM conductor of the anomalous Hall effect, well known in FM metals [48,49]. When an unpolarized charge current ($\vec{J}_C$) flows in a NM conductor, the spin-up and spin-down electrons tend to be deflected in opposite directions due to SOC. This deflection causes a spin accumulation at the edges of the metal, resulting in a pure spin current ($\vec{J}_S$) in the transverse direction to the charge current (see Fig. 1.4(a)). Among the technological advantages that this effect can provide, there are applications such as the magnetization switching of FM elements, which has been recently achieved with spin-transfer torques arising from the SHE [50].

There is also the reciprocal effect, known as inverse SHE (ISHE), in which a transverse charge current is created from the flow of a pure spin current (Fig. 1.4(b)). ISHE is useful in spin-detection experiments, such as the detection of a spin current that has been created by spin pumping [17] or spin Seebeck effect [20].

SHE and ISHE have an additional interest because they are at the basis of the recently discovered spin Hall magnetoresistance (SMR), which will be discussed in detail in section 2.2.2.

1.2.3 Spin transport and relaxation

Not every material is suitable for a long distance spin transport. The way to quantify how effective the spin transport is in a certain material is by means of its spin-relaxation time, τ_{sf}, or its spin-diffusion length, λ. These quantities account for the time scale or the distance, respectively, over which a spin current can propagate without losing its polarization and are related to each other by $\lambda = \sqrt{D\tau_{sf}}$, where D is the diffusion constant.

In metals, in the absence of magnetic impurities, the main spin-relaxation mechanism is the Elliott-Yafet mechanism [51,52]. According to this mechanism, during the momentum scattering of an electron, its spin interacts with the local electric field created by the lattice ions through the SOC, eventually flipping the spin. The spin-relaxation time is, thus, proportional to the momentum-relaxation time, $1/\tau_{sf} = a/\tau_e$, where the proportionality constant a directly depends on the SOC constant of the material, as is briefly discussed in section 2.1.1. For this reason, metals with a low atomic number (Z), high purity and high crystallinity are suitable for spin transport. The best ones reported in literature are Cu [22–25], Al [31, 32] and Ag [33–35], with values of λ reaching 1-2 μm and spin currents that can be detected beyond 6 μm.

For the case of semiconductors, the longest spin-diffusion length (38 μm) has been observed in undoped Si [53], but this value quickly decreases when doped (2.35 μm for a concentration of $5 \cdot 10^{19}$ cm^{-3} [54]). A heavier element such as Ge has lower λ (0.58 μm for a concentration of $1 \cdot 10^{16}$ cm^{-3} [55]), as expected from the Elliott-Yafet mechanism.

However, in semiconductor crystals without inversion symmetry, the spin-bands are no longer degenerate (in the same momentum state, spin-up and spin-down states have different energy). The electrons feel a momentum-dependent effective magnetic field which makes spins precess around it. Therefore, contrary to the Elliott-Yafet mechanism, momentum scattering acts against spin relaxation as $\tau_{sf} \propto 1/\tau_e$, which is known as the D'yakonov-Perel' mechanism [56]. This is the case of GaAs, with $\lambda \sim$6 μm for an n-doped sample [36].

In semiconductors, there is another spin-relaxation mechanism one needs to consider: the Bir-Aronov-Pikus mechanism [57], which originates from the conduction electron-hole exchange interaction. It only plays an important role, thus, in systems with a large number of holes, *i.e.*, p-type semiconductors. Fluctuations in the effective hole concentration produce a fluctuating effective magnetic field generated by the total spin of the holes, which induces a precession of the electron spin around its axis, similar to the D'yakonov-Perel' mechanism. Theoretical studies of spin relaxation in intrinsic and p-type GaAs quantum wells [58] predict that the Bir-Aronov-Pikus mechanism is much smaller than the D'yakonov-Perel' one, and that they only become comparable at high temperature when the hole density and the width of the quantum well are large enough. Hence, unlike in the bulk samples, the Bir-Aronov-Pikus mechanism hardly dominates the spin relaxation in nanoscale samples.

Finally, it is worth giving some insight about graphene, the spin transport material that has drawn more attention in the last years. Due to its small intrinsic SOC and the lack of hyperfine interaction, long spin-diffusion lengths are expected [59]. The first experimental demonstration of spin transport in exfoliated monolayer graphene yielded $\lambda \sim 2$ μm at room temperature [41], which is of the same order as the λ values obtained in metals. Subsequent experiments in suspended graphene ($\lambda \sim 1.9$ μm [42]) or on top of hexagonal boron nitride ($\lambda \sim 4.5$ μm [60]) to avoid the effect of substrate and graphene roughness gave only marginal improvement in λ but similar τ_{sf}. Bilayer graphene presents slightly better numbers ($\lambda \sim 5.4$ μm [61]). Whereas both Elliott-Yafet and D'yakonov-Perel' mechanisms have been identified [60, 61], the origin of the unexpected spin relaxation is far from clear.

1.3 This thesis

The aim of this thesis is divided into three main parts, which are directly related to the study of the key ingredients for the performance of spintronic devices: (*i*) electrical spin injection in FM/NM systems (*ii*) spin transport in NM metals and (*iii*) spin manipulation methods. LSVs are employed in order to obtain pure spin currents, providing the proper scenario for our investigation by eliminating any spurious effect coming from the charge currents.

The manuscript is divided into nine chapters. Chapter 1 is an introduction to the topic: the history and the last advances in spintronics are collected, and LSVs are presented for the first time.

Chapter 2 presents the existing theory of spin injection, transport and manipulation in LSVs, which will be the basis for our experiments and further theoretical development.

Details on the fabrication and the measurements of the LSVs are described in Chapter 3. Due to an optimized nanofabrication procedure highly reproducible LSVs are obtained, as shown in Chapter 4.

The obtained reproducibility allows us to study the spin polarization as a function of temperature in different FM materials (cobalt and permalloy) in Chapter 5. In addition, in Chapter 6, several effects (dimensions of the NM channel, temperature, use of different FM electrodes or magnetic impurities) are considered in order to study their contribution to the spin relaxation in the NM metal (copper).

Whereas the above mentioned first two parts (spin injection and transport) for the realization of spin-only circuits are reasonably well established, the third one (spin manipulation) has not achieved such a maturity. With this purpose, in the third part of the thesis the attention is focused onto different ways of spin manipulation. In Chapter 7, the spins are manipulated by applying an out-of-plane magnetic field (the Hanle effect), which allows us to study the influence of different FM/NM interface resistances and the validity of this method for obtaining relevant information about the FM and NM materials (such as the spin polarization and the spin-diffusion length). In Chapter 8, a new method for spin manipulation is proposed and developed by fabricating LSVs on top of FM insulators, whose magnetization directly affects the spin transport. A theory is developed as a basis of the proposed spin manipulation, which is experimentally verified.

Finally, the conclusions of this work and future perspectives are given in Chapter 9.

References

[1] *Spin Current*, edited by S. Maekawa, S. O. Valenzuela, E. Saitoh and T. Kimura (Oxford University Press, Oxford, 2012).

[2] B. Behin-Aein, D. Datta, S. Salahuddin, and S. Datta, Nat. Natotech. **5**, 266 (2010).

[3] *Quantum Mechanics*, vols. 1 and 2, C. Cohen-Tannoudji, B. Diu, and F. Laloë (John Wiley & Sons, 2006).

[4] *Magnetism in Condensed Matter*, S. Blundell (Oxford Master Series in Condensed Matter Physics, 6th Edition, 2007).

[5] E. C. Stoner, Proc. Roy. Soc. London A **165**, 372 (1938).

[6] N. F. Mott, Proc. Roy. Soc. A **153**, 699 (1936).

[7] J. F. Gregg, I. Petej, E. Jouguelet, and C. Dennis, J. Phys. D: Appl. Phys. **35**, R121 (2002).

[8] M. N. Baibich, J. M. Broto, A. Fert, F. Nguyen van Dau, F. Petroff, P. Eitenne, G. Creuzet, A. Friederich, J. Chazelas, Phys. Rev. Lett. **61**, 2472 (1988).

[9] G. Binasch, P. Grünberg, F. Saurenbach, W. Zinn, Phys. Rev. B **39**, 4828 (1989).

[10] J. S. Moodera, L. S. Kinder, T. M. Wong, and R. Meservey, Phys. Rev. Lett. **74**, 3273 (1995).

[11] S. S. P. Parkin, C. Kaiser, A. Panchula, P. M. Rice, B. Hughes, M. Samant and S.-H. Yang, Nat. Mater. **3**, 862 (2004).

[12] S. Yuasa, T. Nagahama, A. Fukushima, Y. Suzuki, and K. Ando, Nat. Mater. **3**, 868 (2004).

[13] S. Ikeda, J. Hayakawa, Y. Ashizawa, Y.M. Lee, K. Miura, H. Hasegawa, M. Tsunoda, F. Matsukura, and H. Ohno, Appl. Phys. Lett. **93**, 082508 (2008).

[14] R. Mersevey and P. M. Tedrow, Phys. Rep. **238**, 173 (1994).

[15] J. Akerman, Science **308**, 508 (2005).

[16] J. M. Kikkawa and D. D. Awschalom, Nature **397**, 139 (1999).

[17] E. Saitoh, M. Ueda, H. Mikajima, and G. Tatara, Appl. Phys. Lett. **88**, 182509 (2006).

[18] Y. Kajiwara, H. Harii, S. Takahashi, J. Ohe, K. Uchida, M. Mizuguchi, H. Umezawa, H. Kawai, K. Ando, K. Takanashi, S. Maekawa, and E. Saitoh, Nature **464**, 262 (2010).

[19] A. Slachter, F. L. Bakker, J.-P. Adam, and B. J. van Wees, Nat. Phys. **6**, 879 (2010).

[20] K. Uchida, J. Xiao, H. Adachi, J. Ohe, S. Takahashi, J. Ieda, T. Ota, Y, Kajiwara, H. Umezawa, H. Kawai, G. E. W. Bauer, S. Maekawa, and E. Saitoh, Nature Mater. **9**, 894 (2012).

[21] M. Johnson and R. H. Silsbee, Phys. Rev. Lett. **55**, 1790 (1985).

[22] F. J. Jedema, A. T. Filip, and B. J. van Wees, Nature **410**, 345 (2001).

[23] F. J. Jedema, M. S. Nijboer, A. T. Filip, and B. J. van Wees, Phys. Rev. B **67**, 085319 (2003).

[24] T. Kimura, Y. Otani, and J. Harmle, Phys. Rev. B **73**, 132405 (2006).

[25] T. Kimura, T. Sato, and Y. Otani, Phys. Rev. Lett. **100**, 066602 (2008).

[26] S. O. Valenzuela and M. Tinkham, Appl. Phys. Lett. **85**, 5914 (2004).

[27] Y. Ji, A. Hoffmann, J. S. Jiang, and S. D. Bader, Appl. Phys. Lett. **85**, 052509 (2004).

[28] S. Garzon, I. Žutić, and R. A. Webb, Phys. Rev. Lett. **94**, 176601 (2005).

[29] F. Casanova, A. Sharoni, M. Ehrekhinsky, and I. K. Schuller, Phys. Rev. B **79**, 184415 (2009).

[30] P. Łączkwoski, L. Vila, S. Ferry, A. Marty, J. M. George, H. Jaffrés, A. Fert, T. Kimura, T. Yang, Y. Otani, and J. P. Attané, Appl. Phys. Express **4**, 063007 (2011).

[31] N. Poli, M. Urech, V. Korenivski, and D. B. Haviland, J. Appl. Phys. **99**, 08H701 (2006).

[32] A. Vogel, J. Wulfhorst, and G. Meier, Appl. Phys. Lett. **94**, 122510 (2009).

[33] G. Mihajlovic, J. E. Pearson, S. D. Bader, and A. Hoffmann, Phys. Rev. Lett. **104**, 237202 (2010).

[34] Y. Fukuma, L. Wang, H. Idzuchi, S. Takahashi, S. Maekawa, and Y. Otani, Nat. Mater. **10**, 527 (2010).

[35] H. Idzuchi, Y. Fukuma, L. Wang, and Y. Otani, Appl. Phys. Lett. **101**, 022415 (2012).

[36] X. Lou, C. Adelmann, S. A. Crooker, E. S. Garlid, J. Zhang, K. S. M. Reddy, S. D. Flexner, C. J. Palmstrøm, and P. A. Crowell, Nat. Phys. **3**, 197 (2007).

[37] Y. Aoki, M. Kameno, Y. Ando, E. Shikoh, Y. Suzuki, T. Shinjo, M. Shiraishi, T. Sasaki, T. Oikawa, and T. Suzuki, Phys. Rev. B **86**, 081201(R) (2012).

[38] N. Poli, J. P. Morten, M. Urech, A. Brataas, D. B. Haviland, and V. Korenivski, Phys. Rev. Lett. **100**, 136601 (2008).

[39] K. Ohnishi, T. Kimura, and Y. Otani, Appl. Phys. Lett. **96**, 192509 (2010).

[40] L. E. Hueso, M. A. Pruneda, V. Ferrari, G. Burnell, J. Valdes, B. Simons, P. B. Littlewood, A. Fert, and N. D. Mathur, Nature **445**, 410 (2007).

[41] N. Tombros, C. Jozsa, M. Popinciuc, H. T. Konkman, and B. J. van Wees, Nature **448**, 571 (2007).

[42] I. Neumann, J. Van de Vondel, G. Bridoux, M. V. Costache, F. Alzina, C. V. Sotomayor Torres, and S. O. Valenzuela, SMALL **9**, 156 (2013).

[43] M. I. D'yakonov and V. I. Perel', Phys. Lett. A **35**, 459 (1971).

[44] J. E. Hirsch, Phys. Rev. Lett. **83**, 1834 (1999).

[45] S. O. Valenzuela and M. Tinkham, Nature **442**, 176 (2006).

[46] T. Kimura, Y. Otani, T. Sato, S. Takahashi, and S. Maekawa, Phys. Rev. Lett. **98**, 156601 (2007).

[47] A. Hoffmann, IEEE Trans. Magn. **49**, 5172 (2013).

[48] R. Karplus and J. M Luttinger, Phys. Rev. **95**, 1154 (1954).

[49] N. Nagaosa, J. Sinova, S. Onoda, A. H. MacDonald, and N. P. Ong, Rev. Mod. Phys. **82**, 1539 (2010).

[50] K. Garello, I. M. Miron, C. O. Avci, F. Freimuth, Y. Mokrousov, S. Blügel, S. Auffret, O. Boulle, G. Gaudin, and P. Gambardella, Nat. Nanotech. **8**, 587 (2013).

[51] R. J. Elliott, Phys. Rev., **96**, 266 (1954).

[52] Y. Yafet, in *Solid State Physics*, edited by F. Seitz and D. Turnbull (Academic, New York, 1963), pp. 1-98.

[53] I. Appelbaum, B. Huang, and D. J. Monsma, Nature **447**, 295 (2007).

[54] T. Sasaki, T. Oikawa, T. Suzuki, M. Shiraishi, Y. Suzuki, and K. Noguchi, Appl. Phys. Lett. **96**, 122101 (2010).

[55] Y. Zou, W. Hang, L.-T. Chang, F. Xiu, M. Wang, M. Oehme, I. A. Fischer, J. Schulze, R. K. Kawakami, and K. L. Wang, Phys. Rev. B **84**, 125323 (2011).

[56] M. I. D'yakonov and V. I. Perel', Sov. Phys. JETP **33**, 1053 (1971).

[57] G. L. Bir, A. G. Aronov and G.E. Pikus, Sov. Phys. JETP **42**, 705 (1976).

[58] J. Zou and M. W. Wu, Phys. Rev. B **77**, 075318 (2008).

[59] D. Huertas-Hernando, F. Guinea, and A. Brataas, Phys. Rev. Lett. **103**, 146801 (2009).

[60] P. J. Zomer, M. H. D. Guimarães, N. Tombros, and B. J. van Wees, Phys. Rev. B **86**, 161416(R) (2012).

[61] W. Han and R. K. Kawakami, Phys. Rev. Lett. **107**, 047207 (2011).

Chapter 2

Lateral Spin Valves

As mentioned in section 1.2.2, LSVs work in a similar way to conventional spin valves but, due to their non-local geometry (shown in Fig. 1.3), they allow the injection and transport of pure spin currents into a NM material. In 1993, Valet and Fert developed a one-dimensional theory in order to explain the GMR effect in magnetic multilayers [1]. In the early 2000's, together with the pioneering LSV experiments, Jedema and coworkers extended the Valet-Fert theory [2]. Based on that and the subsequent work that has ben done in this field, the principles of injection and transport of pure spin currents are explained in detail in this Chapter, pointing out the most relevant results for the development of this thesis.

2.1 Theory of spin injection and transport

In a LSV, the driving force of a pure spin current is the gradient of the spin-up and spin-down chemical potentials in the NM channel. The chemical potential, μ_{ch}, is by definition the energy needed to add one electron to the system, which at absolute zero is equal to the Fermi energy E_F. When there is an excess of electrons, near the equilibrium ($\mid eV \mid < k_B T$), the chemical potential is equal to the excess electron particle density n divided by the density of states (DOS) at the Fermi energy: $\mu_{ch} = n/N(E_F)$. If the electrons are subjected to an electric field $\vec{E}$, they have an additional potential energy, which should be added to μ_{ch} to get the electrochemical potential (ECP), $\mu = \mu_{ch} - eV$, where e is the electron charge and V is the electric potential. A gradient in the ECP will cause an electron transport in the form of a current density:

$$\vec{j_C} = \frac{\sigma}{e} \vec{\nabla} \mu \ , \tag{2.1}$$

where σ is the electrical conductivity. The electron transport can be due to both an electric field ($\vec{E} = -\vec{\nabla} V$) or to a spatial variation in the electronic density ($\vec{\nabla} \mu_{ch} \propto \vec{\nabla} n$).

When a spin-polarized current is driven from a FM metal (Fig. 2.1(a)) into a NM, it will encounter that both sub-bands and, thus, conductivities for spin-up and spin-down electrons are equal (Fig. 2.1(b)), originating a spin accumulation (*i.e*, a non-equilibrium population of the spin-up and spin-down electrons) at the NM, close to the FM/NM interface (Fig. 2.1(c)) [3].

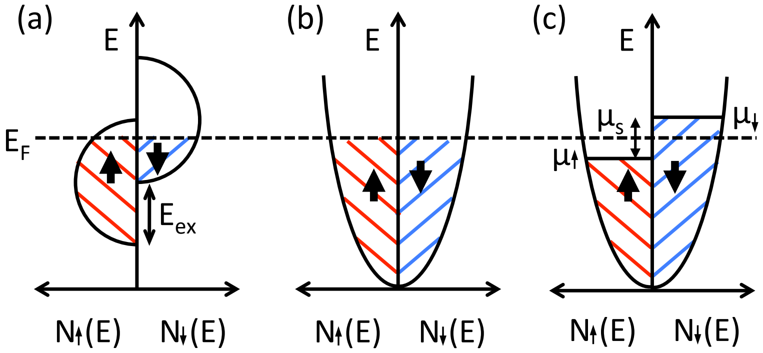

Figure 2.1: (a) Schematic representation of the DOS of *3d* spin sub-bands in a FM metal. The bands are shifted with respect to each other due to exchange interaction. (b) Schematic representation of the *s* spin sub-bands in a NM metal, where there is no spin accumulation. (c) Schematic representation of the *s* spin sub-bands in a NM metal, near the FM/NM interface, where there is spin accumulation.

The spin accumulation is defined as the difference between spin-up and spin-down ECPs, $\mu_s = \mu_\uparrow - \mu_\downarrow$. Therefore, the gradient of spin-up and spin-down potentials is the responsible for the spin transport:

$$\vec{j}_{\uparrow,\downarrow} = \frac{\sigma}{e}\vec{\nabla}\mu_{\uparrow,\downarrow} \ , \tag{2.2}$$

where $\vec{j}_{\uparrow,\downarrow}$ are the spin-up and spin-down current densities. The sum of both results in the total charge current density

$$\vec{j}_C = \vec{j}_\uparrow + \vec{j}_\downarrow \ . \tag{2.3}$$

In addition, a spin current density can be defined as

$$\vec{j}_S = \vec{j}_\uparrow - \vec{j}_\downarrow \ . \tag{2.4}$$

If a charge current (I) is injected in a geometry such as the one shown in Fig. 2.2(a), the generated spin accumulation will diffuse to both sides of the NM channel. Therefore, even where there is no net charge flowing, $\vec{j}_C = 0$, (right side of the NM channel in Fig. 2.2(a)), there will be a net flow of spins, $\vec{j}_S \neq 0$, decoupling a pure spin current from the charge current.

Figure 2.2(b) shows a scheme of the ECP in a LSV. An electric bias is being applied through the FM injector in order to drive a spin-polarized current, which generates the slope in the ECP. At the FM/NM interface, the continuity of the spin-up and spin-down ECPs is the responsible for the spin accumulation, μ_s. The ECP itself is discontinuous at the FM/NM interface and zero throughout the middle part of the NM channel, as there is not net charge flowing here. μ_s tends to decay along the NM channel, which generates a pure spin current. From Fig. 2.2(b) and Eq. 2.4 one can visualize it as the sum of two opposite charge currents for opposite spins. If another FM electrode (the detector) is placed at a certain distance from the FM injector, a discontinuity in the ECP ($\Delta\mu$ from Fig.

2.2(b)) will build a voltage at the second FM/NM interface ($V_S = \Delta\mu/e$), which is proportional to the spin accumulation at that point [3].

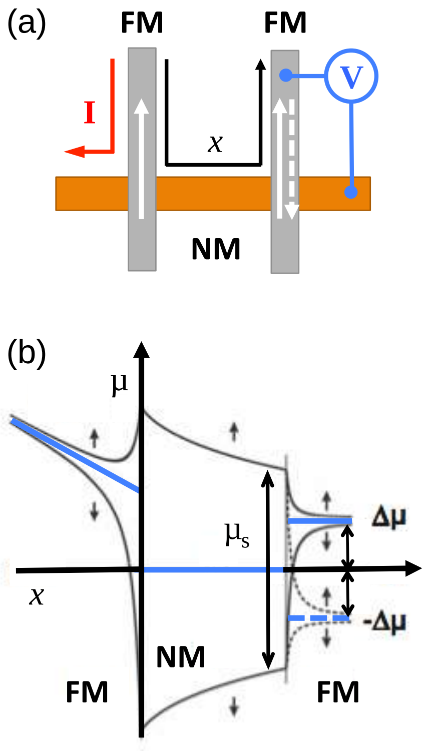

Figure 2.2: (a) Sketch of a LSV. Materials, magnetization of the FM electrodes and measurement configuration are shown. (b) Schematic representation of the electrochemical potential (blue line) across the x line sketched in the LSV. Black solid (dashed) line is a representation of the spin-up and spin-down chemical potentials in the case where both FM electrodes have a parallel (antiparallel) magnetization. Figure adapted from Ref. [8].

An expression for the voltage V_S measured by the FM detector can be obtained by solving the one-dimensional (1D) spin-dependent diffusion equation formulated by Valet and Fert [1]. The diffusive regime is considered because the dimensions of the LSVs (generally hundreds or thousands of nanometers) are, in general, larger than the electron mean free path, l_e (tenths of nanometers in the case of metals). The NM channel length is generally of the order of ~ 200-2000 nm, whereas the width and the thickness are around ~ 100 nm; the 1D spin-diffusion equation is, thus, a good approximation which has, in turn, a simple analytical solution.

The 1D spin-diffusion equation is the following:

$$D\frac{\partial^2 \mu_s}{\partial x^2} = \frac{\mu_s}{\tau_{sf}} , \tag{2.5}$$

where D is the diffusion constant and τ_{sf} is the spin-relaxation time. The solution of the previous equation has the general form:

$$\mu_s = \mu_+ e^{-x/\lambda_N} + \mu_- e^{x/\lambda_N} , \tag{2.6}$$

where we define the spin-diffusion length as $\lambda_N = \sqrt{D\tau_{sf}}$ and μ_+ and μ_- are constants to be determined by the boundary conditions (charge and spin current continuity) at both FM/NM interfaces. The voltage measured at the second FM/NM interface is given by [4]:

$$V_S = I \frac{2R_N \left[\frac{P_{I1}}{1-P_{I1}^2}\left(\frac{R_{I1}}{R_N}\right)+\frac{\alpha_{F1}}{1-\alpha_{F1}^2}\left(\frac{R_{F1}}{R_N}\right)\right]\left[\frac{P_{I2}}{1-P_{I2}^2}\left(\frac{R_{I2}}{R_N}\right)+\frac{\alpha_{F2}}{1-\alpha_{F2}^2}\left(\frac{R_{F2}}{R_N}\right)\right]e^{-L/\lambda_N}}{\left[1+\frac{2}{1-P_{I1}^2}\left(\frac{R_{I1}}{R_N}\right)+\frac{2}{1-\alpha_{F1}^2}\left(\frac{R_{F1}}{R_N}\right)\right]\left[1+\frac{2}{1-P_{I2}^2}\left(\frac{R_{I2}}{R_N}\right)+\frac{2}{1-\alpha_{F2}^2}\left(\frac{R_{F2}}{R_N}\right)\right]-e^{-2L/\lambda_N}} , \quad (2.7)$$

where α_{Fi} and λ_N are the previously defined spin polarizations of the FM injector ($i = 1$) and detector ($i = 2$) (Eq. 1.3) and the spin-diffusion length of the NM channel. R_{Ii} is the electrical resistance of each FM/NM interface and P_{Ii} is its corresponding spin polarization, which is defined as follows [2, 4, 12]:

$$P_{Ii} = \frac{R_{Ii}^{\downarrow} - R_{Ii}^{\uparrow}}{R_{Ii}^{\downarrow} + R_{Ii}^{\uparrow}} . \quad (2.8)$$

This is a phenomenological definition that accounts for the spin injection efficiency of the interface. L is the edge-to-edge distance between the FM injector and detector, $R_N = \lambda_N\rho_N/w_N t_N$ is the spin resistance of the NM channel and $R_{Fi} = \lambda_F\rho_F/w_N w_{Fi}$ are the spin resistances of the FM injector and detector. λ_F is the spin-diffusion length of the FM metal, $\rho_{N,F}$ are the electrical resistivities of the NM and FM materials, $w_{N,Fi}$ are the widths of the NM channel and the FM electrodes and t_N is the thickness of the NM channel.

The spin resistance of a material can be seen as the tendency that this material has to absorb spins, *i.e.*, spins will prefer to diffuse into metals which have a low spin resistance. The general form of the spin resistance, regardless it is of a FM or a NM material is $R_{spin} = \lambda^2\rho/V$, where V is the volume over which the spins can diffuse in each material [6, 7]. In a 1D approximation, in the case of NM materials with a long λ_N, the spin diffuses over a volume $w_N t_N \lambda_N$; FM materials, however, generally have a λ_F smaller than their thickness [5], making the spin current in the FM decay very close to the interface, over a volume $w_N w_F \lambda_F$.

Generally, the voltage measured by the FM detector is normalized to the injected current; the resulting magnitude is called non-local resistance, $R_{NL} = V_S/I$. It is important to note that this is not an electrical resistance, even though it has the same dimensions, because the voltage is measured in a non-local configuration. The measured R_{NL} at the FM detector has a different value depending on the relative magnetization of both FM electrodes. When both electrodes have a parallel (P) magnetization the measured R_{NL} is positive, whereas when they have an antiparallel (AP) magnetization the measured R_{NL} has the same magnitude, but it is negative (see Fig. 2.2(b)), since the second FM now is sensitive to spin-down electrons. This effect is equivalent to the high and low resistance states of the spin valves described in section 1.1, but using pure spin currents. It is called non-local spin valve (NLSV) effect and it can be easily deduced from Eq. 2.7. If we use the same FM material for both electrodes, both P_{Ii} have the same (opposite) sign among each other in a P (AP) magnetization configuration, as well as both α_{Fi} have the same (opposite) sign among each other. The relative magnetization of the FM injector and detector can be easily controlled by sweeping an external magnetic field H (with the same orientation as the easy axis of the

FM electrode, as shown in Fig. 1.3) from positive to negative, and *vice versa* (see section 3.2 for details). Figure 2.3 shows a typical measurement of the non-local resistance as a function of the applied magnetic field. The shape of the R_{NL} *vs.* H curve is the univocal signature of the NLSV effect, and allows us to distinguish the measured voltage due to a pure spin current from leakage currents or other possible artifacts. The difference between the P and AP non-local resistances is defined as the spin signal, ΔR_{NL}, and is tagged in Fig. 2.3.

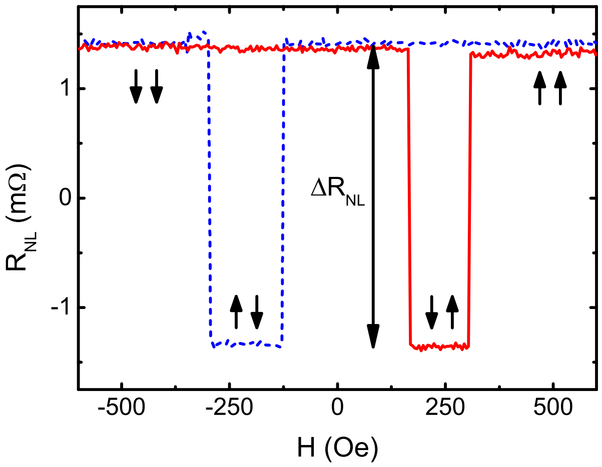

Figure 2.3: Non-local resistance as a function of the applied magnetic field in a permalloy/silver LSV. Solid red (dashed blue) line indicates the increasing (decreasing) direction of the magnetic field. Parallel and antiparallel configurations of the electrode magnetizations, and the spin signal, ΔR_{NL}, are indicated.

Eq. 2.7 holds for all types of FM/NM interfaces. However, there are two limiting cases: (*i*) FM/NM transparent interfaces and (*ii*) FM/NM tunneling interfaces.

Transparent FM/NM interfaces

In this case, there is a direct (ohmic) contact between the FM and the NM metals, and the interface resistance is, thus, negligible: $R_I << R_F, R_N$. In addition, the spin resistance of the FM electrodes is usually lower than the spin resistance of the NM channel [9]. Therefore, we can use the condition $R_I << R_F << R_N$ in order to express Eq. 2.7 as follows [4, 8, 9]:

$$R_{NL} = \frac{2\alpha_{F1}\alpha_{F2}R_N}{\left[2+\frac{R_N\left(1-\alpha_{F1}^2\right)}{R_{F1}}\right]\left[2+\frac{R_N\left(1-\alpha_{F2}^2\right)}{R_{F2}}\right]e^{L/\lambda_N}-\left[\frac{R_N\left(1-\alpha_{F1}^2\right)}{R_{F1}}\right]\left[\frac{R_N\left(1-\alpha_{F2}^2\right)}{R_{F2}}\right]e^{-L/\lambda_N}}. \tag{2.9}$$

The spin signal is twice the value of the non-local resistance and, thus, is expressed as:

$$\Delta R_{NL} = \frac{4\alpha_{F1}\alpha_{F2}R_N}{\left[2+\frac{R_N\left(1-\alpha_{F1}^2\right)}{R_{F1}}\right]\left[2+\frac{R_N\left(1-\alpha_{F2}^2\right)}{R_{F2}}\right]e^{L/\lambda_N}-\left[\frac{R_N\left(1-\alpha_{F1}^2\right)}{R_{F1}}\right]\left[\frac{R_N\left(1-\alpha_{F2}^2\right)}{R_{F2}}\right]e^{-L/\lambda_N}}. \tag{2.10}$$

When both FM electrodes are made of the same material, we can assume $\alpha_{F1} = \alpha_{F2}$ and $R_{F1} = R_{F2}$, further simplifying Eq. 2.10 to:

$$\Delta R_{NL} = \frac{4\alpha_F^2 R_N}{\left[2 + \frac{R_N\left(1-\alpha_F^2\right)}{R_F}\right]^2 e^{L/\lambda_N} - \left[\frac{R_N\left(1-\alpha_F^2\right)}{R_F}\right]^2 e^{-L/\lambda_N}} \ . \tag{2.11}$$

It can be seen from the previous equations that a crucial parameter for a good spin injection is the ratio of the spin resistances, R_N/R_F. This means that for systems where $R_N >> R_F$, the spin injection is not effective. In fact, it happens in most systems because, as stated above, FM metals have a lower spin resistance than NM metals. We can think of a FM as a spin reservoir, where absorbed spins (diffused back from the NM) tend to flip to be parallel to the FM polarization. Therefore, the proximity of the FM electrode disturbs the non-equilibrium spin population present in the NM metal. This problem becomes even worse for the case where, instead of a NM metal, a semiconductor is used, which has a lower conductivity. This problem is known as the conductivity mismatch [10, 11].

Tunneling FM/NM interfaces

An effective way to avoid the conductivity mismatch and have a more efficient spin injection is to place a tunnel barrier in between the FM and the NM materials, because it prevents the spins in the NM from diffusing back into the FM [11]. This corresponds to the second limiting case, where $R_I >> R_N >> R_F$. With this constriction, Eq. 2.7 becomes [2, 4]:

$$R_{NL} = \frac{1}{2} P_{I1} P_{I2} R_N e^{-L/\lambda_N} \ . \tag{2.12}$$

Further simplifying Eq. 2.12 by considering $P_{I1} = P_{I2}$, the following expression for the spin signal is obtained:

$$\Delta R_{NL} = P_I^2 R_N e^{-L/\lambda_N} \ . \tag{2.13}$$

In this case, the non-local resistance and the spin signal only depend on R_N, and no longer on the ratio R_N/R_F.

Despite the enhanced spin-injection efficiency in the presence of tunnel barriers, there is also a main drawback: the electrical current that can be injected from the FM injector into the NM is limited. The reason is that a high current can break the barrier. In addition, by increasing the applied bias, the spin polarization of the interface (P_I) decreases, as it was proven by Valenzuela *et al.* [12]. This occurs because, in the case of tunneling FM/NM interfaces, P_I (Eq. 2.8) is proportional to the difference between the spin-up and spin-down DOS at the FM metal [13], which is smaller above the Fermi level. In the case of transparent FM/NM interfaces, however, DOS above the Fermi level are not accessible and α_F is constant for any applied bias [8].

Being able to inject large electrical currents can be advantageous, as it enhances the spin accumulation at the injecting FM/NM interface and, thus, the voltage measured at the detecting NM/FM interface, increasing the signal-to-noise ratio. In addition, some applications, such as the pure spin current-induced magnetization switching [14, 15], require high current densities, which could not be obtained by using LSVs with tunneling contacts.

2.1.1 Spin-relaxation mechanisms in a NM metal

As it is explicitly seen in Eqs. 2.7-2.13, the spin diffuses throughout the NM channel with a characteristic length, λ_N, which means that a spin current will lose its polarization after traveling a sufficiently large distance. When an electron interacts with its environment, it is subjected to spin-flip scattering events.

In metals, in the absence of magnetic impurities, the origin of the spin flip is dominated by the spin-orbit coupling (SOC), whose Hamiltonian is $\hat{H}_{SO} = C_{SO}\hat{\mathbf{L}}\cdot\hat{\mathbf{S}}$, where $\hat{\mathbf{L}}$ is the orbital angular momentum operator, $\hat{\mathbf{S}}$ is the spin operator and C_{SO} is the SOC constant. The coupling between $\hat{\mathbf{L}}$ and $\hat{\mathbf{S}}$ does not allow m_s to be a "good" quantum number [3]. Hence, including the SOC in the band structure calculation, the resulting Bloch eigenfunctions for conduction electrons must be written as linear combinations of spin-up and spin-down states [16]. Elliott proved that the spin-relaxation time, τ_{sf}, is proportional to the momentum-relaxation time, τ_e, in the form:

$$1/\tau_{sf} = a/\tau_e \ , \tag{2.14}$$

obtaining the following relation between the spin-flip probability, a, and the SOC constant:

$$a \propto \left(\frac{C_{SO}}{\Delta E}\right)^2 \ , \tag{2.15}$$

where ΔE is the average energy difference between the considered conduction band and the nearest band which is coupled *via* the atomic spin-orbit coupling constant [16]. Later on, Yafet showed that Eqs. 2.14 and 2.15 are temperature independent [17], evidencing that the spin-relaxation time has the same temperature dependence as the momentum-relaxation time, which in turn scales with the temperature dependence of the electrical conductivity.

2.2 Spin manipulation

2.2.1 Spin transport in a perpendicular magnetic field: Hanle effect

Eqs. 2.7-2.13 describe the measured non-local resistance as a function of an applied in-plane magnetic field, which is parallel to the magnetization axis of the FM electrodes (as the one shown in Fig. 1.3). This field is applied in order to control the relative magnetization of the electrodes, but it does not alter the polarization of the injected spin current, as both the magnetic field and the spin polarization are parallel. However, when the spin of an electron is subjected to an external perpendicular magnetic field, this will exert a torque on the spin magnetic moment, making it precess around the applied field with the characteristic Larmor's frequency:

$$\omega_L = \frac{g_s \mu_B B}{\hbar} \ , \tag{2.16}$$

where B is the value of the magnetic field in the NM (the other parameters are defined in section 1.1). B is proportional to the applied magnetic field H and, for NM metals, we can approximate $B \sim \mu_0 H$.

If an out-of-plane magnetic field is applied to a LSV during the transport of a pure spin current, as shown in Fig. 2.4(a), the spins will rotate by an angle $\omega_L t$ and the FM detector will detect the projection of such spins onto its own magnetization, *i.e.*, the measured non-local resistance will vary with a $\cos(\omega_L t)$ modulation. In addition to this, the diffusive nature of the spin transport through the NM channel will cause a dispersion in the time that the spins need to travel from the FM injector to the detector, t. Hence, an angular dispersion will occur on the orientation of the spins arriving to the FM injector, which causes the measured spin current at the FM detector to be zero for high enough magnetic fields [18, 19]. This is the so-called Hanle effect. A measurement of this effect is plotted in Fig. 2.4(b) as an example.

In order to model the precession of the spins being diffused through the NM channel, an expression for the non-local resistance can be obtained by solving the Bloch-type equation in the steady state (Bloch equations describe the free precession of a system of spins in a static magnetic field [20]) with an added (1D) spin-diffusion term applied to the LSV geometry [3, 21]:

$$\nabla^2 \vec{\mu}_s = \frac{\vec{\mu}_s}{\lambda_N^2} + \frac{1}{\lambda_m^2} \vec{\mu}_s \times \hat{n} \ , \tag{2.17}$$

where the vector notation of the spin accumulation at the NM channel $\vec{\mu_s}$ refers to the spin polarization direction and $\lambda_m = \sqrt{D\hbar/2\mu_B B}$ is the magnetic length determined by the amplitude of the magnetic field $B\hat{n}$ ($\hat{n}$ is a unit vector along the magnetic field direction).

When the magnetic field is applied in the out-of-plane direction, $\vec{B} = B\hat{z}$, the following expression is obtained for the non-local resistance measured at the FM detector [21]:

$$R_{NL} = \frac{2R_N^\omega \left[\frac{P_{I1}}{1-P_{I1}^2}\left(\frac{R_{I1}}{R_N^\omega}\right)+\frac{\alpha_{F1}}{1-\alpha_{F1}^2}\left(\frac{R_{F1}}{R_N^\omega}\right)\right]\left[\frac{P_{I2}}{1-P_{I2}^2}\left(\frac{R_{I2}}{R_N^\omega}\right)+\frac{\alpha_{F2}}{1-\alpha_{F2}^2}\left(\frac{R_{F2}}{R_N^\omega}\right)\right]\left(\frac{Re\left[\lambda_N^\omega e^{-L/\lambda_N^\omega}\right]}{Re\left[\lambda_N^\omega\right]}\right)}{\left[1+\frac{2}{1-P_{I1}^2}\left(\frac{R_{I1}}{R_N^\omega}\right)+\frac{2}{1-\alpha_{F1}^2}\left(\frac{R_{F1}}{R_N^\omega}\right)\right]\left[1+\frac{2}{1-P_{I2}^2}\left(\frac{R_{I2}}{R_N^\omega}\right)+\frac{2}{1-\alpha_{F2}^2}\left(\frac{R_{F2}}{R_N^\omega}\right)\right]-\left(\frac{Re\left[\lambda_N^\omega e^{-L/\lambda_N^\omega}\right]}{\left[\lambda_N^\omega\right]}\right)^2} \ , \tag{2.18}$$

where $\lambda_N^\omega = \frac{\lambda_N}{\sqrt{1+i\omega_L \tau_{sf}}}$ is an effective spin-diffusion length (λ_N is the previously defined spin-diffusion length of the NM channel) and $R_N^\omega = R_N Re\left[\lambda_N^\omega/\lambda_N\right]$ is an effective spin resistance (R_N is the previously defined spin resistance of the NM channel). If the out-of-plane magnetic field is removed (*i.e.*, if $\omega_L = 0$), Eq. 2.7 is recovered. Therefore, it should be valid for any FM/NM interface.

Very recently, Idzuchi and coworkers have proposed a difference in the spin absorption mechanism for longitudinal and transverse spin currents in FM/NM transparent interfaces [22]. According to this work, the spin absorption by the FM electrodes alters the spatial distribution of the chemical potential and the spin transport is also altered. Therefore, Eq. 2.18 would not be valid, and the following equation is proposed as a correction:

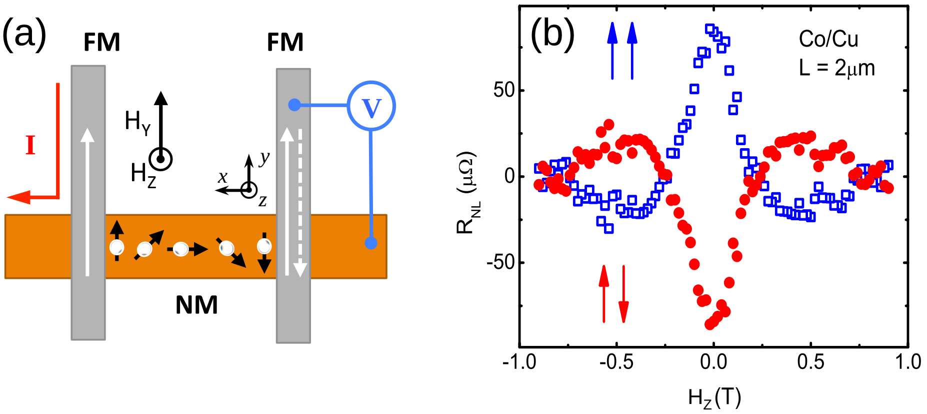

Figure 2.4: (a) Sketch of a LSV where the axes, the direction of the applied in-plane and out-of-plane magnetic field, H_Y and H_Z, materials, measurement configuration, magnetization of the FM electrodes and a sketch of the precession of the spins are shown. (b) Non-local resistance measured as a function of the out-of-plane magnetic field in a cobalt/copper LSV where the distance between FM electrodes is 2 μm. Empty blue squares (solid red circles) correspond to a parallel (antiparallel) configuration of the FM electrodes.

$$R_{NL} = -2R_N \left(\frac{\alpha_{F1}}{1-\alpha_{F1}^2}\frac{R_{F1}}{R_N} + \frac{P_{I1}}{1-P_{I1}^2}\frac{R_{I1}}{R_N}\right)\left(\frac{\alpha_{F2}}{1-\alpha_{F2}^2}\frac{R_{F2}}{R_N} + \frac{P_{I2}}{1-P_{I2}^2}\frac{R_{I2}}{R_N}\right)\frac{C_{12}}{\det(\hat{X})}\ , \tag{2.19}$$

where $\det(\hat{X})$ is the determinant of the matrix $\hat{X}$ and C_{12} is the (1,2) component of the cofactors of $\hat{X}$:

$$\hat{X} = \begin{pmatrix} r_{1\parallel} + \mathrm{Re}\left[\frac{\lambda_N^\omega}{\lambda_N}\right] & \mathrm{Re}\left[\frac{\lambda_N^\omega}{\lambda_N}e^{-L/\lambda_N^\omega}\right] & -\mathrm{Im}\left[\frac{\lambda_N^\omega}{\lambda_N}\right] & -\mathrm{Im}\left[\frac{\lambda_N^\omega}{\lambda_N}e^{-L/\lambda_N^\omega}\right] \\ \mathrm{Re}\left[\frac{\lambda_N^\omega}{\lambda_N}e^{-L/\lambda_N^\omega}\right] & r_{2\parallel} + \mathrm{Re}\left[\frac{\lambda_N^\omega}{\lambda_N}\right] & -\mathrm{Im}\left[\frac{\lambda_N^\omega}{\lambda_N}e^{-L/\lambda_N^\omega}\right] & -\mathrm{Im}\left[\frac{\lambda_N^\omega}{\lambda_N}\right] \\ \mathrm{Im}\left[\frac{\lambda_N^\omega}{\lambda_N}\right] & \mathrm{Im}\left[\frac{\lambda_N^\omega}{\lambda_N}e^{-L/\lambda_N^\omega}\right] & r_{1\perp} + \mathrm{Re}\left[\frac{\lambda_N^\omega}{\lambda_N}\right] & \mathrm{Re}\left[\frac{\lambda_N^\omega}{\lambda_N}e^{-L/\lambda_N^\omega}\right] \\ \mathrm{Im}\left[\frac{\lambda_N^\omega}{\lambda_N}e^{-L/\lambda_N^\omega}\right] & \mathrm{Im}\left[\frac{\lambda_N^\omega}{\lambda_N}\right] & \mathrm{Re}\left[\frac{\lambda_N^\omega}{\lambda_N}e^{-L/\lambda_N^\omega}\right] & r_{2\perp} + \mathrm{Re}\left[\frac{\lambda_N^\omega}{\lambda_N}\right] \end{pmatrix},$$

and

$$C_{12} = \begin{vmatrix} \mathrm{Re}\left[\frac{\lambda_N^\omega}{\lambda_N}e^{-L/\lambda_N^\omega}\right] & -\mathrm{Im}\left[\frac{\lambda_N^\omega}{\lambda_N}e^{-L/\lambda_N^\omega}\right] & -\mathrm{Im}\left[\frac{\lambda_N^\omega}{\lambda_N}\right] \\ \mathrm{Im}\left[\frac{\lambda_N^\omega}{\lambda_N}\right] & r_{1\perp} + \mathrm{Re}\left[\frac{\lambda_N^\omega}{\lambda_N}\right] & \mathrm{Re}\left[\frac{\lambda_N^\omega}{\lambda_N}e^{-L/\lambda_N^\omega}\right] \\ \mathrm{Im}\left[\frac{\lambda_N^\omega}{\lambda_N}e^{-L/\lambda_N^\omega}\right] & \mathrm{Re}\left[\frac{\lambda_N^\omega}{\lambda_N}e^{-L/\lambda_N^\omega}\right] & r_{2\perp} + \mathrm{Re}\left[\frac{\lambda_N^\omega}{\lambda_N}\right] \end{vmatrix}.$$

The terms $r_{i\parallel}$ and $r_{i\perp}$ have the expressions:

$$r_{i\parallel}\left(\frac{2}{1-P_{Ii}^2}\frac{R_{Ii}}{R_N} + \frac{2}{1-\alpha_{Fi}^2}\frac{R_{Fi}}{R_N}\right) \text{ and } r_{i\perp} = \frac{1}{R_N w_F w_N G_{ri}}\ ,$$

where $i = 1, 2$ refer to each interface and G_{ri} is the real part of the spin-mixing interface conductance per unit area [29, 30].

2.2.2 Spin transport on top of a FM insulator

The interaction between the magnetization of a FM insulator (FMI) and a spin current can be an effective way of spin manipulation, and it lies at the basis of the recently discovered spin Hall magnetoresistance (SMR) [23–28]. SMR is based on the spin-mixing conductance concept [29,30] at NM/FMI interfaces, which is also present in alternative spin-injection methods, such as spin pumping [31] and spin Seebeck [32], mentioned in section 1.2.2. According to this, when a spin current is driven through a metal which is in direct contact with a FMI, if the spin polarization $\vec{s}$ and the magnetization vector $\vec{M}$ of the FMI are non-collinear, part of the spin current will be absorbed by $\vec{M}$ *via* spin-transfer torque [33–35], leading to a maximum spin absorption in the case where $\vec{M}$ and $\vec{s}$ are perpendicular.

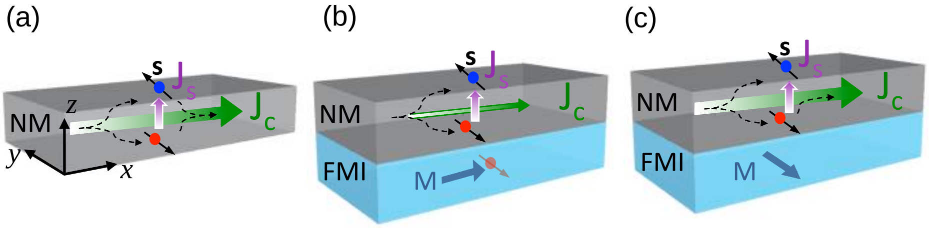

Figure 2.5: Schematic representation of the SMR. (a) NM layer with strong SOC. A charge current $\vec{J_C}$ is driven in the $\vec{x}$ direction, which, by means of SHE, generates a spin current $\vec{J_S}$ in the $\vec{z}$ direction with a spin polarization $\vec{s}$ in the $\vec{y}$ direction. The spin current is reflected back at the surfaces, generating an additional charge current by means of ISHE. (b) NM/FMI bilayer. The magnetization $\vec{M}$ of the FMI is perpendicular to $\vec{s}$, leading to an absorption of the spin current at the interface as a spin-transfer torque. (c) NM/FMI bilayer. In this case, $\vec{M}$ and $\vec{s}$ are parallel and no spin absorption will take place. Figure adapted from Ref. [28]

SMR was first discovered in 2013 by Nakayama and coworkers [23] in yttrium iron garnet (YIG, $Y_3Fe_5O_{12}$)/platinum (Pt) bilayers (more precisely, Pt Hall bars fabricated on top of YIG). Being Pt a strong SOC material, when a charge current $\vec{J_C}$ is driven through it in the $\hat{x}$ direction (see Fig. 2.5(a)), a transverse spin current $\vec{J_S}$ is created by means of SHE in the out-of-plane direction ($\hat{z}$), with a spin polarization $\vec{s}$ perpendicular to both $\vec{J_C}$ and $\vec{J_S}$ ($\hat{y}$ direction). In the absence of a FMI, the created spin current is reflected back at the interfaces of Pt with the substrate and with the vacuum, inducing an additional charge current by means of ISHE along the same direction as the original one [36]. If a FMI (such as YIG) is placed below the Pt, when the $\vec{M}$ of the FMI and $\vec{s}$ are perpendicular, part of the spin current will be absorbed by $\vec{M}$ as a spin-transfer torque (see Fig. 2.5(b)) and the measured current will be smaller (*i.e.*, the measured electrical resistance will be higher). When $\vec{M}$ and $\vec{s}$ are parallel, however, no spin absorption will take place (see Fig. 2.5(c)) and the spin current will be reflected back into the Pt as in the case where no FMI is placed below. The measured electrical resistance will be, thus, low. Hence, by varying the relative orientation between $\vec{M}$ and $\vec{s}$ one can control the electrical resistance measured in the Pt.

According to the current model of SMR, the measured resistivities in the longitudinal (ρ_L) and transverse (ρ_T) configurations can be formulated as [23,24]:

$$\rho_L = \rho_0 - \Delta\rho m_y^2 \ , \tag{2.20}$$

$$\rho_T = \rho_{AH} m_z + \Delta\rho m_x m_y \ , \tag{2.21}$$

where $\vec{m} = (m_x, m_y, m_z)$ is the unitary vector in the direction of the magnetization $\vec{M}$, ρ_0 is the baseline resistivity of the NM layer, ρ_{AH} accounts for an anomalous Hall-like contribution and $\Delta\rho$ is the resistivity change due to SMR. The torque that $\vec{M}$ exerts on $\vec{s}$ when both vectors are neither parallel nor perpendicular, generates a reflected spin current with a rotated spin polarization, which gives rise to a charge current also in the $\hat{y}$ direction. The variation of such current generates the transverse SMR, with a maximum at $\alpha = 45°$. $\Delta\rho$ is related to the microscopic properties of the NM layer by:

$$\frac{\Delta\rho}{\rho_0} = \theta_{SH}^2 \frac{\frac{2\rho_0\lambda_N^2}{t_N} G_r \tanh^2\frac{t_N}{2\lambda_N}}{1 + 2\rho_0\lambda_N G_r \coth\frac{t_N}{\lambda_N}} \ , \tag{2.22}$$

where θ_{SH}, λ_N and t_N are the spin Hall angle, the spin-diffusion length and the thickness of the NM layer, respectively, and G_r is the real part of the spin-mixing conductance per unit area of the Pt/YIG interface.

Figure 2.6 shows the angle-dependent magnetoresistance (ADMR) of a Pt/YIG sample. The ADMR was measured at a constant magnetic field (H) in the three relevant H-rotation planes defined in the sketches of Fig. 2.6 (corresponding to the variation of the angles α, β and γ) in the longitudinal configuration, as well as a function of α in the transverse configuration. The ADMR measurements in all the configurations give the following results: (*i*) no resistance modulation is observed in $R_L(\gamma)$, (*ii*) a large modulation is observed in $R_L(\alpha)$ and $R_L(\beta)$, with the same amplitude and a $\cos^2$ dependence, and (*iii*) $R_T(\alpha)$ shows a $\sin\alpha \cdot \cos\alpha$ dependence, with the same amplitude as in $R_L(\alpha)$ but with reduced amplitude due to a geometrical factor. These results are in perfect agreement with Eqs. 2.20 and 2.21.

In addition of its potential applications, SMR is interesting from the fundamental point of view, as it allows to probe FMI/NM interfaces [28] and to extract information from them, such as the value of G_r. However, it is not directly the spin current what is measured by this method, but the charge current generated from it, which can lead to spurious effects as suggested by some authors [37,38]. In addition, the SOC, present in the materials that can be tested with this method, can alter the obtained G_r [39].

In order to eliminate any possible artifacts and be able to test low SOC materials, the interaction between pure spin currents and FMIs is proposed in this thesis by fabricating LSVs on top of YIG. This will lead to a novel method of spin manipulation by magnetic gating of pure spin currents. The details will

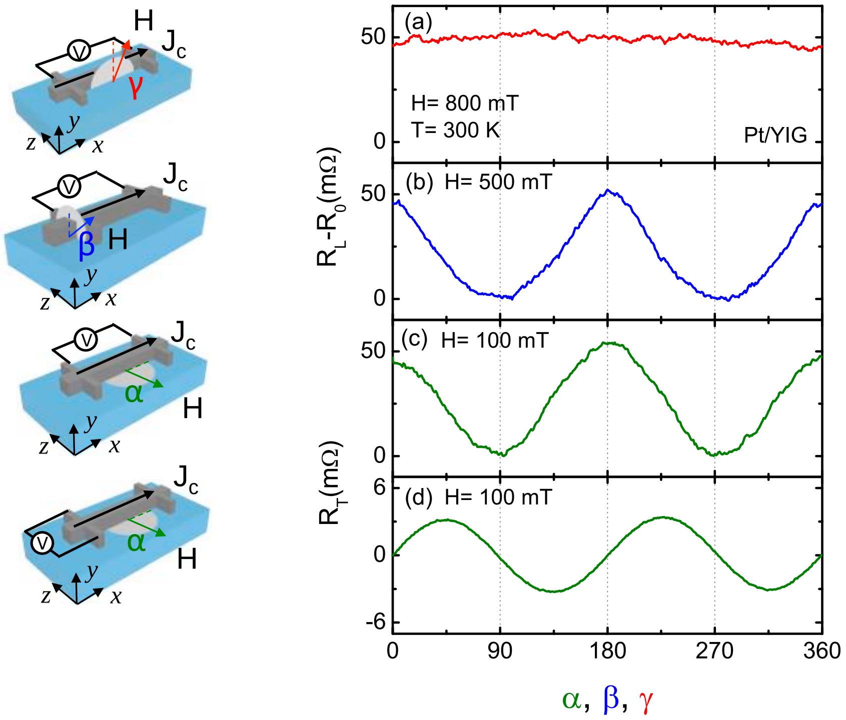

Figure 2.6: Angle-dependent magnetoresistance measurements for a Pt/YIG sample. $R_{L,T}$ is the measured resistance and $R_{L0,T0}$ is the subtracted background. The configuration of each measurement is sketched next to each plot. (a-c) Longitudinal resistance R_L as a function of the direction of the applied magnetic field, in three different rotation planes (angles α, β and γ). (d) Transverse resistance R_T as a function of the angle α. Figure adapted from Ref. [28].

be explained in Chapter 8.

References

[1] T. Valet and A. Fert, Phys. Rev. B **48**, 7099 (1993).

[2] F. J. Jedema, M. S. Nijboer, A. T. Filip, and B. J. van Wees, Phys. Rev. B **67**, 085319 (2003).

[3] M. Johnson and R. H. Silsbee, Phys. Rev. B **37**, 5312 (1988).

[4] S. Takahashi and S. Maekawa, Phys. Rev. B **67**, 052409 (2003).

[5] S. Dubois, L. Piraux, J. M. George, K. Ounadjela, J. L. Duvail, and A. Fert, Phys. Rev. B **60**, 477 (1999).

[6] A. Fert and H. Jaffrès, Phys. Rev. B **64**, 184420 (2001).

[7] A. Fert, J.-M. George, H. Jaffrès, and R. Mattana, IEEE Trans. Electron. Devices 54, 921 (2007).

[8] F. Casanova, A. Sharoni, M. Ehrekhinsky, and I. K. Schuller, Phys. Rev. B **79**, 184415 (2009).

[9] T. Kimura, J. Hamrle, Y. Otani, Phys. Rev. B **72**, 014461 (2005).

[10] G. Schmidt, D. Ferrand, L. W. Molenkamp, A. T. Filip, and B. J. van Wees, Phys. Rev. B **62**, R4790 (2000).

[11] E. I. Rashba, Phys. Rev. B **62**, R16 267 (2000).

[12] S. O. Valenzuela, D. J. Monsma, C. M. Marcus, V. Narayanamurti, and M. Tinkham, Phys. Rev. Lett. **94**, 196601 (2005).

[13] R. Mersevey and P. M. Tedrow, Phys. Rep. **238**, 173 (1994).

[14] T. Kimura, Y. Otani, and J. Hamrle, Phys. Rev. Lett. **96**, 037201 (2006).

[15] T. Yang, T. Kimura, and Y. Otani, Nat. Phys. **4**, 851 (2008).

[16] R. J. Elliott, Phys. Rev., **96**, 266 (1954).

[17] Y. Yafet, in *Solid State Physics*, edited by F. Seitz and D. Turnbull (Academic, New York, 1963), pp. 1-98.

[18] F. J. Jedema, H. B. Heersche, A. T. Filip, J. J. A. Baselmans, and B. J. van Wees, Nature **416**, 713 (2002).

[19] J.-C. Rojas Sánchez, P. Łączkwoski, W. F. Savero Torres, M. Cubukcu, V. D. Nguyen, L. Notin, C. Beigné, C. Vergnaud, A. Marty, M. Jamet, L. Vila, and J. P. Attané, Appl. Phys. Lett. **102**, 132408 (2013).

[20] *Introduction to Solid State Physics*, C. Kittel (John Wiley & Sons, 8th Edition, 2005).

[21] Y. Fukuma, L. Wang, H. Idzuchi, S. Takahashi, S. Maekawa, and Y. Otani, Nat. Mater. **10**, 527 (2011).

[22] H. Idzuchi, Y. Fukuma, S. Takahashi, S. Maekawa, and Y. Otani, Phys. Rev. B **89**, 081308(R) (2014).

[23] H. Nakayama, M. Althammer, Y.-T. Chen, K. Uchida, Y. Kajiwara, D. Kikuchi, T. Ohtani, S. Geprägs, M. Opel, S. Takahashi, R. Gross, G. E. W. Bauer, S. T. B. Goennenwein, and E. Saitoh, Phys. Rev. Lett. **110**, 206601 (2013).

[24] Y.-T. Chen, S. Takahashi, H. Nakayama, M. Althammer, S. T. B. Goennenwein, E. Saitoh, and G. E. Bauer, Phys. Rev. B **87**, 144411 (2013).

[25] N. Vliestra, J. Shan, V. Castel, and B. J. van Wees, Phys. Rev. B **87**, 184421 (2013).

[26] C. Hahn, G. de Loubens, O. Klein, M. Viret, V. V. Naletov, and J. Ben Youssef, Phys. Rev. B **87**, 174417 (2013).

[27] M. Weiler, M. Althamer, M. Schreier, J. Lotze, M. Pernpeintner, S. Meyer, H. Huebl, R. Gross, A. Kamra, J. Xiao, Y.-T. Chen, H. Jiao, G. E. W. Bauer, and S. T. B. Goennenwein, Phys. Rev. Lett. **111**, 176601 (2013).

[28] M. Isasa, A. Bedoya-Pinto, F. Golmar, F. Sánchez, L. E. Hueso, J. Fontcuberta, and F. Casanova, Appl. Phys. Lett. **105**, 142402 (2014).

[29] A. Brataas, Y. V. Nazarov, and G. E. W. Bauer, Phys. Rev. Lett. **87**, 2481 (2000).

[30] A. Brataas, Y. V. Nazarov, and G. E. W. Bauer, Eur. Phys. J. B **22**, 99 (2001).

[31] Y. Kajiwara, H. Harii, S. Takahashi, J. Ohe, K. Uchida, M. Mizuguchi, H. Umezawa, H. Kawai, K. Ando, K. Takanashi, S. Maekawa, and E. Saitoh, Nature **464**, 262 (2010).

[32] K. Uchida, J. Xiao, H. Adachi, J. Ohe, S. Takahashi, J. Ieda, T. Ota, Y, Kajiwara, H. Umezawa, H. Kawai, G. E. W. Bauer, S. Maekawa, and E. Saitoh, Nature Mater. **9**, 894 (2012).

[33] J. C. Slonczewski, J. Magn. Magn. Mater. **159**, L1 (1996).

[34] D. C. Ralph and M. D. Stiles, J. Mag. Magn. Mater **320**, 1190 (2008).

[35] X. Jia, K. Liu, K. Xia, and G. E. Bauer, Europhys. Lett. **96**, 17005 (2011).

[36] M. I. Dyakonov, Phys. Rev. Lett. **99**, 126601 (2007).

[37] S. Y. Huang, X. Fan, D. Qu, Y. P. Chen, W. G. Wang, J. Wu, T. Y. Chen, J. Q. Xiao, and C. L. Chien, Phys. Rev. Lett. **109**, 107204 (2012).

[38] Y. M. Lu, J. W. Cai, S. Y. Huang, D. Qu, B. F. Miao, and C. L. Chien, Phys. Rev. B **87**, 220409 (2013).

[39] A. B. Cahaya, O. A. Tretiakov, and G. E. W. Bauer, Appl. Phys. Lett. **104**, 042402 (2014).

Chapter 3

Experimental techniques

3.1 Fabrication of the lateral spin valves

Figure 3.1 contains the design of one of the samples employed in this thesis. In a first stage, the aim of fabricating the samples is to obtain the spin-diffusion length of the NM metal (λ_N) and the spin polarization of the FM metal (α_F) and/or the interface (P_I). In order to do so, the measured spin signal (ΔR_{NL}) is fitted to Eq. 2.7 (or Eqs. 2.10 and 2.13 depending on the characteristics of the FM/NM interface). As seen from the equations, several geometrical parameters can be used in order to perform the fitting. Due to its exponential dependence with the distance between the FM electrodes (L), and the fact that this parameter is easily controlled experimentally, in this work the measured ΔR_{NL} *vs* L was fitted (see Chapter 4 for a detailed explanation). In order to avoid the dispersion that could be originated by using different devices, all the measurements are performed in the same device. Hence, each device consists of several LSVs, with different edge-to-edge distances L between the FM electrodes, all of them connected by the same NM channel. The electrodes need to be long (~ 3 μm) and narrow ($\sim$ 100-150 nm) so that their magnetization axis is well defined by means of shape anisotropy; in addition to that, the FM injector and the detector have different widths, allowing them to have different coercive fields, H_C. This way, the magnetization will switch for different values of the applied magnetic field, so that both parallel (P) and antiparallel (AP) magnetization configurations can be achieved. The NM metal needs to be narrow ($\sim$ 150-200 nm) to channel the diffusion of the spins and force them to travel longer distances, which validates the 1D approach used to obtain Eq. 2.7.

In order to electrically contact the LSVs, they are connected to contact pads (see Fig. 3.1). These contact pads are small near the LSVs (we will call them microscopic contact pads), and they get progressively bigger as they approach the edges of the substrate (macroscopic contact pads).

The fabrication method employed in this thesis is electron (e)-beam lithography (eBL), which includes e-beam exposure of a resist, developing, ultra high vacuum (UHV) evaporation and lift-off. All these steps are described in detail in the following section. Two consecutive eBL processes were employed in order to fabricate the LSVs.

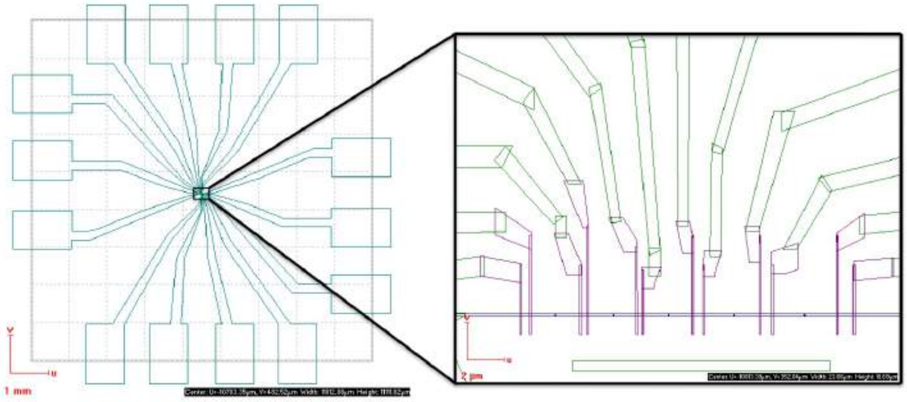

Figure 3.1: GDS design of one of the devices used in this thesis. The macroscopic contact pads shown in the left are connected to the microscopic contact pads and the six LSVs, all connected with the same NM channel.

3.1.1 Single e-beam lithography process

Figure 3.2 schematically shows the steps involved in a standard eBL process, which are listed and briefly described below.

1. **Spin coating:** An *e*-beam sensitive polymer, often called resist, is spin coated onto a SiO_2 (150 nm)/Si substrate. Generally, two resist layers are used in order to create an undercut (see Fig. 3.3) and facilitate the lift-off process (details are given in section 3.1.2).

   Polymethylmethacrylate (PMMA) resists are used, with different molecular weights and anisole (A) concentrations. 495k PMMA A2/950k PMMA A2 and 495k PMMA A4/950k PMMA A2 bilayers are used. The resists with lowest molecular weight (495k) are more sensitive to the *e*-beam and are, thus, coated below in order to create the undercut. The thickness of the resist layer, controlled by the anisole concentration, will be chosen depending on the desired metal thickness: for metal thicknesses <40 nm, 495k PMMA A2 will be used (with a thickness of $\sim$ 50 nm, the same as 950k PMMA A2) whereas, for thicker depositions, 495k PMMA A4 will be used ($\sim$ 200 nm thick). All of them are positive resists, *i.e.*, the part of the resist that is subjected to e-beam exposure is removed. The resists are spin coated at 4000 *rpm* for 1 minute and baked, afterwards, at 195 °C for 1 minute in a hot plate.

2. **E-beam exposure:** An *e*-beam is used to scan (or ”write”) the resist according to a desired pattern (in the form of a GDS design) and modify the bonds of the polymers.

   Two different eBL tools by *Raith GmbH* (Germany) were used: Raith 150-TWO and Raith e-line +. Both tools permit to expose a large area thanks to the laser interferometer of the sample holder, which result in a precise stitching between different write fields. In addition, a precise alignment

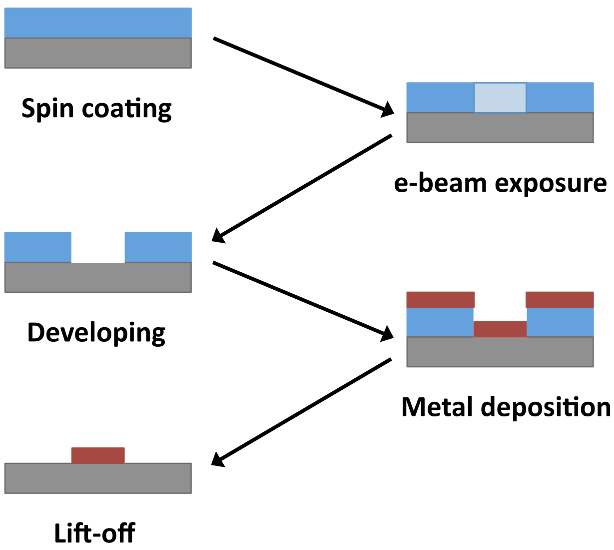

Figure 3.2: Scheme of the different steps involved in a positive eBL process.

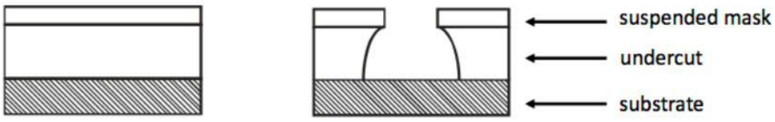

Figure 3.3: Double layer of positive resist on top of a substrate (on the left) and the undercut that is created after the e-beam exposure (on the right).

procedure permits to write a pattern on top of a previously patterned sample with an error <30 nm.

The e-beam parameters typically employed in this work were a voltage of 10 kV and an aperture of 10 μm, which correspond to a beam current of ~20 pA. Write fields of 100×100 (or 200×200) μm^2 and a dose of ~150 $\mu C/cm^2$ were used.

3. **Developing:** The exposed resist is removed by chemically breaking its bonds (in the case of positive resists).

   With this purpose, the exposed sample is introduced in MIBK:IPA 1:3 (a dilution of methyl isobuthyl ketone in isopropanol) for 20 to 60 seconds and rinsed, afterwards, in IPA.

4. **Metal deposition:** A metal is deposited on top of the substrate and the resist.

   A UHV evaporator was used by *Createc GmbH* (Germany), with a base pressure $\leqslant 1 \times 10^{-8}$ mbar. This equipment consists of 4 pockets for *e*-beam evaporation and six ports available for effusion cells.

5. **Lift-off:** The sample is introduced in acetone in order to dissolve the resist. Therefore, the metal deposited on top of the resist will be lifted off, and only the metal deposited directly onto the substrate will remain.

3.1.2 Our recipe: two consecutive lithography processes

As explained above, for the fabrication of the LSVs, two consecutive eBL processes are employed: in the first process the FM electrodes are patterned, 35 nm of permalloy ($Ni_{81}Fe_{19}$, Py) or cobalt (Co) are *e*-beam evaporated and the lift-off is performed; in the second process the NM channel and the microscopic contact pads are patterned, 40 to 150 nm of Cu are evaporated and the lift-off is done. The electrodes are placed below the NM channel in order to avoid their shape distortion, which could lead to the formation multiple magnetic domains and even physically break the electrodes.

The most crucial part of employing two consecutive eBL steps is to obtain high quality FM/NM interfaces that will favor the spin injection. With this purpose, two main concerns have to be taking into account: (*i*) the FM electrodes need to be smooth and not to have the sharp edges sometimes originated after the lift-off process; (*ii*) the resistance of the FM/NM interface needs to be the desired one.

Removal of the sharp edges

If the deposited material is hard, it is very likely that sharp vertical edges (often called *ears* or *horns*) are formed in the structure after the lift-off, such as the ones shown in Fig. 3.4(a). In order to avoid the formation of the sharp edges, it is very important to use a double resist layer for the *e*-beam lithography, so that an undercut (Fig. 3.3) is formed, and to use a directional metal-deposition technique, *i.e.*, evaporation instead of sputtering. This prevents the metal from sticking into the walls of the resist, facilitating the lift-off process. We have observed (Fig. 3.4) that UHV evaporation gives better results than HV evaporation, because it helps in the directionality of the evaporated metal. Finally, even when the evaporation is done under UHV conditions, some edges are likely to be formed; however, they are smaller than the ones formed by sputtering or HV evaporation and they can easily be removed by performing an argon (Ar)-ion milling at a grazing incidence. An equipment from *4-wave Inc.* (USA) was used. The optimal parameters for the Ar-ion milling were found to be an Ar flow of 15 standard cubic centimeters per minute (sccm), an acceleration voltage of 50 V, a beam current of 50 mA, and a beam voltage of 300 mV during 3 minutes. The result is shown in Fig. 3.4(b), where smooth Py electrodes are observed.

Resistance of FM/NM interfaces

Two types of FM/NM interfaces are employed throughout this thesis: (*i*) transparent interfaces and (*ii*) interfaces with a non-zero resistance.

In the first case, in order to be sure of the validity of the study performed in Chapter 5, it is crucial to ensure transparent interfaces. In addition, the spin-injection efficiency at a transparent junction is very sensitive to the interface

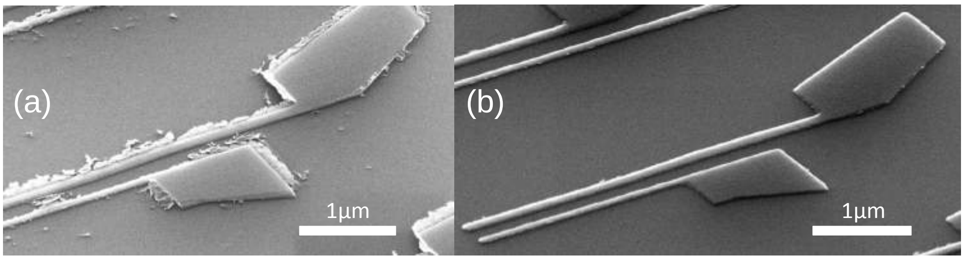

Figure 3.4: SEM image of Py electrodes deposited under (a) HV conditions and (b) UHV conditions. In the first case, sharp edges are formed after the lift-off. In the second case, the lift-off is followed by a grazing-incidence Ar-ion milling, which results in smooth structures.

quality [1–3]. Therefore, the surface of the FM electrodes needs to be cleaned from oxidation and resist left-overs by Ar-ion milling prior to the Cu deposition.

In order to optimize the interface cleaning process, the spin polarization of the FM, α_F, was obtained for different samples in which the Ar-ion milling time was systematically changed. α_F is obtained from the fitting of our measurements to Eq. 2.10, as explained in detail in Chapter 4, and is directly related to the spin-injection efficiency $\gamma = \left(\frac{2\alpha_F \lambda_F \rho_F}{1-\alpha_F^2}\right)^2$ [4]. The other milling parameters were kept constant with an Ar flow of 15 sccm, an acceleration voltage of 50 V, a beam current of 50 mA, and a beam voltage of 300 V. Figure 3.5 shows the spin polarization of Py as a function of the Ar-ion milling time, where α_{Py} increases with time as expected from the interface cleaning process in which the resist left-overs and the oxide are being removed. After a maximum value of $\alpha_{Py} = 0.39 \pm 0.01$ is obtained for a milling time of 30 s, the value of α_{Py} starts to decrease for longer times. This can be understood by the fact that the milling process increases the roughness of the FM surface (as checked by an atomic force microscope) once it is completely cleaned, leading to a rougher interface with reduced spin-injection efficiency. It is worth noting that the Ar-ion milling was not performed *in situ*, *i.e.*, the vacuum was broken to place the sample into the Cu evaporation chamber. However, this is shown not to be crucial for obtaining a transparent interface with the highest spin polarization.

The interface resistance was measured in some of the optimized devices where a cross-shaped junction was added to the original design. The value of the measured resistance was negative in all junctions. This is an artifact which occurs when the resistance of the electrodes is on the order or higher than the interface resistance [5, 6] due to an inhomogeneous current distribution in this geometry. We can estimate the value of the interface resistance multiplied by the area to be $R_I A_I \leqslant 1 \times 10^{-3}$ $\Omega\mu\text{m}^2$ confirming that we are, indeed, in the transparent regime [7].

In the case of Co electrodes, this procedure is more tricky. Although highly reproducible results are generally obtained (as shown in Chapter 4), when the Cu deposition is not done immediately after the interface milling, an oxide layer is formed in Co, leading to non-transparent interfaces. This, however, can also

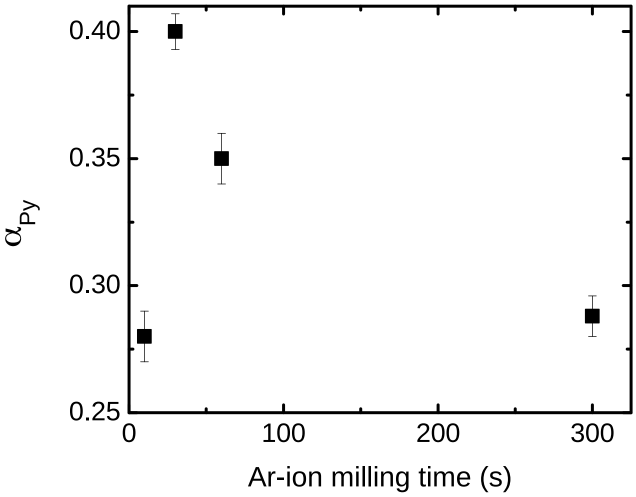

Figure 3.5: Spin polarization of Py as a function of the Ar-ion milling time. The error bars correspond to the fitting of the data to Eq. 2.10.

be an advantage, as in the case of Chapters 7 and 8, where the Co is oxidized on purpose after the milling and before the Cu deposition. Interface resistances of $\sim 1-5\ \Omega$ are obtained, which are needed in order to study the effect of the interface resistance in the analysis of Hanle measurements, as well as to enhance the spin injection [7]. It is important to note that, even when a non-zero interface resistance is desired, the interface milling is not skipped, otherwise the resist left-overs do not allow a good spin injection.

Connecting the device to the macroscopic world

The procedure described above accounts for the fabrication of the microscopic part of the device, shown in Fig. 3.6. However, in order to perform the electrical measurements, it is necessary for the devices to have some macroscopic contact pads, which allow the electrical connection between the device and the electrical measurement setup (described in section 3.2).

For most samples, photolithography is used in order to fabricate the macroscopic contact pads before the fabrication of the microscopic LSVs: a standard 1×1 cm mask with 16 contact pads is used for the UV-light exposure of a photoresist, $\sim 30-50$ nm of titanium (Ti)/gold (Au) are evaporated and the lift-off is done. Afterwards, both eBL processes are performed on top of the macroscopic contacts. A complete sample is shown in Fig 3.7.

When the design of the samples is not compatible with the standard photolithography mask, the macroscopic contact pads are patterned by eBL, right after the patterning of the NM channel and the microscopic pads, doing a single Cu deposition for the NM channel and the microscopic and macroscopic contact pads. The employed beam parameters for the macroscopic contacts were a voltage of 10 kV and an aperture of 120 μm, which correspond to a beam current of $\sim$3.5 nA; write fields of $1000\times1000\ \mu\text{m}^2$ and a dose of $\sim$150-200 $\mu\text{C/cm}^2$ were used. This way, the patterning process was faster, as there is no need for a high resolution.

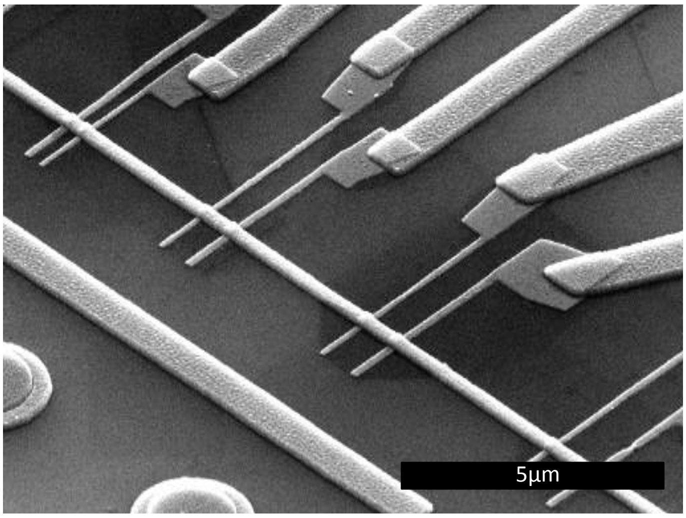

Figure 3.6: SEM image of the microscopic part of a completed device, where five different LSVs, together with the microscopic contact pads, can be seen.

3.1.3 Nanofabrication on top of insulating substrates

As mentioned in section 2.2.2, a new method for spin manipulation is proposed and developed in Chapter 8 by fabricating LSVs on top of FM insulators. The fabrication of nanostructrures on top of insulating substrates is not trivial [8] and it deserves a special mention.

If the standard eBL process is used, the substrate gets charged during the *e*-beam exposure, with the subsequent distortion of the pattern. In order to avoid this, a thin Au layer of 2.5 nm is sputtered on top of the PMMA resist before the *e*-beam exposure. The Au conducts the electrons avoiding the charging of the substrate but, at the same time, it is thin enough to allow the interaction between the *e*-beam and the resist. After the exposure and before developing the patterned resist, the Au layer is removed with a commercial Au etchant from *Sigma Aldrich Inc.* (USA) by introducing the sample in the etchant for 2 seconds.

3.2 Electrical measurements

All the electrical measurements were performed in a commercial Physical Property Measurement System (PPMS) from *Quantum Design Inc.* (USA), a liquid He cryostat whose temperatures range from 400 K to 2 K. In addition, it is equipped with a superconducting magnet which can reach magnetic fields of ± 9 T.

The samples are mounted on a puck that allows for eight different electrical connections, *via* copper wires which are bonded to the macroscopic part of the sample by cold indium pressing (see Fig. 3.7(a)). The puck is pinned into a rotating sample holder (Fig. 3.7(b)), connected to a motor located outside the PPMS. Even if the magnetic field is always applied in the same direction, the rotating system and the different geometries of the available sample holders allow to vary the relative position between the sample and the magnetic field.

A four-point configuration is used for the measurements, which provides two probes for driving an electrical current and two different probes for sensing the

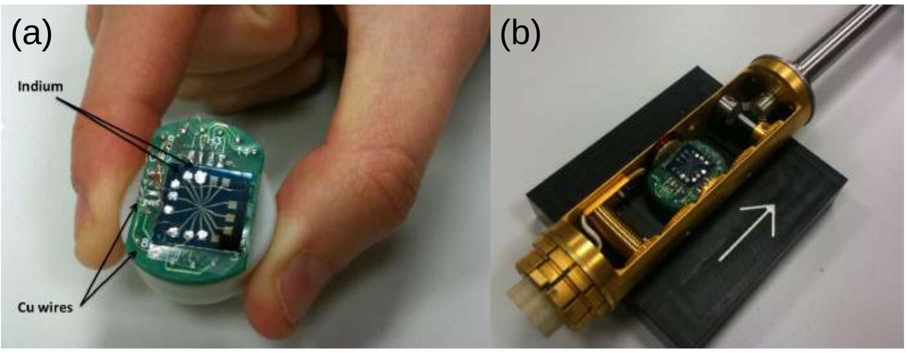

Figure 3.7: (a) Sample mounted on a PPMS puck. Copper wires and indium contacts are indicated. (b) Puck mounted on the rotating sample holder, ready to introduce in the PPMS.

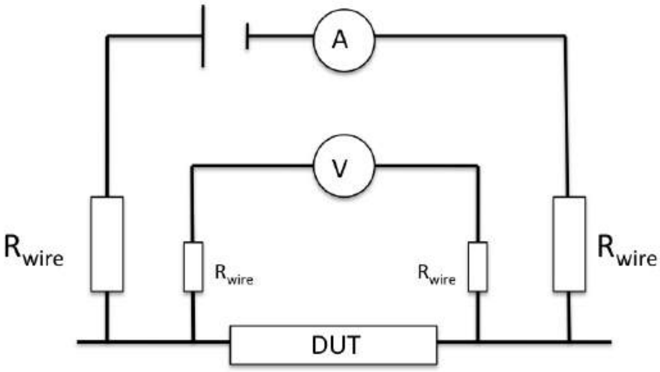

Figure 3.8: Schematic representation of a four-point measurement used for eliminating the contribution of the contact resistances and being able to measure solely the resistance of the device under test (DUT).

voltage in order to eliminate the resistance of the wires and the contacts.The principle of the four-point configuration is sketched in Fig. 3.8. When a current is driven into a device under test (DUT), there is a voltage drop also across the wires of the current source. Therefore, if the voltmeter is integrated in the current source (as it is the case for the usual two-point measurements), there will be a significant error in the voltage measured. This is why we use two additional probes to measure the voltage drop. The voltmeter has a very high impedance and almost no current flows across its wires, reducing their voltage drop contribution. Figure 3.9(a) shows an example of a four-point resistance measurement in a LSV, performed in order to obtain the resistivity of the NM channel. The configuration shown in Fig. 3.9(b), which is performed in order to obtain the resistance of the interface, obeys the same principle. Finally, Fig. 3.9(c) shows the non-local measurement configuration; in this case, the four-point measurement is not performed in order to eliminate the resistance of the wires, but because this kind of measurements can only be done with four probes.

In addition to reducing the noise coming from the resistance of the wires and contacts, the thermal noise was reduced by using the "DC reversal" technique.

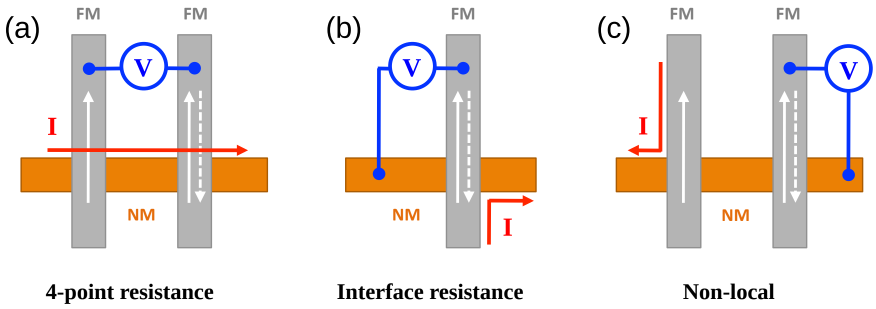

Figure 3.9: Schematic representation of the measurement configurations employed in this thesis: (a) four-point resistance measurements, (b) Interface resistance measurements and (c) non-local measurements.

This is crucial for our work, because resistances of the order of $m\Omega$ need to be measured. The ”DC reversal” technique is an alternative to lock-in (which consists in applying an AC current and filtering out all the frequencies of the measured AC voltage except of the one coming from the current), which reduces the impact of error sources, as well as the time required to achieve a low noise measurement [9]. Furthermore, using DC currents allows one to perform measurements with a defined current polarity.

This method assumes that the thermal noise has two contributions: a constant offset, V_{EMF}, and a thermoelectric voltage that changes linearly with time, δV (see Fig. 3.10). The ”DC reversal” technique consists in making three different measurements over a period of time, alternating the current polarity. These three measurements are the following:

$$V_{M1} = V_{DUT} + V_{EMF} \ , \tag{3.1}$$
$$V_{M2} = -V_{DUT} + V_{EMF} + \delta V \ , \tag{3.2}$$
$$V_{M3} = V_{DUT} + V_{EMF} + 2\delta V \ . \tag{3.3}$$

V_{EMF} and δV can be cancelled the following way:

$$V_A = (V_{M1} - V_{M2})/2 = V_{DUT} - \delta V/2 \ , \tag{3.4}$$
$$V_B = (V_{M3} - V_{M2})/2 = V_{DUT} + \delta V/2 \ . \tag{3.5}$$

This eliminates the constant offset, but still a linear term remains. However, averaging between the two values V_A and V_B, will provide the voltage drop over the DUT:

$$V_{final} = (V_A + V_B)/2 = (V_{M1} - 2V_{M2} + V_{M3})/4 = V_{DUT} \ . \tag{3.6}$$

The connections of the puck are connected to an automatic switch board that allows us to change the configuration of the current and voltage probes while the sample is inside the PPMS cryostat. The switch board is connected to a *Keithley* nanovoltmeter (model 2182) and to a *Keithley* DC/AC current source (model 6221). The measurement configurations, the nanovoltmeter and

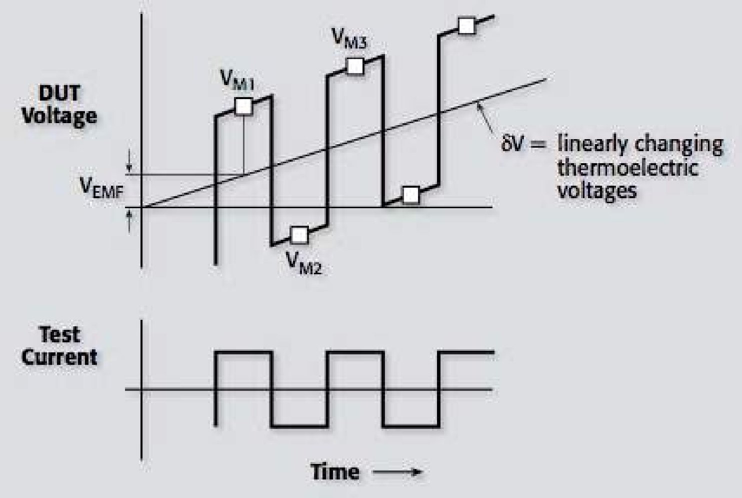

Figure 3.10: Schematic representation of the "DC reversal" measurement technique. Figure taken from Ref. [9].

the source, as well as the temperature and magnetic field inside the PPMS, are controlled by a Labview program, designed to measure the resistance as a function of the temperature, $R(T)$, the magnetic field, $R(H)$, and the rotation angle of the sample holder, $R(\alpha)$.

References

[1] Y. Ji, A. Hoffmann, J. E. Pearson, and S. D. Bader, Appl. Phys. Lett. **88**, 052509 (2006).

[2] T. Kimura, Y. Otani, and J. Hamrle, Phys. Rev. B **73**, 132405 (2006).

[3] P. Łączkwoski, L. Vila, S. Ferry, A. Marty, J. M. George, H. Jaffrés, A. Fert, T. Kimura, T. Yang, Y. Otani, and J. P. Attané, Appl. Phys. Express **4**, 063007 (2011).

[4] G. Bridoux, M. V. Costache, J. Van de Vondel, I. Neumann, and S. O. Valenzuela, Appl. Phys. Lett. **99**, 102107 (2011).

[5] R. J. Pedersen and F. L. Vernon, Jr., Appl. Phys. Lett. **10**, 29 (1967).

[6] J. M. Pomeroy and H. Grube, J. Appl. Phys. **105**, 094503 (2009).

[7] S. Takahashi and S. Maekawa, Phys. Rev. B **67**, 052409 (2003).

[8] *Electron beam lithography on insulating substrates*, L. Arzubiaga (Master Thesis, Basque Country University, 2010).

[9] *Nanotechnology Measurement Handbook, A guide to electrical measurements for nanoscience applications* (Keithley, First Edition, 2006).

Chapter 4

Reproducibility of the LSV devices

Despite the large number of reports employing LSVs, the dispersion in the obtained data is fairly high in literature. As an example, Table 4.1 shows values of the spin-diffusion length of Cu, λ_{Cu}, and the spin polarizations of Py and Co, α_{Py} and α_{Co}, obtained from several references using Py/Cu and Co/Cu LSVs with transparent interfaces. The main reason for such dispersion lies in the irreproducibility of the fabrication of the devices [1–4] due to uncontrollable factors relevant at the nanoscale, which can lead to different results. For instance, a small variation in the interface quality can induce a large change in the effective values of α_{Py} and α_{Co}, deduced from the 1D spin-diffusion model [5,6]. Since the spin-flip scattering in metals is governed by the Elliott-Yafet mechanism [7,8], λ_{Cu} should change linearly with the inverse of the Cu channel resistivity $1/\rho_{Cu}$ [9]. However, the dispersion in λ_{Cu} is too large to be solely explained by the difference in ρ_{Cu} (see Table 4.1). Magnetic impurities at the NM channel, which strongly decrease the spin-diffusion length of a NM material, are the most likely reason for such dispersion [1, 10].

4.1 How to obtain λ_N and α_F

The values of α_F and λ_{Cu} shown in Table 4.1 for Co/Cu and Py/Cu LSVs with transparent interfaces, are obtained from the fitting of ΔR_{NL} as a function of the distance L to Eqs. 2.10 or 2.11 (see Fig. 4.2). Both equations describe the spin signal ΔR_{NL} measured in LSVs with transparent interfaces, the difference is that Eq. 2.11 is only valid when both FM electrodes are made of the same material and have equal dimensions, whereas Eq. 2.10 is the general case (for FM electrodes which can be different to each other).

The fitting of the above mentioned equations is a key parameter throughout this thesis and, thus, it is explained in detail in this section. We use Eq. 2.11 here due to its simpler form, which states:

$$\Delta R_{NL} = \frac{4\alpha_F^2 R_N}{\left[2 + \frac{R_N\left(1-\alpha_F^2\right)}{R_F}\right]^2 e^{L/\lambda_N} - \left[\frac{R_N\left(1-\alpha_F^2\right)}{R_F}\right]^2 e^{-L/\lambda_N}} \, .$$

It is worth reminding that the spin resistances of the NM, $R_N = \rho_N \lambda_N / w_N t_N$, and of the FM electrodes, $R_F = \rho_F \lambda_F / w_F w_N$, depend on the dimensions of the FM electrodes and NM channel (w_F, w_N, t_N), the resistivities of the FM and NM metals (ρ_F and ρ_N) and the spin-diffusion lengths of the FM and NM metals (λ_F and λ_N). There are several parameters that can be experimentally varied in this equation, but the most convenient one is the edge-to-edge distance between the FM electrodes, L. As seen from Eq. 2.11, its double exponential dependence facilitates the fitting. In addition, as explained in section 3.1, it is easy to control experimentally, by designing a device consisting of several LSVs with different Ls connected by the same NM channel (Fig. 3.1).

Table 4.1: Resistivity and spin-diffusion length of Cu and spin polarizations of Py and Co extracted from several references using Py/Cu and Co/Cu LSVs with transparent interfaces.

T (K)	ρ_{Cu} ($\mu\Omega$cm)	λ_{Cu} (nm)	α_{Py}	α_{Co}	References
4.2		100-400	0.15-0.4		[1]
10	1.36	200		0.074	[11]
4.2		190-260		0.1	[12]
4.2	1.67	395	0.29		[13]
4.2	4	400	0.33		[14]
4.2	1.5	460	0.21		[10]
10	0.69	1000	0.58		[15]
4.2	2.8	1000	0.2		[16]
80	1.2	1300	0.35		[17]
77	1.14	1500	0.25		[18]
10	1.26	1020	0.40		This thesis
10	1.8	905		0.114	This thesis

In order to perform the fitting, the dimensions of the device (including L) are measured by SEM for each device, and the deposited NM metal thickness, t_N, is controlled by the quartz crystal monitor of the evaporation systems and checked afterwards by X-ray reflectivity on a thin film deposited together with each sample. ρ_N, as a function of temperature, is obtained by measuring the four-point resistance of the NM channel for every L and performing a linear regression for each sample, whereas ρ_F is obtained separately in a different device where the FM material is deposited under the same nominal conditions as the FM electrodes of the LSVs. The value of λ_F is taken from literature. Due to the wide range of distances L that we use, the two values obtained from the fitting (α_F and λ_N) are completely uncoupled.

Even though Eq. 2.11 is used in this section because of its simplicity, for the fittings of our ΔR_{NL} *vs* L measurements we use Eq. 2.10, since the FM injector and detector of our LSVs have different widths in order to obtain different switching fields (section 3.1).

In addition, it is worth to note that in the case of tunneling or intermediate regimes the procedure is the same, and the ΔR_{NL} *vs* L measurements are fitted to Eqs. 2.13 or 2.7 in order to obtain P_I, α_F and λ_N.

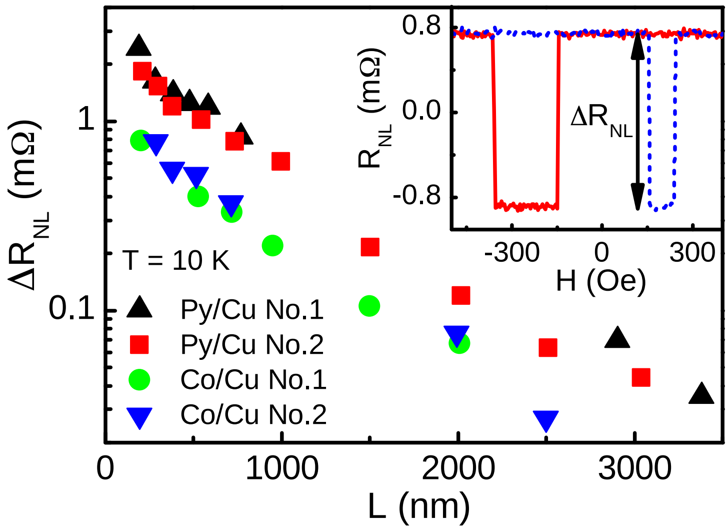

Figure 4.1: Spin signal as a function of the distance L between FM electrodes measured at 10 K for four different samples with a Cu channel and Py or Co electrodes. All the devices have identical dimensions. Inset: Non-local resistance measured at 10 K for a Py/Cu LSV with $L = 300$ nm. The solid red (dashed blue) line indicates the decreasing (increasing) direction of the magnetic field. The spin signal is tagged as ΔR_{NL}.

4.2 Reproducibility

In the introduction of this Chapter, magnetic impurities are mentioned as a possible source for the dispersion found in literature. This is avoided throughout this thesis by using two consecutive eBL processes (explained in section 3.1) as opposed to the two-angle shadow evaporation technique [1, 2, 10–15, 19], thus, avoiding cross contamination between FM and NM [10]. The interface quality is controlled by optimizing a protocol to obtain the interface with the same good quality (section 3.1). As an example, Fig. 4.1 displays the measured ΔR_{NL} as a function of L at 10 K. ΔR_{NL} was obtained by sweeping the external magnetic field H parallel to the FM electrodes (see Fig. 2.3 and inset of Fig. 4.1). This was done for four different Cu-based samples, two with Py electrodes ($\rho_{Py} = 22.4$ $\mu\Omega$cm and $\lambda_{Py} = 5$ nm [20] at 10 K) and two with Co electrodes ($\rho_{Co} = 11.5$ $\mu\Omega$cm and $\lambda_{Co} = 36$ nm [20] at 10 K). Both Py and Co electrodes have the same dimensions of $w_F \sim 110$ and ~ 150 nm. Since the value of λ_{Cu} is influenced by the grain boundary scattering (as shown in Chapter 6), the Cu channel dimensions are kept constant (with $w_N \sim 170-200$ nm and $t_N \sim 100$ nm). The results match perfectly for the two pairs of samples with the same FM/NM combination. In addition, since ΔR_{NL} decays nearly exponentially with L (see Eq. 2.10), the slope in the semilogarithmic plot is essentially λ_{Cu}, remaining the same for all four samples. Furthermore, the clear shift in ΔR_{NL} for samples with different FM materials is caused by their different spin-injection efficiency [19]:

$$\gamma = \left(\frac{2\alpha_F\lambda_F\rho_F}{1-\alpha_F^2}\right)^2, \tag{4.1}$$

which is directly related to the intrinsic properties of the FM metal and is an important contribution to Eqs. 2.10 and 2.11. The consistent results shown in Fig. 4.1, which have been reproduced for virtually all samples we have fabricated during this thesis (more than 25), allow us to compare properties between different samples, a long-standing problem in this type of devices [1–4].

Figure 4.2 shows the fitting to Eq. 2.10 for two of the samples shown in Fig. 4.1. The obtained values are $\lambda_{Cu} = 1020 \pm 46$ nm and $\alpha_{Py} = 0.40 \pm 0.01$ for the Py/Cu sample and $\lambda_{Cu} = 905 \pm 50$ nm, $\alpha_{Co} = 0.114 \pm 0.002$ for the Co/Cu sample. The errors are the ones from the fittings. It is important to mention that every sample we made with this characteristics led to very similar results and that the obtained values are among the highest reported in literature, as observed in table 4.1.

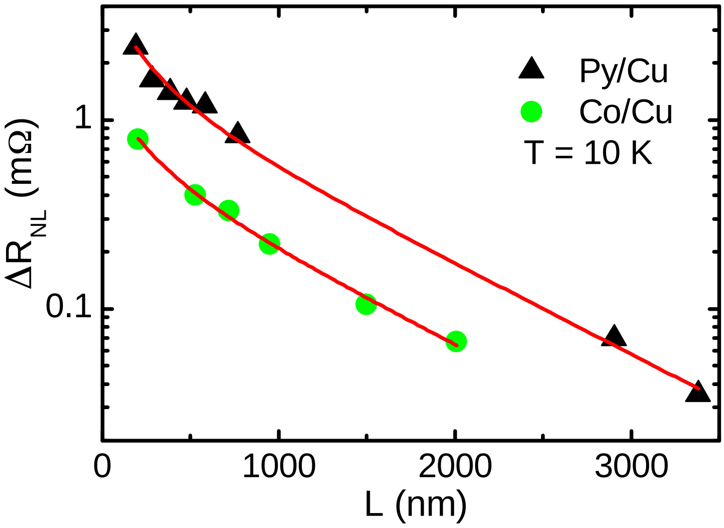

Figure 4.2: Spin signal as a function of the distance L between FM electrodes measured at 10 K for a sample containing Py/Cu (black triangles) and Co/Cu (green circles) LSVs with $t_{Cu} = 100$ nm. Red lines are fits of the data to Eq. 2.10.

4.3 Conclusions

We have shown that, as a result of an optimized nanofabrication method based on two consecutive eBL processes, we are able to fabricate highly reproducible LSVs with transparent interfaces, *i.e.*, the obtained spin signals for a given material, dimensions and interface treatment are always the same, yielding consistent values of α_F and λ_{Cu}. These values can, thus, be considered as a reference in LSV experiments, and allow us to compare properties between different samples, a long standing problem in this type of devices. This is essential for the results presented in Chapters 5 and 6, where several samples are systematically compared.

References

[1] M. Erekhinsky, A. Sharoni, F. Casanova, and I. K. Schuller, Appl. Phys. Lett. **96**, 022513 (2010).

[2] G. Mihajlović, J. E. Pearson, S. D. Bader, and A. Hoffmann, Phys. Rev. Lett. **104**, 237202 (2010).

[3] P. Łączkwoski, L. Vila, S. Ferry, A. Marty, J. M. George, H. Jaffrés, A. Fert, T. Kimura, T. Yang, Y. Otani, and J. P. Attané, Appl. Phys. Express **4**, 063007 (2011).

[4] H. Zou, X. J. Wang, and Y. Ji, J. Vac. Sci. Technol. B **28**, 1314 (2010).

[5] T. Valet and A. Fert, Phys. Rev. B **48**, 7099 (1993).

[6] S. Takahashi and S. Maekawa, Phys. Rev. B **67**, 052409 (2003).

[7] R. J. Elliott, Phys. Rev., **96**, 266 (1954).

[8] Y. Yafet, in *Solid State Physics*, edited by F. Seitz and D. Turnbull (Academic, New York, 1963), pp. 1-98.

[9] J. Bass and W. P. Pratt, J. Phys.: Condens. Matter **19**, 183201 (2007).

[10] H. Zou and Y. Ji, Appl. Phys. Lett. **101**, 082401 (2012).

[11] Y. Ji, A. Hoffmann, J. E. Pearson, and S. D. Bader, Appl. Phys. Lett. **88**, 052509 (2006).

[12] X. J. Wang, H. Zou, L. E. Ocola, R. Divan, and Y. Ji, J. Appl. Phys. **105**, 093907 (2009).

[13] F. Casanova, A. Sharoni, M. Erekhinsky, and I. K. Schuller, Phys. Rev. B **79**, 184415 (2009).

[14] M. Erekhinsky, F. Casanova, I. K. Schuler, and A. Sharoni, Appl. Phys. Lett. **100**, 212401 (2012).

[15] T. Kimura, T. Sato, and Y. Otani, Phys. Rev. Lett. **100**, 066602 (2008).

[16] F. J. Jedema, M. S. Nijboer, A. T. Filip, and B. J. van Wees, Phys. Rev. B **67**, 085319 (2003).

[17] T. Kimura, N. Hashimoto, S. Yamada, M. Miyao, and K. Hamaya, NPG Asia Mater. **4**, e9 (2012).

[18] T. Kimura, Y. Otani, and J. Hamrle, Phys. Rev. B **73**, 132405 (2006).

[19] G. Bridoux, M. V. Costache, J. Van de Vondel, I. Neumann, and S. O. Valenzuela, Appl. Phys. Lett. **99**, 102107 (2011).

[20] S. Dubois, L. Piraux, J. M. George, K. Ounadjela, J. L. Duvail, and A. Fert, Phys. Rev. B **60**, 477 (1999).

Chapter 5

Spin polarization of ferromagnets

We already explained that the creation of pure spin currents is crucial in the development of spintronics, both from an application point of view, as well as to study the basics physics behind the spin-injection and transport mechanisms. Hence, identifying materials with a high spin-injection efficiency is crucial. Only because we can fabricate devices that avoid contamination into the NM channel and reproduce the interface conditions (as explicitly described in Chapter 4), we can understand the precise role of the ferromagnetic materials in the electrical spin injection, which is of great interest for spintronics but not abundant in the literature.

In this Chapter, we extract the temperature dependence of the spin polarization of a FM material, α_F, for the first time from a LSV experiment. In particular, α_{Py} and α_{Co} as a function of temperature are compared. We show that the definition of α_F in the spin-diffusion model used in LSVs follows the standard two-channel model first studied by Mott [1, 2] by simultaneously analyzing the spin polarization and the conductivity of Py, which allows us to correct a systematic underestimation of α_{Py} derived from the LSV experiments.

With that purpose, two samples with identical characteristics were fabricated, where $\sim$ 70 nm of Cu were deposited as the NM channel ($\sim$ 170 nm wide) and the FM electrodes (35 nm thick and $\sim$ 110 and $\sim$ 150 nm wide) were made of Py in one case and of Co in the other. The electrical resisitivity of Cu was found to be $\rho_{Cu} = 1.6$ $\mu\Omega$cm at 10 K (3.2 $\mu\Omega$cm at 300 K), whereas the electrical resistivity of Co and Py, obtained as a function of temperature in two different devices, were $\rho_{Co} = 11.5$ $\mu\Omega$cm (19.1 $\mu\Omega$cm) and $\rho_{Py} = 22.4$ $\mu\Omega$cm (32.9 $\mu\Omega$cm) at 10 K (300 K). Figure 5.1 shows the measured resistivity of both FM metals as a function of temperature. Due to the optimized interface treatment (section 3.1.2), high quality transparent interfaces were obtained. As explained in section 4.1, the spin signal ΔR_{NL} was extracted by measuring the non-local resistance as a function of the applied magnetic field H for different temperatures between 10 K and 300 K. From the fitting of the ΔR_{NL} as a function of the distance between FM electrodes, L, to Eq. 2.10, the values of α_F and λ_{Cu} were obtained for different temperatures. The results for α_F are studied below, whereas those for λ_{Cu} are discussed in Chapter 6.

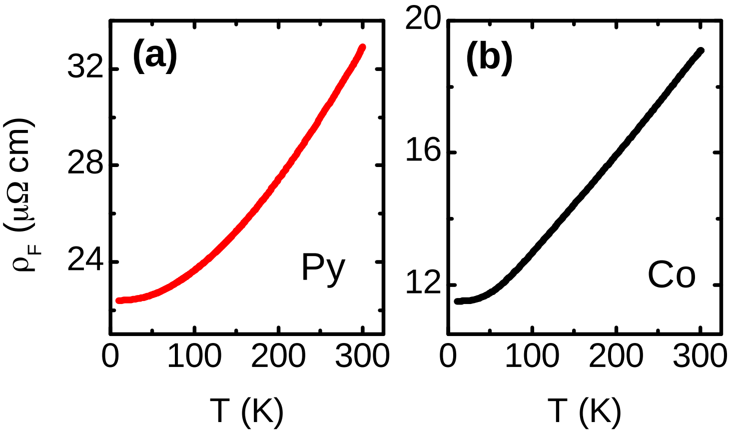

Figure 5.1: Resistivity as a function of temperature for (a) Py and (b) Co.

5.1 Spin-injection properties of Py and Co

The values and temperature dependence of α_{Py} and α_{Co} are shown in Fig. 5.2. The values at 10 K are $\alpha_{Py} = 0.38 \pm 0.01$ and $\alpha_{Co} = 0.118 \pm 0.001$. The obtained α_{Py} is among the highest values reported in LSV experiments (see Table 4.1) but is usually lower (down to half) than the values obtained by other methods (0.47–0.75) [3–6]. α_{Co} is also on the same order as the highest reported values in LSV experiments with transparent interfaces (see Table 4.1) and, in this case, much lower (three to five times) than the values obtained by other methods (0.36–0.52) [5, 7, 8]. A possible explanation for the dramatic difference in Co is the uncertainty of the value of λ_{Co}, a parameter used in the fitting to Eq. 2.10. Co has been reported to have $\lambda_{Co} \sim 40 - 60$ nm [7–9], a value questioned for being much longer than those of the rest of the FM materials [10]. Since the values of α_F and λ_F are coupled in Eq. 2.10 (Ref. [18]) and it is not possible to obtain them independently, an overestimation of λ_{Co} would lower the fitted value of α_{Co}. The quality of the Co/Cu interface could be another reason for the low α_{Co}. Due to the natural oxidation of Co, a spin-independent interface resistance might be created between the two metals, which would act as an additional spin-flip scatterer [18]. Since this additional contribution is not taken into account in Eq. 2.10, it would reduce the fitted value of α_{Co}.

At this point, it should be mentioned that, even if the obtained α_{Co} is three times smaller than α_{Py}, the product $\alpha_F \lambda_F$ is twice as large for Co than for Py. The only other contribution to the spin-injection efficiency γ (Eq. 4.1) is the electrical resistivity of the FM metal (see section 4.2). Since ρ_F is lower for Co, the backflow of the spin current is higher [12, 13], making the spin injection less effective, as observed in the shift in ΔR_{NL} in Fig 4.1.

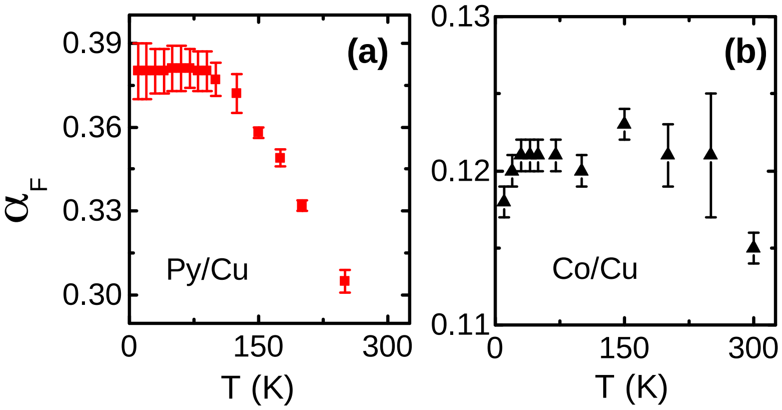

Figure 5.2: Spin polarization as a function of temperature for (a) Py and (b) Co. The error bars correspond to the error from the fitting to Eq. 2.10.

5.2 Temperature dependence of the spin polarization of Co and Py

As observed from Fig. 5.2, in the case of Co, the decay in α_{Co} is negligible up to 300 K (Fig. 5.2(b)), which is expected from previous experiments [7]. In the case of Py, a clear decay in α_{Py} is observed with temperature (Fig. 5.2(a)). In order to analyze the temperature dependence of α_{Py}, we will first note that $\alpha_{Py}(T)$ is an independent measurement fully decoupled from the temperature dependence of $\lambda_F(T)$, even if α_F and λ_F are coupled in Eq. 2.10. The temperature dependence of λ_F is directly obtained from the FM resistivity in the form $\lambda_F = const/\rho_F$ [3,7]. Even if in FM metals electron-magnon scattering is present above 100 K, it is not an efficient spin-lattice relaxation mechanism [7,14] and the spin relaxation is governed by the spin-orbit scattering on defects, impurities and phonons, just as the Elliott-Yafet mechanism in NM metals [15,16]. The previous scaling relation is valid for all temperature ranges: at 300 K we estimate $\lambda_{Py} = 3.4$ nm, which is in good agreement with the values reported in previous works [7,17].

It is also worth noting that the magnitude obtained from LSV experiments with transparent contacts corresponds to the current spin polarization described in Eq. 1.3 [18],

$$\alpha_F = \frac{\sigma_\uparrow - \sigma_\downarrow}{\sigma_\uparrow + \sigma_\downarrow} ,$$

where $\sigma_\uparrow$ and $\sigma_\downarrow$ are the spin-dependent conductivities introduced in Mott's two-channel model [1] and further developed by Campbell and Fert [2] in the study of electronic transport in pure ferromagnetic materials as well as in ferromagnetic alloys. However, the temperature dependence of the current spin polarization of FM metals has only recently been reported and analyzed [6], and to our knowledge, values obtained using LSV experiments have not been reported as a function of temperature before. The spin-dependent conductivities can be written as

$$\sigma_\uparrow = \frac{\rho_\downarrow + 2\rho_{\uparrow\downarrow}}{\rho_\uparrow\rho_\downarrow + \rho_{\uparrow\downarrow}(\rho_\uparrow + \rho_\downarrow)} , \sigma_\downarrow = \frac{\rho_\uparrow + 2\rho_{\uparrow\downarrow}}{\rho_\uparrow\rho_\downarrow + \rho_{\uparrow\downarrow}(\rho_\uparrow + \rho_\downarrow)} , \tag{5.1}$$

where $\rho_\uparrow$ and $\rho_\downarrow$ are the resistivities for spin-up and spin-down channels and $\rho_{\uparrow\downarrow}$ is the spin-mixing resistivity, which is a measure of the momentum transfer between the two channels by spin-mixing scatterings (basically caused by electron-magnon scattering) [2, 14]. The total conductivity through a FM material, thus, has the form

$$\sigma_F = \sigma_\uparrow + \sigma_\downarrow = \frac{\rho_\uparrow + \rho_\downarrow + 4\rho_{\uparrow\downarrow}}{\rho_\uparrow\rho_\downarrow + \rho_{\uparrow\downarrow}(\rho_\uparrow + \rho_\downarrow)} \ , \tag{5.2}$$

and α_F can be represented as a function of each spin-dependent resistivity,

$$\alpha_F = \frac{\rho_\downarrow - \rho_\uparrow}{\rho_\uparrow + \rho_\downarrow + 4\rho_{\uparrow\downarrow}} \ . \tag{5.3}$$

The temperature dependence of all three spin-dependent resistivities is modeled by considering that $\rho_i = \rho_{0i} + A_i T^2$ ($i =\uparrow,\downarrow$ and $\uparrow\downarrow$), where the term ρ_{0i} accounts for spin-flip scattering due to impurities [2] and the temperature dependence comes from phonon and magnon scatterings [6]. In order to explain the experimental temperature decay of α_{Py} with Eq. 5.3, coefficients ρ_{0i} and A_i must be obtained. For this purpose, some assumptions need to be made. First, assuming that the spin-mixing resistivity and, thus, $\rho_{0\uparrow\downarrow}$ is zero at low temperatures [6, 14], $\rho_{0\uparrow}$ and $\rho_{0\downarrow}$ can be obtained from the low-temperature values of $\sigma_\uparrow$ and $\sigma_\downarrow$, which, in the case of Py, are calculated from the experimental values of α_{Py} and σ_{Py} using Eqs. 1.3 and 5.2:

$$\sigma_\downarrow = \frac{\sigma_F(1-\alpha_F)}{2} \ ; \ \sigma_\uparrow = \frac{\sigma_F(1+\alpha_F)}{2} \ . \tag{5.4}$$

We obtain $\rho_{0\uparrow} = 3.24 \times 10^{-7}$ Ωm and $\rho_{0\downarrow} = 7.13 \times 10^{-7}$ Ωm. The corresponding ratio $\rho_{0\downarrow}/\rho_{0\uparrow} = 2.2$ is lower than the values between 6 and 20 previously reported [2, 6]. Next, A_i coefficients have been fixed as $A_\uparrow = A_\downarrow = A_{\uparrow\downarrow}$, following Ref. [6]. In order to obtain their value, the conductivity of Py as a function of temperature, plotted in Fig. 5.3(a), has been fitted to Eq. 5.2 (red solid line) with the only fitting parameter $A_i = (1.96 \pm 0.01) \times 10^{-12}$ $\mathrm{m^{-1}K^2}$. According to the model above, we should be able to reproduce the temperature dependence of α_{Py} by introducing this parameter into Eq. 5.3. However, the obtained curve (red solid line in Fig. 5.3(b)) does not reproduce well the experimental temperature dependence. Alternatively, we have fitted the experimental values of α_{Py} directly to Eq. 5.3 (blue dashed line in Fig 5.3(b)), obtaining, in this case, $A_i = (0.60 \pm 0.02) \times 10^{-12}$ $\Omega^{-1}\mathrm{m^{-1}K^2}$. In turn, this A_i value cannot reproduce the experimental values of σ_{Py} (blue dashed line in Fig 5.3(a)).

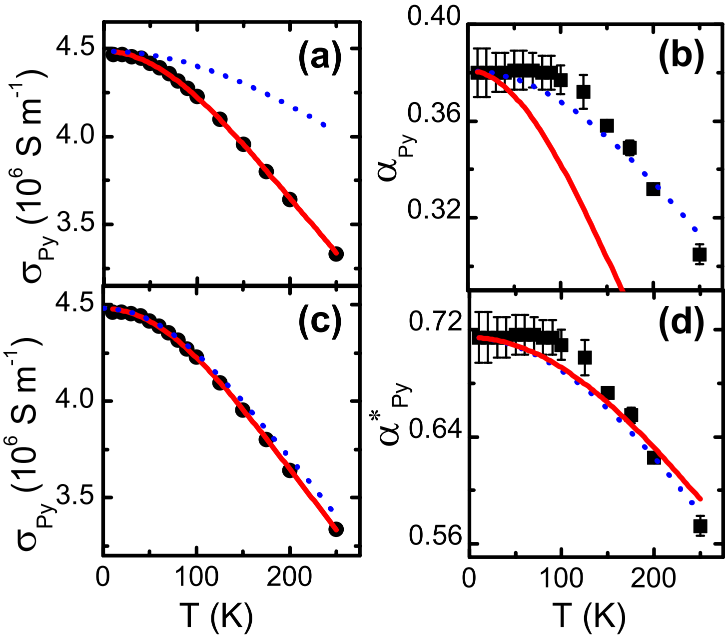

Figure 5.3: (a) Conductivity of Py as a function of temperature (black circles). The red solid line is a direct fit of the data to Eq. 5.2, and the blue dashed line is the representation of Eq. 5.2 with the A_i parameter obtained from the fitting of the data in (b) to Eq. 5.3. (b) Spin polarization of Py as a function of temperature (black squares). The blue dashed line is a direct fit of the data to Eq. 5.3, and the red solid line is the representation of Eq. 5.3 with the A_i parameter obtained from the fitting of the data in (a) to Eq. 5.2. (c) Conductivity of Py as a function of temperature (black circles). The red solid line is a direct fit of the data to Eq. 5.2, and the blue dashed line is the representation of Eq. 5.2 with the A_i parameter obtained from the fitting of the data in (d) to Eq. 5.3 and the new $\rho_{0\uparrow}$ and $\rho_{0\downarrow}$ obtained after applying the correction of α_F. (d) Corrected spin polarization of Py as a function of temperature (black squares). The blue dashed line is a direct fit of the data to Eq. 5.3, and the red solid line is the representation of Eq. 5.3 with the A_i parameter obtained from the fitting of the data in (c) to Eq. 5.2 and the new $\rho_{0\uparrow}$ and $\rho_{0\downarrow}$ obtained after applying the correction of α_F.

The mismatch between the red solid and the blue dashed lines in both Figs. 5.3(a) and 5.3(b) evidences that the model assumed cannot simultaneously describe our two sets of independent data (α_{Py} and σ_{Py}). Considering the validity of the model to explain the temperature dependence of the current spin polarization in a previous study [6], it is more plausible to suppose that the origin of the disagreement comes from the data sets. In particular, the obtained low values of α_{Py} in the LSV experiments compared to other experiments (*i.e.*, giant magnetoresistance [3,4] or spin-wave Doppler [6]), suggest an underestimation of our α_{Py} data, which can be corrected by introducing a multiplying factor to the experimental α_{Py} values. By introducing the factor $n = \alpha_F^*/\alpha_F$ and the relation $\frac{\rho_{0\uparrow}}{\rho_{0\downarrow}} = \frac{1+n\alpha_F}{1-n\alpha_F}$ into Eqs. 5.2 and 5.3, a factor of $n = 1.88$ is found to give the best agreement between our two data sets (α_{Py} and σ_{Py}) and the model above as well as a much closer match between our α_{Py} value and the ones obtained by other methods [3,4,6]. With such a correction, we obtain $\rho_{0\uparrow} = 2.61 \times 10^{-7}$ Ωm and $\rho_{0\downarrow} = 15.66 \times 10^{-7}$ Ωm; the ratio $\rho_{0\uparrow}/\rho_{0\downarrow}$ has a value of 6, now within the range reported in Refs. [2] and [6]. From the fitting of σ_{Py} to Eq. 5.2 (red solid curve in Fig. 5.3(c)) $A_i = (1.09 \pm 0.01) \times 10^{-12}$ $\Omega^{-1}\text{m}^{-1}\text{K}^2$ is obtained, which, being introduced into Eq. 5.3, perfectly reproduces the experimental curve of α^*_{Py} (red solid curve in Fig. 5.3(d)). Similarly to what we have performed for α_{Py}, we have fitted the values of α^*_{Py} directly to Eq. 5.3 (blue dashed line in Fig. 5.3(d)), obtaining $A_i = (0.99 \pm 0.02) \times 10^{-12}$ $\Omega^{-1}\text{m}^{-1}\text{K}^2$. This value of A_i is now in excellent agreement with the previous one and reproduces, with high accuracy, the experimental values of σ_{Py} (blue dashed line in Fig. 5.3(c)).

There are several possible reasons, which are not mutually exclusive, for the underestimation of the obtained α_{Py}. The first one could be the choice of a wrong injection area in the expression of R_F present in Eq. 2.10. If we consider that the side surfaces of the FM electrodes are also in contact with the Cu channel, the correct expression would be $R_F = 2\lambda_F\rho_F/(1-\alpha_F^2)(w_F w_N + 2t_F w_F)$. By introducing such a correction into Eq. 2.10, α_{Py} increases from 0.38 to 0.49 at 10 K. Another possible reason for such underestimation could be the 1D approximation of the spin-diffusion model used in LSVs to derive Eq. 2.10 [19]. Indeed, it has already been reported [20] that such an approximation does not consider the "intermediate" region of the NM metal above the FM/NM interface, which causes spins to flip before they diffuse through the NM channel and even to flow back to the FM electrodes underestimating the fitted α_F value. Similarly, Niimi et al. [21] have recently analyzed LSV data using a three-dimensional (3D) finite element model based on an extension of the Valet-Fert formalism where they observe an increase in the fitted α_{Py} from 1D to 3D. In addition to this, it is also possible that the value of λ_{Py} used for the fitting of Eq. 2.10 is not accurate enough. The value of $\lambda_{Py} = 5$ nm, obtained from GMR experiments [3], could easily be different from the real λ_{Py} of our Py, due to a dispersion in related properties such as resistivity. Because of the $\alpha_F\lambda_F$ coupling, an overestimation of λ_{Py} would directly lower the obtained α_{Py} value.

5.3 Conclusions

To summarize, the electrical spin injection from both Py and Co was compared, clearly observing a decreased spin injection with the latter one, caused by its lower electrical resistivity. The experimental spin polarizations of both FM materials are among the highest reported in LSV experiments, even though they are systematically lower than those obtained by other methods, and their temperature dependences were reported. For the case of Py, the comparison of the temperature dependence of the spin polarization with the conductivity agrees well with the prediction given by the standard two-channel model, but a correction factor of ~ 2 to the spin polarization was detected. Our analysis, thus, confirms the substantial underestimation of the spin polarization in LSV experiments and identifies several possible contributions to this mismatch.

References

[1] N. H. Mott, Proc. R. Soc. London, Ser. A **153**, 699 (1936).

[2] *Ferromagnetic Materials*, I. A. Campbell and A. Fert (North-Holland, Amsterdam, 1982), Vol. 3, Chap. 9.

[3] S. Dubois, L. Piraux, J. M. George, K. Ounadjela, J. L. Duvail, and A. Fert, Phys. Rev. B **60**, 477 (1999).

[4] S. D. Steenwyk, S. Y. Hsu, R. Loloee, J. Bass, and W. P. Pratt, Jr., J. Magn. Magn. Mater. **170**, L1 (1997).

[5] B. Nadgorny, R. J. Soulen, M. S. Osofsky, I. I. Mazin, G. Laprade, R. J. M. van de Veerdonk, A. A. Smits, S. F. Cheng, E. F. Skelton, and S. B. Qadri, Phys. Rev. B **61**, R3788 (2000).

[6] M. Zhu, C. L. Dennis, and R. D. McMichael, Phys. Rev. B **81**, 140407(R) (2010).

[7] L. Piraux, S. Dubois, A. Fert, and L. Belliard, Eur. Phys. J. B **4**,413 (1998).

[8] B. Doudin, A. Blondel, and J. P. Ansermet, J. Appl. Phys. **79**, 6090 (1996).

[9] A. C. Reilly, W.-C. Chiang, W. Park, S. Y. Hsu, R. Loloee, S. Steenwyk, W. P. Pratt, Jr., and J. Bass, IEEE Trans. Magn. **34**, 939 (1998).

[10] J. Bass and W. P. Pratt, J. Phys.: Condens. Matter **19**, 183201 (2007).

[11] P. Łączkwoski, L. Vila, S. Ferry, A. Marty, J. M. George, H. Jaffrés, A. Fert, T. Kimura, T. Yang, Y. Otani, and J. P. Attané, Appl. Phys. Express **4**, 063007 (2011).

[12] G. Bridoux, M. V. Costache, J. Van de Vondel, I. Neumann, and S. O. Valenzuela, Appl. Phys. Lett. **99**, 102107 (2011).

[13] S. Oki, S. Yamada, N. Hashimoto, M. Miyao, T. Kimura, and K. Hamaya, Appl. Phys. Express **5**, 063004 (2012).

[14] A. Fert, J.-L. Duvail, and T. Valet, Phys. Rev. B **52**, 6513 (1995).

[15] R. J. Elliott, Phys. Rev., **96**, 266 (1954).

[16] Y. Yafet, in *Solid State Physics*, edited by F. Seitz and D. Turnbull (Academic, New York, 1963), pp. 1-98.

[17] T. Kimura, T. Sato, and Y. Otani, Phys. Rev. Lett. **100**, 066602 (2008).

[18] F. J. Jedema, M. S. Nijboer, A. T. Filip, and B. J. van Wees, Phys. Rev. B **67**, 085319 (2003).

[19] S. Takahashi and S. Maekawa, Phys. Rev. B **67**, 052409 (2003).

[20] M. Erekhinsky, A. Sharoni, F. Casanova, and I. K. Schuller, Appl. Phys. Lett. **96**, 022513 (2010).

[21] Y. Niimi, Y. Kawanishi, D. H. Wei, C. Deralnot, H. X. Yang, M. Chshiev, T. Valet, A. Fert, and Y. Otani, Phys. Rev. Lett. **109**, 156602 (2012).

Chapter 6

Spin relaxation in copper

As mentioned in Chapter 1, the envisioned second generation of spintronic devices should be suitable for the spin transport over a significantly long distance, in order to enable the manipulation of the information carried by pure spin currents. Therefore, it is of utmost importance to understand the spin-relaxation processes leading to the loss of the spin information inside a NM material.

Whereas nanostructures are needed in order to be able to electrically generate and detect pure spin currents, the inherent confinement related to such nanostructures introduces additional sources of spin relaxation. In a NM material, spin relaxation arises both from the scattering with phonons and the defects of the material, which include impurities, grain boundaries, and the surface. In particular, the role of the surface to the spin-flip scattering has recently been debated due to its effect to the spin-diffusion length at low temperatures [1–5]. In this Chapter, we first analyze the charge and spin transport in copper (Cu) nanowires as a function of the temperature and thickness by using Py/Cu LSVs. We quantify the relative importance of each contribution to the spin relaxation through the corresponding spin-flip probabilities.

Furthermore, the role that different FM injectors and detectors play on the spin relaxation in a NM metal is studied, by systematically comparing the spin transport in Cu as a function of temperature using Py/Cu and Co/Cu LSVs. This study gives us information about additional sources of spin-flip scattering that affect the spin transport: magnetic impurities in the bulk of the Cu channel, which, in addition, are found to be the responsible of the low-temperature maximum in λ_N, observed by several groups [1, 2, 4–7].

The results presented here allows us to suggest routes for improving spin transport in metallic nanostructures, otherwise limited by impurities or confinement effects.

6.1 Contribution of defects to the charge and spin transport

Five samples were fabricated, with Cu thicknesses (t_{Cu}) of 145, 100, 70, 60, and 40 nm, and resistivities (ρ_{Cu}) of 1.18, 1.26, 1.63, 1.98, and 2.22 $\mu\Omega$cm at 10 K, respectively (see Table 6.1). The width of the Cu nanowire is $\sim$ 200 nm for all samples. The thickness of Py is 35 nm for all samples, the widths are $\sim$ 110 nm and $\sim$ 150 nm, and the resistivity is 22.4 $\mu\Omega$cm (32.9 $\mu\Omega$cm) at 10 K (300 K). The spin signal ΔR_{NL} as a function of the distance L was measured in every device (see Fig. 6.1), and the fitting to Eq. 2.10 was done in order to obtain the values of α_{Py} and λ_{Cu} (see section 4.1 for details). For all samples, we obtain the values of α_{Py}, which are consistently between 0.38 and 0.40 (0.31 and 0.34) at 10 K (300 K), in agreement with literature [1, 3–6, 8, 9] and our previous results (Chapters 4 and 5).

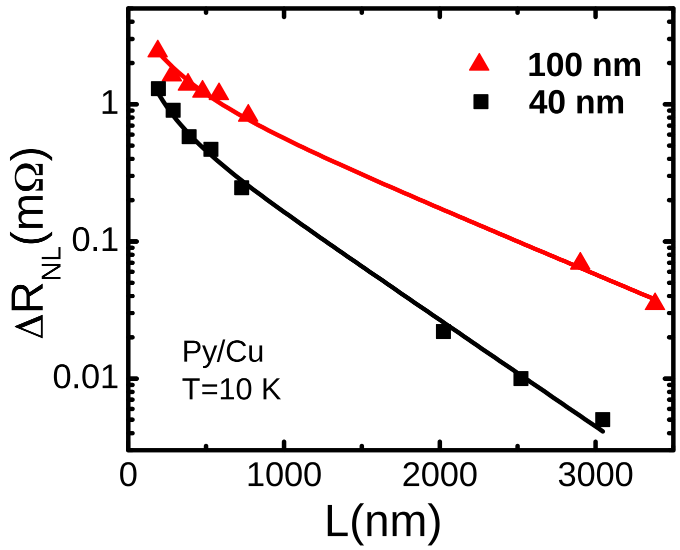

Figure 6.1: Spin signal as a function of the distance L between Py electrodes measured at 10 K for two samples with t_{Cu} = 100 nm (red triangles) and 40 nm (black squares). Solid lines are fits to Eq. 2.10.

Table 6.1: Summary of the most relevant data of the samples used in this section: thickness of the Cu channel, resistivity and spin-diffusion length at 10 K, defect scattering time, and spin-flip probabilities from phonon and defect scattering.

t_{Cu} (nm)	ρ_{Cu} ($\mu\Omega$cm)	λ_{Cu} (nm)	τ_e^{def} ($\times 10^{-3}$ ps)	a_{ph} ($\times 10^{-4}$)	a_{def} ($\times 10^{-4}$)
145	1.18 ± 0.01	1020 ± 6	35.8 ± 0.6	12.8 ± 0.8	8.2 ± 0.5
100	1.26 ± 0.01	1020 ± 46	33.5 ± 0.8	11.9 ± 0.9	7.0 ± 0.5
70	1.63 ± 0.01	863 ± 17	25.9 ± 0.8	11.2 ± 1.0	6.3 ± 0.6
60	1.98 ± 0.01	709 ± 120	21.3 ± 0.5	11.8 ± 0.5	6.8 ± 0.3
40	2.22 ± 0.01	501 ± 19	19.0 ± 0.2	9.5 ± 2.0	11.0 ± 0.3

6.1.1 Charge transport in Cu nanowires

For a proper analysis of λ_{Cu} values, we first need to characterize the resistivity of the Cu nanowire. It was measured as a function of temperature for each sample (only three curves are shown in Fig. 6.2 for the sake of clarity), showing all curves the same temperature dependence. The phonon scattering contribution to the resistivity is described by the Bloch-Grüneisen theory

$$\rho(T) = \rho_0 + K\left(\frac{T}{\Theta}\right)^5 \int_0^{\Theta/T} \frac{x^5}{(e^x-1)(1-e^{-x})}dx \ , \qquad (6.1)$$

where ρ_0 is the residual resistivity, K is a constant for a given metal and Θ is the Debye temperature [10, 11]. We obtain $\Theta \sim 280$ K and $K \sim 6.5$ $\mu\Omega$cm for all samples when fitting the experimental curves to Eq. 6.1, in agreement with previously reported values [11,12]. The residual resistivity, arising from scattering with defects, is thus temperature independent and increases with decreasing the Cu thickness as can be seen in Fig. 6.2. Both grain-boundary scattering and surface scattering are known to increase the resistivity with decreasing the thickness of thin films and nanowires. However, whereas the former contribution does not change the temperature dependence of the resistivity with respect to the bulk one, the latter induces a deviation in this temperature dependence [13–15]. This indicates that the defect scattering of the Cu nanowires is dominated by grain boundaries rather than surface.

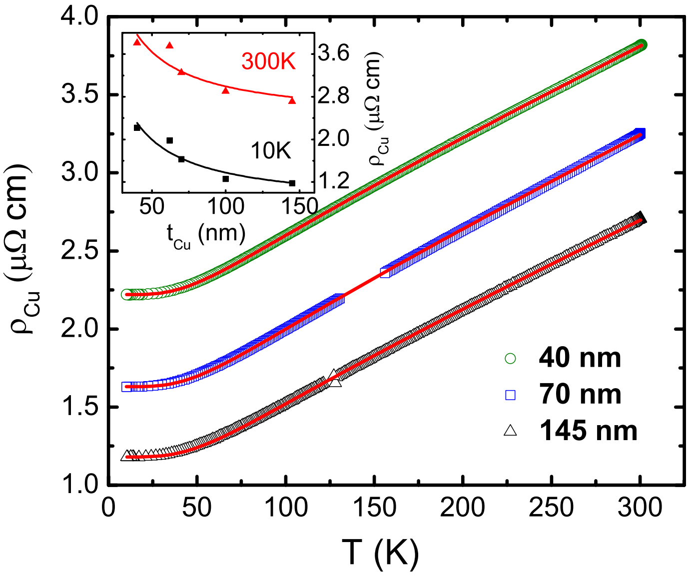

Figure 6.2: Resistivity as a function of temperature for Cu nanowires with different thicknesses. Red solid lines are fits to Eq. 6.1. Inset: Resistivity of the Cu channels as a function of the thickness at 10 K (black squares) and 300 K (red triangles). Solid lines are fits to Eq. 6.2.

The grain-boundary-dominated scattering is described by the Mayadas and Shatzkes model [13–17]. This model, to a first approximation, has a dependence with the inverse of the average grain size d by

$$\rho = \rho_b\left(1 + \frac{3l}{2}\frac{R}{1-R}\frac{1}{d}\right) \ , \qquad (6.2)$$

where ρ_b and l are the resistivity and the mean-free path of the bulk Cu, and R is the reflection coefficient of the electrons colliding at the grain boundaries. One can consider that, in evaporated Cu, d is given by the smallest dimension of the wire, *i.e.*, the thickness in this case [13], and fit the resistivity of Cu as a function of the thickness to the Mayadas and Shatzkes model, as it is shown in the inset of Fig. 6.2. This fitting is consistent both at 10 and 300 K, yielding a temperature-independent value of $R = 0.38$, which is in good agreement with literature [13,15,17]. From the fitting, we also obtain the value of $\rho_b = 0.73$ $\mu\Omega$cm (2.31 $\mu\Omega$cm) at 10 K (300 K), slightly larger than pure bulk Cu resistivity, due to the likely presence of other impurities [17].

6.1.2 Spin transport in Cu nanowires

Figure 6.3(a) shows the values of the spin-diffusion length of Cu, obtained from the fitting of Eq. 2.10, as a function of the temperature. The highest values of the spin-diffusion length correspond to the samples with the thickest Cu nanowire (145 nm). A λ_{Cu} of 1020 ± 6 nm is obtained at 10 K, being in good agreement with the largest values reported [1,8,18] and our previous results (see table 4.1). For the sample with a 40-nm-thick Cu nanowire, a λ_{Cu} of 500 ± 16 nm is obtained at 10 K. The values of λ_{Cu} tend to increase with thickness, following the opposite trend of the resistivity (see Table 6.1). This is also observed in Fig. 6.1, where the slope of the spin signal as a function of L is clearly reduced for the smallest t_{Cu}. In fact, λ_{Cu} shows, with a slight dispersion, a linear dependence with the inverse of the resistivity at 10 K [see Fig. 6.3(b)]. Figure 6.3(a) also shows a maximum in λ_{Cu} around 30 K for all thicknesses. This behavior, which can not be explained by the Elliott-Yafet mechanism for spin relaxation [19, 20], has been previously reported in Cu [1,5–7], in silver (Ag) [2,4] and in aluminum (Al) LSV devices [6,7] and is discussed in section 6.3.

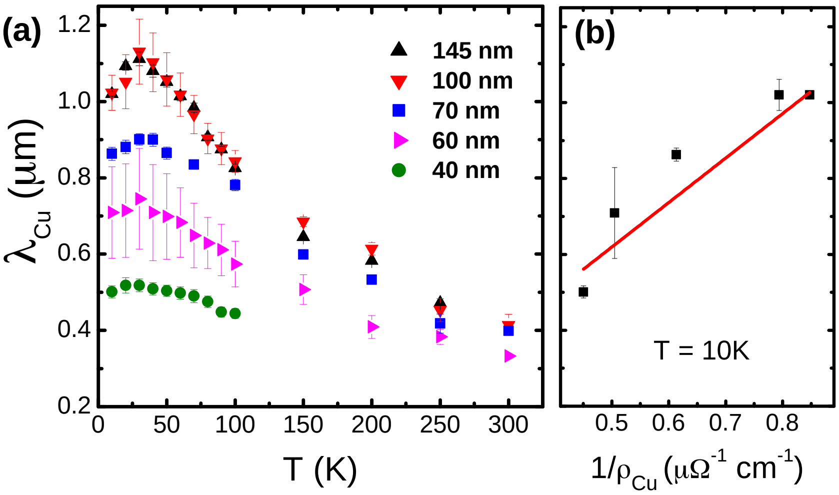

Figure 6.3: (a) Spin-diffusion length of Cu as a function of temperature obtained for nanowires with different thicknesses. (b) Spin-diffusion length of Cu as a function of the inverse of the resistivity, at 10 K. Red solid line is a linear fit of the data.

The spin-diffusion length is represented by $\sqrt{D\tau_{sf}}$, where $D = 1/N(E_F)e^2\rho$

is the diffusion constant, $N(E_F)$ is the electronic density of states at the Fermi level (1.8×10^{28} states/eV/m^3 for Cu [18]), e is the electronic charge, and τ_{sf} the spin-relaxation time of the NM metal. The spin-relaxation mechanisms in metals arise from the spin-orbit interaction, as discussed by Elliott and Yafet [19,20]. In this case, the spin-relaxation time is proportional to the momentum-relaxation time τ_e by the spin-flip probability a in the form $1/\tau_{sf} = a/\tau_e$ (see section 2.1.1).

The momentum-relaxation time can be calculated from the measured resistivity with

$$\tau_e = \frac{3}{v_F^2 N(E_F) e^2 \rho} , \tag{6.3}$$

where v_F is the Fermi velocity (1.57×10^6 m/s for Cu [18]), and decomposed in two different contributions coming from the phonons ph and the defects def (including impurities, grain boundaries, and surface) using the Matthiessen rule

$$\frac{1}{\tau_e} = \frac{1}{\tau_e^{ph}} + \frac{1}{\tau_e^{def}} . \tag{6.4}$$

As discussed previously in the analysis of the resistivity (section 6.1.2), the first contribution is temperature dependent, whereas the second one is temperature independent. Accordingly, the spin-relaxation rate $(\tau_{sf})^{-1}$ can be expressed as

$$\frac{1}{\tau_{sf}} = \frac{a_{ph}}{\tau_e^{ph}} + \frac{a_{def}}{\tau_e^{def}} , \tag{6.5}$$

where a_{ph} and a_{def} are the spin-flip probabilities for each contribution.

Figure 6.4 shows, for all samples, $(\tau_{sf})^{-1}$ as a function of the phonon-scattering rate $(\tau_e^{ph})^{-1}$, which has been calculated from the $\rho(T)$ measurements (Fig. 6.2), the Matthiessen rule, and taking into account that the residual resistivity gives the defect-scattering rate $(\tau_e^{def})^{-1}$ (listed in Table 6.1). The minimum in $(\tau_{sf})^{-1}$ associated to the maximum in λ_{Cu} (Fig. 6.3(a)) is smeared out in this representation, and a clear linear dependence of the experimental data is observed for all thicknesses, which can be fitted to Eq. 6.5. The value of a_{ph} is directly obtained from the slope. The intercept to the y axis corresponds to a_{def}/τ_e^{def} , which is the contribution of the defects to the total spin-relaxation rate $(\tau_{sf})^{-1}$. Since we already know the value of $(\tau_e^{def})^{-1}$, we can independently obtain a_{def}.

The values of the spin-flip probabilities a_{ph} and a_{def} for all samples are shown in Table 6.1. Cu nanowires with different thicknesses consistently yield the same value of a_{ph} ($\sim 1.1 \times 10^{-3}$), which is an intrinsic parameter of bulk Cu. Similar values have been previously obtained in bulk Cu using conduction-electron spin resonance (CESR) experiments ($a_{ph} = 1.1 \times 10^{-3}$) [21], as well as in Cu nanowires with LSV experiments ($a_{ph} = 2.0 \times 10^{-3}$) [18]. The value of a_{def} is very similar for all thicknesses as well, evidencing that the nature of the defects contributing to the spin relaxation is the same in all samples. This is consistent with the observed linear dependence of λ_{Cu} with the inverse of resistivity at 10 K (Fig. 6.3(b)). These defects are mostly grain boundaries, as demonstrated from the resistivity analysis, although the slight dispersion in the values of a_{def} also suggests small differences in the presence of impurities from sample to sample, arising from the

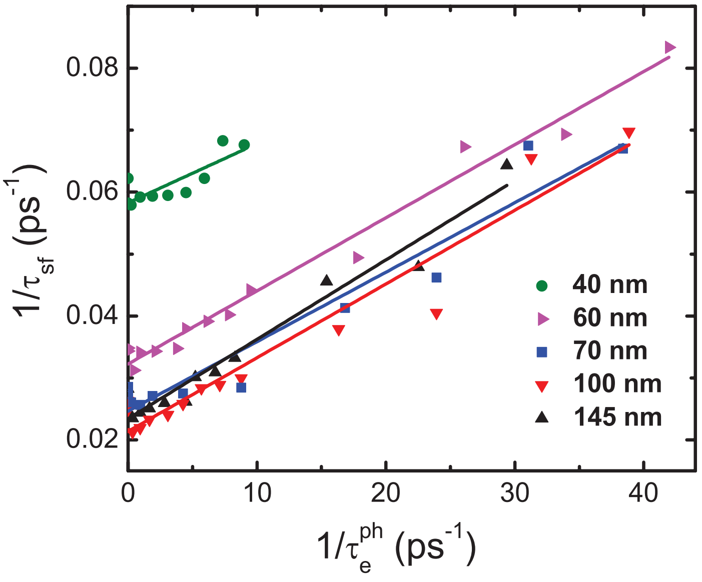

Figure 6.4: Spin-relaxation rate as a function of the phonon-scattering rate. Symbols are experimental data and solid lines are linear fits to Eq. 6.5.

fabrication process. The coherent fitting of Eq. 6.5 to all samples demonstrates that both spin-flip mechanisms are independent of the temperature [20] and of the thickness of Cu. The temperature dependence of the spin-relaxation rate is thus given by the phonon-scattering rate, whereas the temperature-independent part is given by the defect-scattering rate, which increases with decreasing thickness and contributes to the spin-relaxation rate at all temperatures. This is clearly observed in Fig. 6.4, where all the parallel linear curves are shifted up with decreasing Cu thickness.

6.2 Spin transport in Cu using different FM metals

Next, we study in more detail the role that Py and Co play in the spin transport of Cu. With this purpose, we obtain λ_{Cu} in two different samples with identical characteristics where ~ 70 nm of Cu were deposited as the NM channel and the FM electrodes were made of Py in one case and of Co in the other (these are the samples studied in Chapter 5). The values and the temperature dependence of λ_{Cu}, shown in Fig. 6.5(a), are the same for both samples containing Py and Co electrodes ($\lambda_{Cu} = 860 \pm 20$ and 820 ± 90 nm at 10 K for Co and Py, respectively). This is consistent with the fact that they show the same resistivity ρ_{Cu} at all temperatures ($\rho_{Cu} = 1.6$ $\mu\Omega$cm at 10 K, see the inset of Fig. 6.5(a)) since λ_{Cu} is basically proportional to $1/\rho_{Cu}$ (see Fig. 6.3(b)). This good agreement evidences that the use of different FM electrodes does not influence the spin transport properties of the NM channel. The obtained values of λ_{Cu} are among the highest reported in LSV experiments, given the dimensions and the ρ_{Cu} of the channel (see tables 4.1 and 6.1), further suggesting that the purity of the Cu channel is not affected by the fabrication process.

Despite the saturation of $1/\rho_{Cu}$ at low temperatures, a maximum is found in λ_{Cu} for both samples, equal to the maximum in λ_{Cu} found in section 6.1.2 for other samples. The maximum in λ_{Cu} arises from a maximum in R_{NL} as a function of temperature, which also occurs at 30 K in both Py/Cu and Co/Cu LSVs for any L as shown in Figs. 6.5(b) and 6.5(c).

6.3 The origin of the maximum in λ_{Cu}

Finally, we discuss the origin of the maximum in λ_{Cu}. From the previous discussion of the contributions to the spin relaxation in the framework of the Elliott-Yafet mechanism, the contribution of the phonons is the only responsible for the temperature dependence of the spin-relaxation rate and, therefore, of λ_{Cu}. Accordingly, from the temperature dependence of the resistivity, an increase of λ_{Cu} with decreasing temperature until saturation at low temperatures is expected. This is observed down to 30 K, where λ_{Cu} starts to decrease with decreasing temperature (see Figs. 6.3(a) and 6.5(a)). This effect can only be explained by introducing a temperature dependence of the contribution of the defects, which include grain boundaries, surface, and impurities.

Since we have already shown that the contribution of grain boundaries is temperature independent, we could hypothesize that the observed temperature dependence arises from the surface contribution [1, 2]. This has been explicitly taken into account by Mihajlović et al. [2], who added an extra term of the form a_S/τ_e^S to Eq. 6.5. The temperature dependence arises from the fact that the surface scattering time τ_e^S is proposed to be inversely proportional to the one coming from the bulk. As a result, surface contribution to spin-flip scattering should dominate at low temperatures, when the mean free path becomes comparable to the dimensions of the NM nanowire, and the temperature at which the maximum of λ_N occurs should increase when decreasing the thickness of the NM nanowire. However, our results clearly show that the maximum of λ_{Cu} always occurs at 30 K, regardless of the thickness of Cu (see Fig. 6.3(a)). Furthermore, the assumption that the surface scattering time is inversely proportional to the bulk one would necessarily imply an upturn in ρ_{Cu} at low temperatures, which is not observed (Fig. 6.2 and inset of Fig. 6.5(a)).

A second option is that the temperature dependence comes from the impurities' contribution. In particular, magnetic impurities have not been considered in our previous analysis since the Elliott-Yafet mechanism describes the spin-flip scattering in metals in the absence of such [18–20]. A temperature-dependent spin-flip probability coming from magnetic impurities is an option which is supported by recent studies made in Cu [5, 7], Al [7] and Ag [4] LSV devices. According to some of these works, the oxidation of the surface of the NM nanowire [5], or its capping with a MgO layer [4], induce the extinction of the maximum of the spin-diffusion length. Such disappearance is attributed to the isolation from the NM nanowire of the magnetic impurities, which are most likely located at the surface due to the two-angle-shadow-evaporation fabrication process [5]. In our case, the presence of magnetic impurities at the surface of the NM channel is unlikely due to the two-step fabrication process employed, and thus, they must be located at the bulk. Interdiffusion of the FM material near the interface could be a possible source of magnetic impurities at the NM channel. In this case, the effective spin

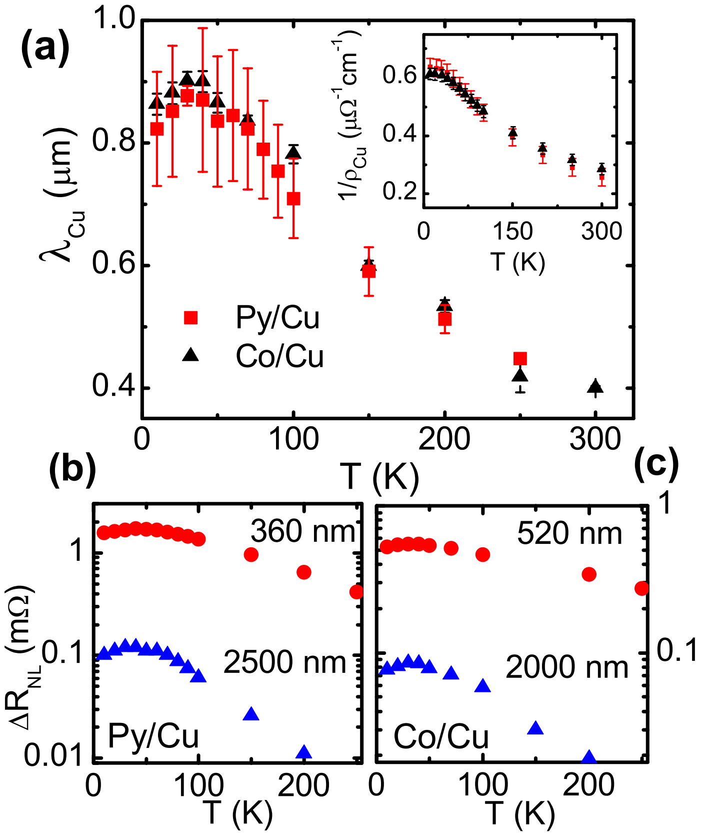

Figure 6.5: (a) Spin-diffusion length of Cu as a function of temperature using Py (red squares) and Co (black triangles) electrodes. Error bars correspond to the error from the fitting of Eq. 2.10. A maximum is found at 30 K. Inset: Inverse of the resistivity of Cu as a function of temperature using Py (red squares) and Co (black triangles) electrodes. Error bars correspond to the error from the linear regression used to obtain the resistivity. (b) Spin signal as a function of temperature in two Py/Cu LSVs with $L = 360$ nm (red dots) and $L = 2500$ nm (blue triangles). A maximum is observed at 30 K. (c) Spin signal as a function of temperature in two Co/Cu LSVs with $L = 520$ nm (red dots) and $L = 2000$ nm (blue triangles). A maximum is observed at 30 K.

injection should also be affected, leading to the observation of a clear maximum in the temperature dependence of the spin polarization [7]. However, this is not observed in our samples (see Fig. 5.2). In addition, changing the FM material should also change the position of the maximum in λ_{Cu} [7], but, in our case, the shape and position (30 K) of the maximum in λ_{Cu} are independent of the used FM material as shown in Fig. 6.5(a). These two observations rule out the presence of interdiffusion and confirm the previous evidence that, with our fabrication process, the NM channel is not contaminated in any way by the FM used in the electrodes. Therefore, the magnetic impurities at the bulk of the Cu channel, responsible for the maximum in λ_{Cu}, must be introduced during the evaporation process, probably from the original Cu source. This result is in agreement with recent observations in which the origin of the maximum in λ_{Cu} is attributed to a suppression of the spin diffusion at low temperatures generated by magnetic impurities *via* a manifestation of the Kondo effect [7]. The fact that we do not observe an upturn in ρ_{Cu} at low temperatures means that the concentration of magnetic impurities in our Cu nanowires is below the concentration needed for the (charge) Kondo effect to emerge [7], evidencing, as expected, that the spin transport is more sensitive to magnetic impurities than the charge transport.

6.4 Conclusions

In conclusion, we systematically measured both charge and spin transport in Cu nanowires as a function of temperature and thickness using lateral spin valves, in order to determine the different contributions to the spin relaxation. From a careful analysis based on the Elliott-Yafet mechanism, we found that the spin-flip probabilities coming from the phonons and the defects are both temperature and thickness independent. Whereas the temperature dependence of the spin relaxation is given by the phonon scattering as in bulk Cu, the temperature-independent part comes from defect scattering, which increases with decreasing thickness. Surprisingly, defect scattering in our Cu nanowires is clearly dominated by the grain boundaries rather than the surface.

In addition, we also compared the spin transport properties of Cu when using different FM electrodes. We found that the values and temperature dependence of λ_{Cu} are the same regardless of the FM material used. This result shows that no contamination from the FM material into the NM channel is induced.

Furthermore, the maximum in the spin-diffusion length of Cu observed at low temperatures, a puzzling feature reported before [1, 2, 4–7], can not be explained by the Elliott-Yafet mechanism. Instead of that, it is attributed to a temperature-dependent spin-flip probability arising from magnetic impurities present in the bulk of the Cu channel.

Although additional spin-relaxation contributions are unavoidable in confined nanostructures such as metallic nanowires, increasing the grain size or reducing the amount of magnetic impurities during the fabrication of spintronic nanodevices can be an efficient approach to overcome such limitations, leading to an improvement of the spin transport.

References

[1] T. Kimura, T. Sato, and Y. Otani, Phys. Rev. Lett. **100**, 066602 (2008).

[2] G. Mihajlović, J. E. Pearson, S. D. Bader, and A. Hoffmann, Phys. Rev. Lett. **104**, 237202 (2010).

[3] M. Erekhinsky, A. Sharoni, F. Casanova, and I. K. Schuller, Appl. Phys. Lett. **96**, 022513 (2010).

[4] H. Idzuchi, Y. Fukuma, L. Wang, and Y. Otani, Appl. Phys. Lett. **101**, 022415 (2012).

[5] H. Zou and Y. Ji, Appl. Phys. Lett. **101**, 082401 (2012).

[6] F. Casanova, A. Sharoni, M. Erekhinsky, and I. K. Schuller, Phys. Rev. B **79**, 184415 (2009).

[7] L. O'Brien, M. J. Erickson, D. Spivak, H. Ambaye, R. J. Goyette, V. Lauter, P. A. Crowell, and C. Leighton, Nat. Comm. **5**, 3927 (2014).

[8] F. J. Jedema, A. T. Filip, and B. J. van Wees, Nature **410**, 345 (2001).

[9] T. Kimura, J. Hamrle, and Y. Otani, Phys. Rev. B **72**, 014461 (2005).

[10] *Electrons and Phonons*, J. M. Ziman (Clarendon, Oxford, 1960).

[11] A. Bid, A. Bora, and A. K. Raychaudhuri, Phys. Rev. B **74**, 035426 (2006).

[12] P. Monod and F. Beuneu, Phys. Rev. B **19**, 911 (1979).

[13] N. Artunç and Z. Z. Öztürk, J. Phys.: Condens. Matter **5**, 559 (1993).

[14] W. Steinhögl, G. Schindler, G. Steinlesberger, and M. Engelhardt, Phys. Rev. B **66**, 075414 (2002).

[15] W. Wu, S. H. Brongersma, M. van de Hove, and K. Maex, Appl. Phys. Lett. **84**, 2838 (2004).

[16] A. F. Mayadas and M. Shatzkes, Phys. Rev. B **1**, 1382 (1970).

[17] W. Steinhögl, G. Schindler, G. Steinlesberger, M. Traving, and M. Engelhardt, J. Appl. Phys. **97**, 023706 (2005).

[18] F. J. Jedema, M. S. Nijboer, A. T. Filip, and B. J. van Wees, Phys. Rev. B **67**, 085319 (2003).

[19] R. J. Elliott, Phys. Rev., **96**, 266 (1954).

[20] Y. Yafet, in *Solid State Physics*, edited by F. Seitz and D. Turnbull (Academic, New York, 1963), pp. 1-98.

[21] F. Beuneu and P. Monod, Phys. Rev. B **13**, 3424 (1976).

Chapter 7

Effect of the interface resistance in non-local Hanle measurements

In Chapter 2 we explained that Hanle effect is an effective tool for spin manipulation. In addition to that, it presents an important advantage in the study of the spin-injection and spin-transport mechanisms, because it allows us to obtain the spin polarization of the FM material (α_F), of the FM/NM interface (P_I) and the spin-diffusion length of the NM material (λ_N) by using a single LSV [1–6], as opposed to the conventional non-local spin valve (NLSV) method, which needs several LSVs with different distances (L) between the FM electrodes in order to obtain these parameters [7–9] (as explained in section 4.1 and used in Chapters 5 and 6). However, Hanle measurements are very sensitive to different device details, such as the contact resistance [5, 6] or the finite length of the NM channel [10]. The used model has also been widely discussed in terms of the liability of the obtained information from Hanle measurements. It has been suggested that it is not possible to measure Hanle effect with transparent interfaces [1,9] or that, if doing so, the equation needs to be carefully chosen [5, 6].

In this Chapter, we study the validity of Eq. 2.18 by fitting Hanle measurements obtained in LSVs with different interface resistances to such equation. The obtained parameters were compared to those obtained from the fitting of the NLSV measurements as a function of L to Eq. 2.7 in the very same devices. Whereas in the presence of a contact resistance both methods are in good agreement, we observe an anomalous behavior for the case with transparent contacts, where there is a clear mismatch between both methods for L of the order of λ_N or larger. For L larger than λ_N this disagreement can be solved by taking into account the recently proposed spin absorption anisotropy at the FM electrodes [6] and, thus, applying Eq. 2.19. However, when L is of the order of λ_N the mismatch is still present, evidencing that additional unidentified effects are influencing the spin transport. Our analysis shows the complexity of an accurate fitting of the non-local Hanle measurements, a widely used technique to extract relevant spin transport parameters.

7.1 Experimental appoach

In order to carry out the study, Py/Cu and Co/Cu LSVs were compared. The reason for choosing different materials as FM electrodes is the need of different

FM/NM interface resistances. In Chapter 3 (section 3.1.2) we already explained that Py has given us high quality transparent interfaces with a high spin polarization, whereas Co is easily oxidized allowing the fabrication of an interface with a non-zero resistance. It is important to note that, contrary to what we did in Chapters 5 and 6, where Cu was deposited right after the interface milling of Co, in this case Co was oxidized on purpose. The interface resistance, R_I, was measured in all samples, where a cross-shaped junction was fabricated in addition to the regular LSVs. Several samples were fabricated and measured (all of them containing LSVs with different L). Since all the obtained results are very reproducible, for the sake of simplicity, in this Chapter the focus will be only on two samples. Sample #1 consists of Co/Cu LSVs with 35-nm-thick Co electrodes of widths $w_{F1} \sim 90$ nm and $w_{F2} \sim 150$ nm and a resistivity of $\rho_{Co} = 15.7$ $\mu\Omega$cm at 10 K. Sample #2 consists of Py/Cu LSVs with 35-nm-thick Py electrodes of widths $w_{F1} \sim 85$ nm and $w_{F2} \sim 135$ nm and a resistivity of $\rho_{Py} = 22.4$ $\mu\Omega$cm at 10 K. The Cu channel is 150 nm thick, $\sim$ 190 nm wide and has a resistivity of $\rho_{Cu} = 1.2$ $\mu\Omega$cm at 10 K in both samples.

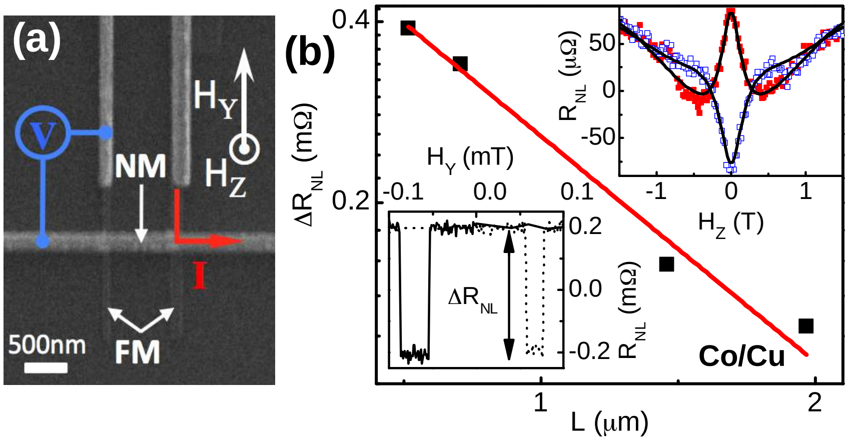

Figure 7.1: (a) Scanning electron microscopy (SEM) image of a LSV. The non-local measurement configuration, materials, and the directions of the in-plane and out-of-plane magnetic fields (H_Y and H_Z) are shown. (b) Spin signal ΔR_{NL} as a function of the distance L between FM electrodes, measured at 10 K for sample #1, which contains Co/Cu LSVs with a $R_I \sim 1$ Ω. Red solid line is a fit to Eq. 2.7. Lower inset: Non-local resistance R_{NL} as a function of H_Y measured at 10 K for the LSV with $L = 500$ nm. Solid (dotted) line indicates the decreasing (increasing) sweep of H_Y. ΔR_{NL} is tagged in the image. Upper inset: R_{NL} as a function of H_Z measured at 10 K both for the parallel (red solid squares) and antiparallel (blue empty squares) configuration of the FM electrodes for the LSV with $L = 1.5$ μm. Black solid lines are fits to Eq. 7.1 (using Eq. 2.18).

The $R_I \times A_I$ product (A_I is the contact area) measured in sample #1 is 2.8×10^{-2} $\Omega\mu$m^2 (therefore, the interface resistances have values of $R_{I1} = 1.6$ Ω and $R_{I2} = 1$ Ω), which are not transparent interfaces (Eq. 2.11) but cannot be considered to be in the fully tunneling regime (Eq. 2.13), hence the measured interface resistances fall in the intermediate regime [11], which is described by Eq. 2.7. The measured R_I at the Py/Cu junctions of sample #2 was negative, meaning that R_I is of the order or lower than the resistance of the electrodes [12,13] and $R_I \times A_I \leqslant 10^{-3}$ $\Omega\mu\text{m}^2$ (see section 3.1.2 for further details). Therefore, sample #2 is in the transparent regime [11].

Two types of measurements have been performed: (i) the NLSV measurements described in section 2.1, which consist in measuring R_{NL} as a function of the in-plane magnetic field along the FM electrodes (H_Y, as shown in Fig. 7.1(a)) and (ii) the Hanle measurements described in section 2.2.1, which consist in measuring R_{NL} as a function of the out-of-plane magnetic field (H_Z, see Fig. 7.1(a)). All measurements were done at 10 K.

In the first case, the obtained spin signal, ΔR_{NL}, as a function of L is fitted to Eq. 2.7 in order to obtain α_F, P_I (in the case of a non-zero interface resistance) and λ_{Cu} (see Fig. 7.1(b) and its lower inset).

In the second case, the R_{NL} as a function of H_Z obtained for each LSV should be fitted to Eq. 2.18 in order to obtain the same parameters. To be more precise, one needs to take into account that the magnetization of the FM electrodes can be tilted out-of-plane due to the magnetic field H_Z. The following equation is used to correct for such tilting [1,2,4]:

$$R_{NL}^{P(AP)}(H_Z,\theta) = \pm R_{NL}^{P}(H_Z)\cos^2\theta + |R_{NL}(H_Z=0)|\sin^2\theta \tag{7.1}$$

where "+" and "-" signs correspond to the P and AP magnetization states of the FM electrodes, $R_{NL}^{P}(H_Z)$ is the one from Eq. 2.18, and $\theta \equiv \theta(H_Z)$ is the angle between the magnetization of the FM electrodes and H_Z; its dependence with H_Z can be extracted from the anisotropic magnetoresistance (AMR) measurements of the FM electrodes as a function of H_Z [11]. Hence, in order to obtain α_F, P_I and λ_{Cu} from Hanle measurements, the data was fitted to Eq. 7.1 (see upper inset of Fig. 7.1(b)).

7.2 Comparison between NLSV and Hanle measurements

For sample #1, with a non-zero interface resistance, $P_I^{NLSV} = 0.043 \pm 0.003$, $\alpha_{Co}^{NLSV} = 0.038 \pm 0.004$ and $\lambda_{Cu}^{NLSV} = 1159 \pm 100$ nm were obtained from the fitting of the NLSV measurements to Eq. 2.7. Note that P_I and α_F are coupled, as can be seen from Eqs. 2.7 and 2.18, since sample #1 is not fully in the tunneling regime. Only when $\frac{P_I R_I}{1-P_I^2} >> \frac{\alpha_F R_F}{1-\alpha_F^2}$ or $\frac{P_I R_I}{1-P_I^2} << \frac{\alpha_F R_F}{1-\alpha_F^2}$ (*i.e.*, for the tunneling or transparent regimes [11]) they will decouple.

For the Hanle measurements, R_{NL} as a function of H_Z was measured for both the parallel (P) and antiparallel (AP) magnetization states (see upper inset of Fig. 7.1(b)), with identical results. For all the LSVs with different L, a spin-diffusion length ranging between $\lambda_{Cu}^{Hanle} = 987 \pm 25$ nm and 1107 ± 27 nm, and an interface polarization ranging between $P_I^{Hanle} = 0.044 \pm 0.001$ and 0.048 ± 0.001 were obtained. Due to the complexity of Eq. 2.18, the spin polarization of Co was fixed to $\alpha_{Co} = 0.038$. The obtained λ_{Cu}^{Hanle} and P_I values show no substantial deviation from the NLSV values for any of the distances L (see Fig. 7.2(a)).

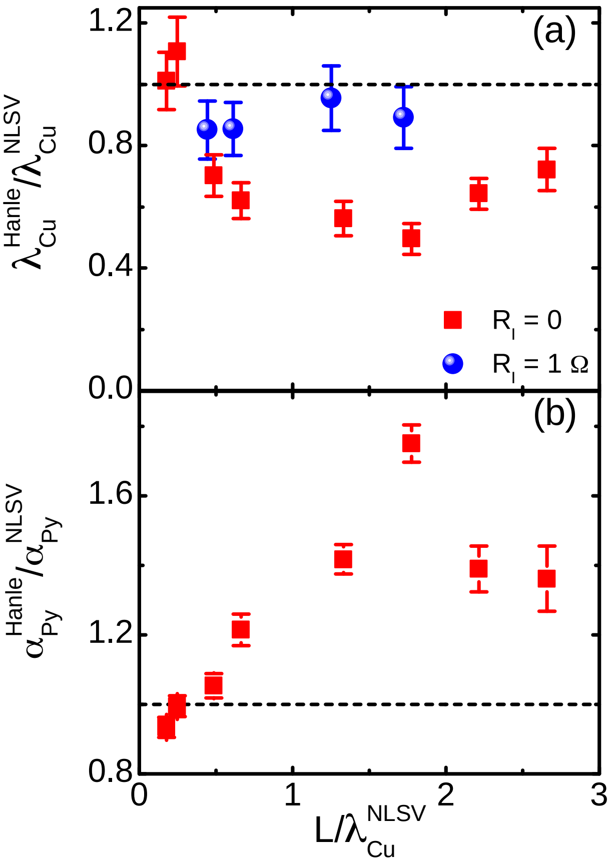

Figure 7.2: (a) Spin-diffusion length of Cu obtained from Hanle measurements (λ_{Cu}^{Hanle}) performed at 10 K as a function of the distance L between FM electrodes, for sample #1 containing Co/Cu LSVs with an $R_I \sim 1\ \Omega$ (blue solid circles) and sample #2 containing Py/Cu LSVs with transparent interfaces (red solid squares). Both λ_{Cu}^{Hanle} and L are normalized to the spin-diffusion length of Cu obtained from NLSV measurements (λ_{Cu}^{NLSV}) of each sample. (b) Spin polarization of Py obtained from Hanle measurements (α_{Py}^{Hanle}) as a function of L for sample #1. α_{Py}^{Hanle} and L are normalized to α_{Py}^{NLSV} and λ_{Cu}^{NLSV}, respectively.

For sample #2, with transparent interfaces, we can approximate $R_I = 0$ in Eqs. 2.7 and 2.18 in order to obtain α_{Py} and λ_{Cu}. From NLSV measurements as a function of L we obtained $\alpha_{Py}^{NLSV} = 0.36 \pm 0.01$ and $\lambda_{Cu}^{NLSV} = 1125 \pm 62$ nm. However, for Hanle measurements, spin-diffusion lengths ranging between $\lambda_{Cu}^{Hanle} = 557 \pm 26$ nm and 1245 ± 58 nm were obtained. The spin polarization of Py also changed between $\alpha_{Py}^{Hanle} = 0.34 \pm 0.01$ and 0.63 ± 0.02. Note that in this case R_{NL} as a function of H_Z was only measured for the P magnetization configuration of the FM electrodes since Py is a soft magnetic material. Therefore, when starting from an initial AP state, the magnetization of one of the electrodes was always swiped back into the P state in the presence of a high enough H_Z, preventing us from measuring R_{NL} at the AP state for the whole range of H_Z.

As shown in Fig. 7.2(a), the obtained λ_{Cu}^{Hanle} values present a clear deviation from the NLSV values with a strong dependence on L: for low values of L (*i.e.*, $L << \lambda_{Cu}^{NLSV}$) the agreement between both methods is excellent but, as L increases, λ_{Cu}^{Hanle} starts to deviate from λ_{Cu}^{NLSV}. The highest discrepancy occurs for $L \sim \lambda_{Cu}^{NLSV}$ and, for longer L (*i.e.*, $L >> \lambda_{Cu}^{NLSV}$), the deviation of λ_{Cu}^{Hanle} tends to reduce. α_{Py}^{Hanle} changes with the opposite tendency to that of λ_{Cu}^{Hanle}, showing a coupling between both fitting parameters (see Fig. 7.2(b)).

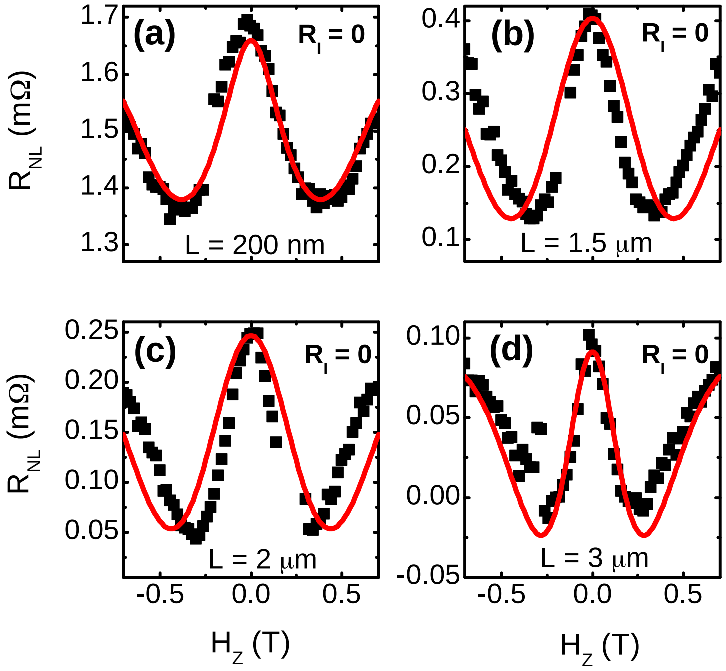

Figure 7.3: Non-local resistance R_{NL} as a function of H_Z (black squares) measured at 10 K for sample #2, which consists of Py/Cu LSVs with transparent interfaces. L ranges from 200 nm to 3 μm. Red solid lines are fits to Eq. 7.1 (using R_{NL} from Eq. 2.18).

The observed deviation in the $L \sim \lambda_{Cu}^{NLSV}$ regime agrees with a bad fitting of the Hanle data, measured in sample #2, to Eq. 7.1 (using R_{NL} from Eq. 2.18). As shown in Fig. 7.3(b)-(c), in this regime the fitted curve tends to be wider than the measured data, which decreases considerably the fitted value of λ_{Cu}^{Hanle} (increasing, in turn, the value of α_{Py}^{Hanle}). The agreement between the measured data and the fitted curve is only good for the $L << \lambda_{Cu}^{NLSV}$ regime (Fig. 7.3(a)), whereas for $L >> \lambda_{Cu}^{NLSV}$ the data and the curve tend to converge again (Fig. 7.3(d)). This suggests that Eq. 7.1 (using the R_{NL} from Eq. 2.18) is not valid for the $L \sim \lambda_{Cu}^{NLSV}$ regime, where additional effects might need to be considered in the spin transport in Cu.

At this point, we would like to emphasize that other samples with the same interface resistance have the same behavior and, thus, the observed deviation is intrinsic to LSVs with transparent contacts, as can be observed in Fig. 7.4.

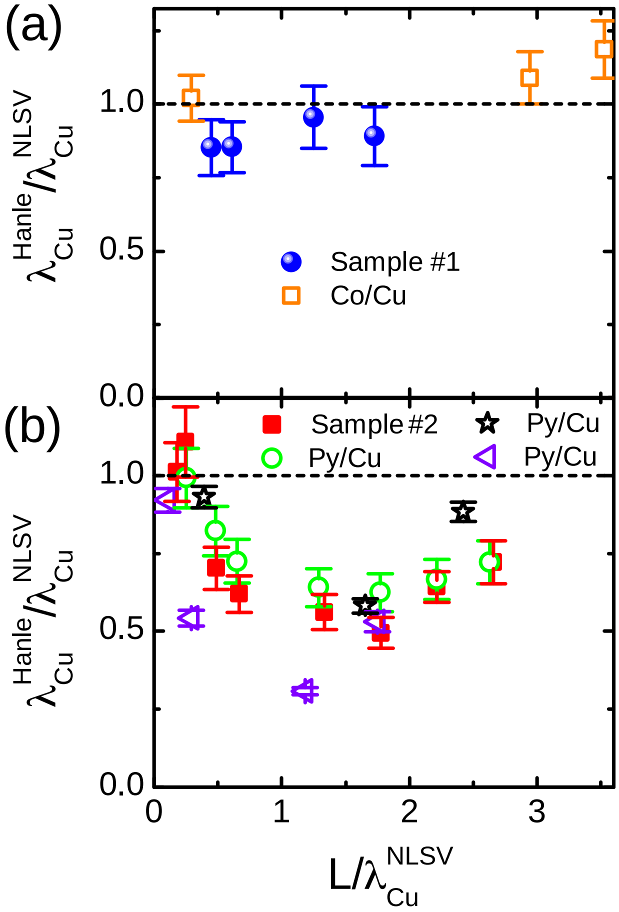

Figure 7.4: λ_{Cu}^{Hanle} obtained at 10 K as a function of L for (a) Co/Cu LSVs with $R_I \sim$ 1 Ω and (b) Py/Cu LSVs with transparent interfaces. Both λ_{Cu}^{Hanle} and L are normalized to the λ_{Cu}^{NLSV} value of each sample.

7.3 Effect of the anisotropic spin absorption at FM/NM interfaces

Whereas Maasen *et al.* reported an anomalous behavior of the parameters obtained from Hanle measurements due to a bad fitting, where the backflow of spins at the FM electrodes was not considered [5], this is not the case in the present work, since Eq. 2.18 explicitly takes into account the role of the interface resistances. Very recently, Idzuchi and co-workers [6] have proposed the difference in the spin absorption mechanisms for longitudinal and transverse spin currents as the reason of the disagreement in the Hanle measurement in LSVs without tunnel barriers, describing the measured non-local resistance with Eq. 2.19 (see section 2.2.1). According to this work, in LSVs with transparent interfaces, the anisotropic spin absorption by the FM electrodes alters the spatial distribution of the chemical potential. Therefore, the spin transport is also altered, more pronouncedly for short L. This could explain the strong deviation between λ_{Cu}^{Hanle} and λ_{Cu}^{NLSV} in the $L \sim \lambda_{Cu}^{NLSV}$ regime, but one would expect an even stronger deviation in the $L << \lambda_{Cu}^{NLSV}$ regime. Instead, we find the opposite trend.

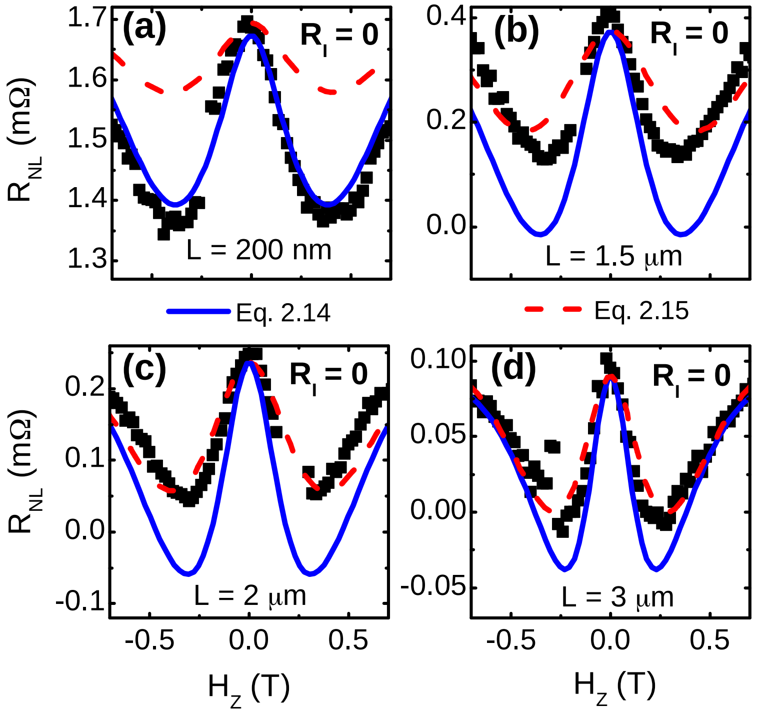

Figure 7.5: Non-local resistance R_{NL} as a function of H_Y (black squares) measured at 10 K for sample #2. L ranges from 200 nm to 3 μm. Blue solid (red dashed) line is a simulation of Eq. 7.1 using the R_{NL} from Eq. 2.18 (2.19). α_{Py}^{NLSV} and λ_{Cu}^{NLSV} obtained from NLSV measurements were used, and a real part of the spin-mixing conductance between Py and Cu of $G_r = 3.9 \times 10^{14}$ $\Omega^{-1}\text{m}^{-2}$ was assumed.

In order to clarify this issue, Fig. 7.5 shows the measured R_{NL} as a function of H_Z in sample #2 for the same regimes as in Fig. 7.3, together with the simulated curves of Eq. 7.1, with the R_{NL} expression from both Eq. 2.18 and 2.19. For the simulations, we took the α_{Py}^{NLSV} and λ_{Cu}^{NLSV} values obtained from the fittings of the NLSV measurements. A value of $G_r = 3.9 \times 10^{14}$ $\Omega^{-1}\text{m}^{-2}$ was used for the real part of the spin-mixing conductance of the Py/Cu interface [6, 14, 15] (see section 2.2.2 for an explanation of this magnitude). The figure shows a clear agreement between the measured data and Eq. 2.18 for $L << \lambda_{Cu}^{NLSV}$, the same way there is an excellent agreement between the fitted λ_{Cu}^{Hanle} and λ_{Cu}^{NLSV}. For the $L >> \lambda_{Cu}^{NLSV}$ regime, Eq. 2.19 follows quite accurately the measured data. In addition, both simulated curves tend to converge, which is expected since the spatial distribution of the chemical potential is, overall, less altered. However, in the $L \sim \lambda_{Cu}^{NLSV}$ regime none of the curves are able to reproduce the measured data.

In order to obtain the value of λ_{Cu} by fitting Eq. 7.1 with R_{NL} from Eq. 2.19, we fixed all the parameters except for λ_{Cu}^{Hanle}, which was left as the fitting parameter. This was done for the sake of simplicity, given the complex form of the equation. Figure 7.6 shows the obtained values of λ_{Cu}^{Hanle} as a function of L using Eq. 2.19. The tendency is the same we see in the simulations, where λ_{Cu}^{Hanle} and λ_{Cu}^{NLSV} converge in the $L >> \lambda_{Cu}^{NLSV}$ regime. For comparison, the λ_{Cu}^{Hanle} values obtained by using Eq. 2.18, already shown in Fig. 7.2, are also plotted.

7.4 Discussion

Even if Eq. 2.18 accounts for the interface resistance, it does not accurately fit the measured data. In turn, Eq. 2.19, which considers the anisotropic spin absorption at the FM/NM interfaces, is more accurate when $L >> \lambda_{Cu}^{NLSV}$, and the fitted λ_{Cu}^{Hanle} presents no substantial deviation from λ_{Cu}^{NLSV}. However, Eq. 2.19 does not work at the $L \sim \lambda_{Cu}^{NLSV}$ and $L << \lambda_{Cu}^{NLSV}$ regime, showing that both the spin backflow and the anisotropic spin absorption are not enough to account for the disagreement between the current Hanle models and the measured curves.

The effect of the nearby electrodes is also considered as a possible source of interference, due to the design of our devices, which consist of several LSVs on a row. However, by systematically varying the distance of the nearby Py/Cu LSVs with transparent interfaces, the same behavior as in Figs. 7.2 is observed, ruling out any effect coming from the adjacent electrodes. The results of two control samples where the distance between the Py electrodes was varied are shown in Fig. 7.4.

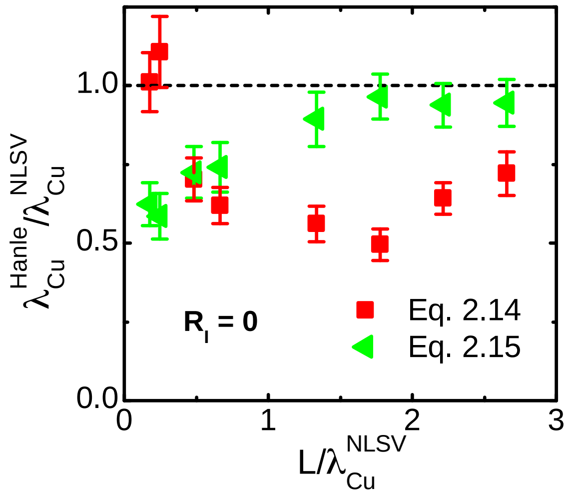

Figure 7.6: λ_{Cu}^{Hanle} obtained at 10 K from the fitting of Eq. 7.1 by using Eq. 2.18 (red squares) and Eq. 2.19 (green triangles) as a function L for sample #2, which consists of Py/Cu LSVs with transparent interfaces. Both λ_{Cu}^{Hanle} and L are normalized to λ_{Cu}^{NLSV}.

Finally, the origin of this discrepancy could be attributed to the use of a 1D model, which, at $L < \lambda_{Cu}^{NLSV}$, could no longer be a good approximation [16].

7.5 Conclusions

To summarize, we performed non-local Hanle measurements in LSVs with transparent and finite interface resistances, and we compared the spin-diffusion length of the Cu channel, λ_{Cu}, obtained from such measurements to the one obtained from NLSV measurements as a function of L. In the case where we have a finite FM/NM interface resistance, both methods are in excellent agreement. However, in the case of transparent interfaces an anomalous behavior is observed, which depends on the distance L between both FM electrodes. Even though taking into account the spin backflow and the anisotropic spin absorption at the transparent FM/NM interfaces can explain some of the observed disagreements, a new interference effect that influences the non-local Hanle measurements is detected. Such effect is beyond the understanding of the current theory of spin injection and transport and is maximized when L is of the order of λ_{Cu}. Hence, care should be taken when obtaining spin transport information from such type of measurements in LSVs with transparent interfaces.

References

[1] F. J. Jedema, H. B. Heersche, A. T. Filip, J. J. A. Baselmans, and B. J. van Wees, Nature **416**, 713 (2002).

[2] G. Mihajlović, J. E. Pearson, and A. Hoffmann, Phys. Rev. Lett. **104**, 237202 (2010).

[3] Y. Fukuma, L. Wang, H. Idzuchi, S. Takashi, S. Maekawa, and Y. Otani, Nat. Mater. **10**, 527 (2010).

[4] J.-C. Rojas Sánchez, P. Łączkwoski, W. F. Savero Torres, M. Cubukcu, V. D. Nguyen, L. Notin, C. Beigné, C. Vergnaud, A. Marty, M. Jamet, L. Vila, and J. P. Attané, Appl. Phys. Lett. **102**, 132408 (2013).

[5] T. Maasen, I. J. Vera-Marun, M. H. D. Guimarães, And B. J. van Wees, Phys. Rev. B, *86*, 235408 (2012).

[6] H. Idzuchi, Y. Fukuma, S. Takahashi, S. Maekawa, and Y. Otani, Phys. Rev. B **89**, 081308(R) (2014).

[7] F. J. Jedema, M. S. Nijboer, A. T. Filip, and B. J. van Wees, Phys. Rev. B **67**, 085319 (2003).

[8] M. Erekhinsky, A. Sharoni, F. Casanova, and I. K. Schuller, Appl. Phys. Lett. **96**, 022513 (2010).

[9] T. Kimura, T. Sato, and Y. Otani, Phys. Rev. Lett. **100**, 066602 (2008).

[10] M. Wojtaszek, I. J. Vera-Marun, and B. J. van Wees, Phys. Rev. B **89**,245427 (2014).

[11] S. Takahashi and S. Maekawa, Phys. Rev. B **67**, 052409 (2003).

[12] R. J. Pedersen and F. L. Vernon, Jr., Appl. Phys. Lett. **10**, 29 (1976).

[13] J. M. Pomeroy and H. Grube, J. Appl. Phys. **105**, 094503 (2009).

[14] Y. Tserkovnyak, A. Brataas, and G. E. W. Bauer, Phys. Rev. B **66**, 224403 (2002).

[15] G. E. W. Bauer, Y. Tserkovnyak, D. Huertas-Hernando, and A. Brataas, Phys. Rev. B **67**, 094421 (2003).

[16] B. T. Bolon, L. O'Brien, N. Krueger, T. Peterson, D. Spivak, M. Erickson, C. C. Geppert, C. Leighton, and P. A. Crowell, 59th Annual Magnetism & Magnetic Materials Conference, Honolulu (Hawaii) November 3-7 (2014), Abstract FW-03, p. 668.

Chapter 8

Magnetic gating of pure spin currents

The most basic unit in an envisioned spin-only circuit that would integrate logics and memory [1] is the spin analogue to the transistor, in which the manipulation of pure spin currents is crucial. The original proposal by Datta and Das [2], which is also applicable to pure spin currents [3], suggested a spin manipulation that would arise from the spin precession due to the spin-orbit interaction modulated by an electric field (Rashba coupling). However, a fundamental limitation appears here, because the best materials for spin transport are those showing the lowest spin-orbit interaction and, therefore, there has been no success in electrically manipulating the spins and propagating them at the same environment, with few exceptions [3].

Alternative ways to control pure spin currents are thus desirable. One could take advantage of the spin-mixing conductance concept [4–6] at NM/FM insulator (FMI) interfaces, which governs the interaction between the spin currents present at the NM and the magnetization of the FMI. This concept is at the base of new spin-dependent phenomena, including the spin pumping [6–12] and spin Seebeck effect [6, 13] or the recently discovered spin Hall magnetoresistance (SMR) [6, 14–18], explained in section 2.2.2. In these cases, a NM with a large SOC is required to convert the involved spin currents into charge currents *via* the inverse Spin Hall effect [19].

In this Chapter, we demonstrate an alternative way of modulating pure spin currents based on magnetic, instead of electric, gating. To that end, we fabricate LSVs on top of a FMI, in order to enable the magnetic gating of the pure spin currents. The basic idea is depicted in Fig. 8.1: when the spin polarization ($\vec{s}$) has the same orientation as the magnetization ($\vec{M}$) of the FMI, the spin current reaching the detector will not vary with respect to the case where no FMI is used (Fig. 8.1(a)). However, when $\vec{s}$ and $\vec{M}$ are non-collinear, part of the spin current will be absorbed by $\vec{M}$ *via* spin-transfer torque [20–22], leading to a maximum spin absorption in the case where $\vec{M}$ and $\vec{s}$ are perpendicular (Fig. 8.1(b)). By using LSVs, we are able to extract the spin-mixing conductance of NM/FMI interfaces in the absence of charge currents, which otherwise could lead to spurious effects as suggested by some authors [23, 24]. Furthermore, the use of NM metals with low atomic number, optimal for spin transport in LSVs, rules out spin-orbit interaction effects that might exist for other systems, such as

Pt/YIG [25].

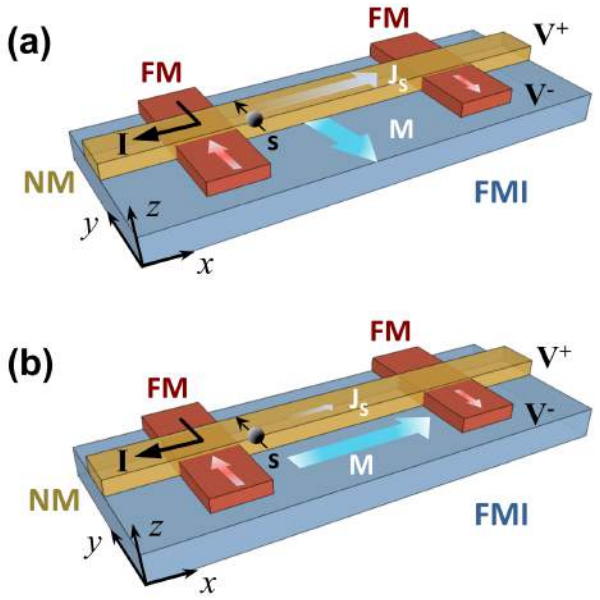

Figure 8.1: Scheme of the device used to modulate a pure spin current with magnetic gating. It consists on a ferromagnetic (FM)/ non-magnetic (NM) lateral spin valve on top of a ferromagnetic insulator (FMI). The non-local measurement configuration is shown. x, y and z axes are indicated as used in the text. (a) When the magnetization of the FMI ($\vec{M}$) and the polarization ($\vec{s}$) of the injected pure spin current ($\vec{J_S}$) are parallel, there will be no spin absorption. (b) When $\vec{M}$ and $\vec{s}$ are perpendicular, the spin absorption will be maximum.

8.1 Experimental approach

We chose $Y_3Fe_5O_{12}$ (YIG) as a magnetic gate because it is ferromagnetically soft and has a negligible magnetic anisotropy. M (which is isotropic in-plane) as a function of the applied in-plane magnetic field (H) measured by vibrating sample magnetometry (VSM) saturates at $\sim$ 100 Oe (Fig. 8.3(a)), allowing the control of $\vec{M}$ above this field. The YIG was grown by liquid phase epitaxy on a (111) gadolinium gallium garnet (GGG) single crystal at Innovent e. V. (Jena, Germany). Co/Cu LSVs (shown in Fig. 8.3(b)) were fabricated with 35-nm-thick and $\sim$ 115-nm and $\sim$ 175-nm-wide Co electrodes; the edge-to-edge distances between the FM electrodes were $L = 250$ nm, $L = 570$ nm and $L = 1600$ nm. The Cu channel was 100 nm thick and $\sim$ 200 nm wide and had an electrical resistivity of 2.1 $\mu\Omega$cm at 150 K (see inset of Fig. 8.2). Co electrodes were oxidized on purpose before the deposition of the Cu in order to overcome their low spin-injection efficiency. The interface resistance was estimated to be $R_I \geqslant 5\ \Omega$. Two types of measurements were performed: (i) R_{NL} measurements by varying the intensity of the magnetic field H, whose direction was fixed parallel to the magnetization of the Co electrodes and (ii) R_{NL} measurements by varying the direction of the magnetic field H, whose value was fixed, with an angle α with respect to the magnetization of the FM electrodes. Unless something else is specified, all the measurements referred in this Chapter were done at 150 K.

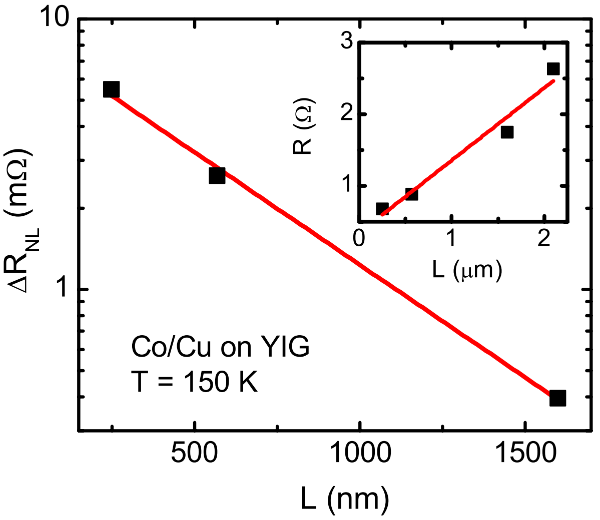

Figure 8.2: Spin signal as a function of the distance L between FM electrodes (black squares) measured in a Co/Cu LSV on top of YIG at 150 K. Red solid line is a fit to Eq. 2.13. The inset shows the electrical resistance of the Cu channel as a function of L (black squares) measured in the same device at 150 K and the linear fit (red solid line) in order to obtain the value of the resistivity.

8.2 The NLSV effect

The first type of measurement was done in order to show the standard performance of a LSV. This measurement (Fig. 8.3(c)) is an unambiguous demonstration that a pure spin current is transported along the Cu channel [26–29], as shown throughout this thesis (see section 2.1 for details).

Fitting the ΔR_{NL} *vs* L measurements to Eq. 2.13 (Fig. 8.2), the interface spin polarization and the spin-diffusion length of Cu were obtained. At 150 K, their values are $P_I = 0.18 \pm 0.01$ and $\lambda = 522 \pm 25$ nm. P_I is within the range of values that are observed in literature in similar systems [26–29]; λ_{Cu} is similar but slightly lower than our previous values obtained in Py/Cu LSVs (with a Cu thickness of 100 nm) on top of Si/SiO$_2$ measured at 150 K ($\lambda = 680 \pm 15$ nm) (Chapter 6). This could be due to the different growth of Cu on top of YIG as compared to SiO$_2$.

It is worth noting that the relative magnetization of the Co electrodes changes at $H \geqslant 400$ Oe, far above the saturation field of YIG (~ 100 Oe). This detail is important for the performance of the next measurement.

8.3 Modulation of the spin current

The second type of measurement (R_{NL} as a function of α by fixing the value of H) was done for both the P and AP configuration of the Co electrodes, which can be chosen with the proper magnetic field history. In this case, H was fixed to 250 Oe (see dots in Fig. 8.3(c)), which is enough to control $\vec{M}$ of YIG but does not affect the magnetization of the Co electrodes. As intended, Fig. 8.3(d) shows a clear modulation of the measured R_{NL} (*i.e.*, a modulation of the spin current) when $\vec{M}$ of YIG is rotated in plane, clearly demonstrating a direct magnetic gating to a pure spin current.

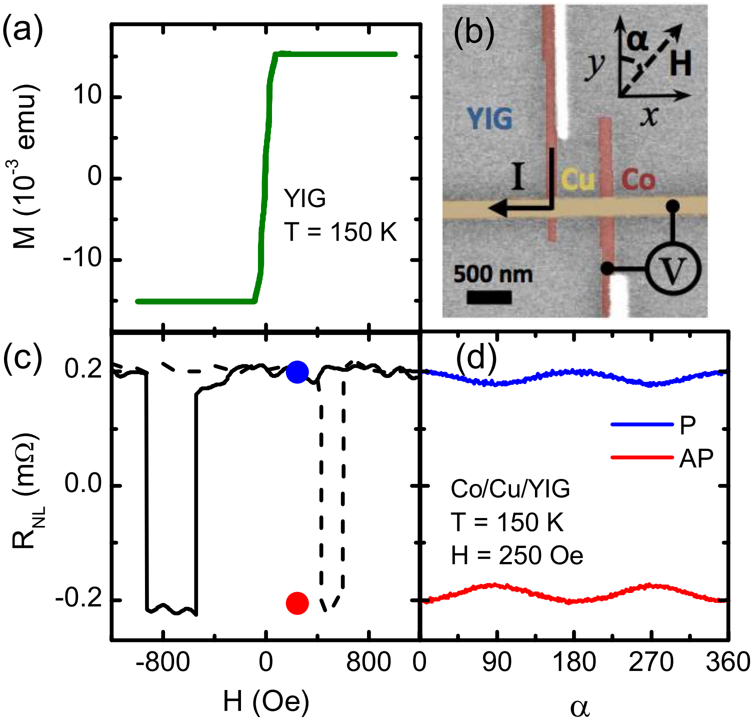

Figure 8.3: (a) Magnetization of YIG (M) as a function of the applied in-plane magnetic field H measured at 150 K. (b) Colored SEM image of a LSV. The non-local measurement configuration, materials, direction of H and its angle α with respect to the FM electrodes are shown. (c) Non-local resistance (R_{NL}) measured at 150 K as a function of H with $\alpha = 0°$ for a LSV with a separation distance between Co electrodes of $L = 1.6$ μm. Solid (dashed) line indicates the decreasing (increasing) sweep of H. A constant background of 0.14 $m\Omega$ is subtracted from the data. Blue and red dots correspond to the value of R_{NL} at the P and AP configuration of the Co electrodes, respectively, at $H = 250$ Oe. (d) R_{NL} as a function of α, measured for both the P and AP configuration, at 150 K with $H = 250$ Oe for the same LSV.

The total change in R_{NL}, caused by the spin absorption at the Cu/YIG interface, is defined as the non-local modulation $\delta R_{NL} = R_{NL}(\alpha = 0°) - R_{NL}(\alpha = 90°)$ and is tagged in Fig. 8.4. This figure contains the same data shown in Fig. 8.3(d) although, for the sake of clarity, the P and AP configurations are plotted separately. In this case, for a distance between Co electrodes of $L = 1.6$ μm, δR_{NL} has a magnitude of ~ 0.025 mΩ. We can define the factor

$$\beta = \frac{\delta R_{NL}}{R_{NL}(\alpha = 0°)} = 1 - \frac{R_{NL}(\alpha = 90°)}{R_{NL}(\alpha = 0°)} \tag{8.1}$$

as an analogue of a magnetoresistance, which gives us a measure of the efficiency of the magnetic gating. A β factor of 8.33% is obtained for the LSV with $L = 1.6$ μm, whereas $\beta = 2.96\%$ for $L = 570$ nm, showing that longer channels provide more efficient modulations. The LSV with $L = 250$ nm broke after the R_{NL} *vs* H_Y measurement and, thus, the non-local modulation was impossible to measure.

The reflection symmetry between the P and AP modulations (Figs. 8.3(d) and 8.4) rules out the possibility of a relative tilting between the magnetization of Co electrodes, which could be caused by the torque exerted directly by the applied magnetic field or/and by a coupling between the Co electrodes and the YIG substrate. A modulation in R_{NL} originated from the rotation of the magnetization of the Co electrodes (angles θ_1, θ_2 with respect to the easy axis defined by shape anisotropy) would be given by $R_{NL} \propto \cos\theta$, where θ is the relative angle between Co magnetizations. Since $\theta = \theta_1 - \theta_2$ in the P case, whereas in the AP case $\theta = 180° - \theta_1 - \theta_2$, this would lead to a different amplitude modulation not observed in our experiment. Only in the special case where the narrower electrode does not rotate at all ($\theta_2 \sim 0$) the modulations corresponding to the P and AP cases would be identical. The wider electrode should then rotate as much as $\theta_1 \sim 23°$ to observe an $\sim$ 8% modulation, which was ruled out by means of MOKE microscopy. This control experiment is described below (Appendix 8.A).

An additional control experiment, by repeating the R_{NL} *vs* α measurements on top of a SiO$_2$ substrate, was performed in order to rule out any other possible artifact (Appendix 8.B).

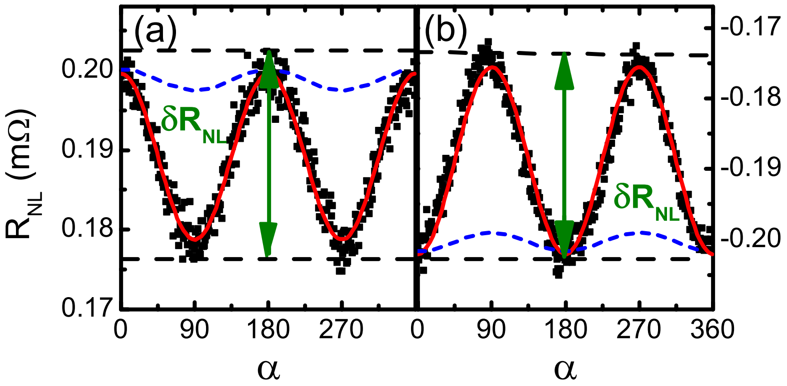

Figure 8.4: Non-local resistance (black solid squares) as a function of the angle α between the FM electrodes and the applied magnetic field H, measured for the parallel (a) and antiparallel (b) configuration, at 150 K and $H = 250$ Oe for a LSV with a separation distance of $L = 1.6$ μm. Red solid line corresponds to the fit of the data to Eq. 8.14. Blue dashed line corresponds to Eq. 8.14 in the absence of FMI/NM interface spin-mixing conductance. The non-local modulation δR_{NL} is tagged.

8.4 Theory

In order to quantify the observed modulation of R_{NL}, Eq. 2.17 needs to be solved with the proper boundary conditions. The geometry shown in Fig. 8.1 is considered; at $x = 0$ the FM injector drives a charge current I that flows to the $x < 0$

direction. We assume that the system is invariant in y direction and therefore, the spin accumulation only depends on x and z: $\mu_s(x,z)$. In addition, at the upper interface of the NM with the vacuum the spin current should vanish. In the absence of spin-orbit coupling, the spin current density in the NM $\vec{j}_k$ (the vector denotes the spin polarization direction and k denotes the flow direction) is then originated by the gradient of the spin accumulation μ_s^a

$$\vec{j}_k = -\frac{1}{2e\rho_N}\partial_k\vec{\mu}_s \; . \tag{8.2}$$

Therefore, the spin accumulation at the upper interface satisfies the following condition:

$$\partial_z\vec{\mu}_s|_{z=t_N} = 0 \; . \tag{8.3}$$

We are assuming $z=0$ at the NM/FMI interface, and $z=t_N$ at the NM/vacuum interface. At the interface with the FMI we use the Brataas-Nazarov-Bauer boundary condition [29]:

$$\partial_z\vec{\mu}_s|_{z=0} = -2\rho_N\left[G_r\hat{m}\times(\hat{m}\times\vec{\mu}_s) + G_i\hat{m}\times\vec{\mu}_s\right] \; , \tag{8.4}$$

where $\hat{m}$ is a unit vector along the magnetization of the FMI, and $G_{mix} = G_r + iG_i$ is the complex spin-mixing interface conductance per unit area [4,5]. In LSV experiments, the thickness t_N of the NM layer is generally smaller than the characteristic scale of variation of μ_s ($\approx \lambda_N$) and therefore we can integrate Eq. 2.17 over z assuming that μ_s does not depend on z. By performing this integration and using Eqs. 8.3-8.4 we obtain the following 1D equation for $\vec{\mu}_s$:

$$\partial^2_{xx}\vec{\mu}_s = \frac{\vec{\mu}_s}{\lambda_N^2} + \left(\frac{1}{\lambda_m^2} + \frac{1}{\lambda_i^2}\right)\vec{\mu}_s\times\hat{m} - \frac{1}{\lambda_r^2}\hat{m}\times(\hat{m}\times\vec{\mu}_s) \; . \tag{8.5}$$

We have considered an in-plane magnetization of the FMI, $\hat{m} = (\sin\alpha, \cos\alpha, 0)$, and defined $\lambda_r^{-2} = 2\rho_N G_r/t_N$ and $\lambda_i^{-2} = 2\rho_N G_i/t_N$. The latter term acts as an effective magnetic field parallel to the magnetization of the FMI which is assumed to be parallel to the applied magnetic field. The magnetic length $\lambda_m = \sqrt{D\hbar/2\mu_B B}$ is defined in section 2.2.1.

Equation 8.5 describes the spatial dependence of the spin accumulation in a thin NM layer in contact with a FMI. It consists of three coupled linear second order differential equations. In order to solve it we have to write the boundary conditions corresponding to the experimental situation: at $x=0$ an electric current I is injected, which induces at $x=0$ a spin current equal to $P_I I$. At a distance L from the injection point there is a detector. The spin accumulation and its derivative are continuous in the NM layer. The boundary conditions for $\vec{\mu}_s(x)$ at the injector and detector are obtained from the spin current continuity and read:

$$P_I I\hat{y} = -\frac{\lambda_N}{eR_N}\partial_x\vec{\mu}_s|_{x=0^-} - \frac{\lambda_N}{eR_N}\partial_x\vec{\mu}_s|_{x=0^+} \; , \tag{8.6}$$

$$0 = -\frac{\lambda_N}{eR_N}\partial_x\vec{\mu}_s|_{x=L^-} - \frac{\lambda_N}{eR_N}\partial_x\vec{\mu}_s|_{x=L^+} \; , \tag{8.7}$$

where the spin current at both sides of the FM injector (detector) is considered. The FM injector is polarized in y direction (whose unit vector is $\hat{y}$) due to shape anisotropy, and, thus, the injected spin current as well. In order to obtain the boundary conditions Eqs. 8.6-8.7, a high interface resistance (R_I) was considered at the interfaces between the NM and the FM injector ($x = 0$) and between the NM and the FM detector ($x = L$) [30], *i.e.*, $R_I >> R_N$ (please remember that $R_N = \rho_N \lambda_N / w_N t_N$ is the spin resistance of the NM channel). If R_I is of the order of R_N, a spin current that might flow back into the FM electrodes [31,32] has to be taken into account.

In the case considered above, it is rather straightforward to solve Eq. 8.5 with the conditions Eqs. 8.6-8.7, in order to obtain the spin accumulation in all three spin polarization directions:

$$\begin{aligned} \mu_s^x(x) &= P_I I e R_N \cos\alpha \sin\alpha \left[e^{-x/\lambda_N} + \mathrm{Re}\left(\frac{\lambda_1}{\lambda_N} e^{-x/\lambda_1} \right) \right] , & (8.8) \\ \mu_s^y(x) &= P_I I e R_N \left[\cos^2\alpha e^{-x/\lambda_N} + \sin^2\alpha \mathrm{Re}\left(\frac{\lambda_1}{\lambda_N} e^{-x/\lambda_1} \right) \right] , & (8.9) \\ \mu_s^z(x) &= -P_I I e R_N \sin\alpha \mathrm{Im}\left(\frac{\lambda_1}{\lambda_N} e^{-x/\lambda_1} \right) , & (8.10) \end{aligned}$$

where the characteristic length in the second exponential is defined as

$$\lambda_1 = \frac{\lambda_N}{\sqrt{1 + \left(\frac{\lambda_N}{\lambda_r}\right)^2 + i\left[\left(\frac{\lambda_N}{\lambda_i}\right)^2 + \left(\frac{\lambda_N}{\lambda_m}\right)^2 \right]}} . \tag{8.11}$$

According to first-principle calculations, the imaginary part of the spin-mixing conductance can be neglected [22] and, therefore, λ_1 can be approximated to

$$\lambda_1 = \frac{\lambda_N}{\sqrt{1 + \left(\frac{\lambda_N}{\lambda_r}\right)^2 + i\left(\frac{\lambda_N}{\lambda_m}\right)^2}} . \tag{8.12}$$

It is interesting to note that, even if the injected spin current is polarized in the y direction, a spin accumulation is created with the spins polarized in the x direction, due to both the torque exerted by $\vec{M}$ at the NM/FMI interface (equivalent to the transverse resistance in SMR, explained in section 2.2.2) and the spin precession caused by the magnetic field perpendicular to the spin polarization, and in the z direction only due to the spin precession caused by the magnetic field perpendicular to the spin polarization.

Since the magnetization of the injector and detector are in y direction, only μ_s^y can be detected at $x = L$. From Eq. 8.9 we can determine the non-local resistance measured at the detector [30,32]:

$$R_{NL} = \frac{P_I \mu_s^y(L)}{2eI} , \tag{8.13}$$

where we assume that the polarization at the detector contact is the same as at the injector. By inserting Eq. 8.9 into this last expression we finally obtain

$$R_{NL} = \frac{P_I^2 R_N}{2} \left[\cos^2\alpha e^{-L/\lambda_N} + \sin^2\alpha \mathrm{Re}\left(\frac{\lambda_1}{\lambda_N} e^{-L/\lambda_1} \right) \right] . \tag{8.14}$$

Notice that for $\alpha = 0°$ (*i.e.*, when the magnetic field is parallel to the magnetization of the FM electrodes), the R_{NL} without FMI (Eq. 2.12) is recovered. At $\alpha = 90°$ we obtain a similar expression of R_{NL} as in the $\alpha = 0°$ case, but with a reduced spin-diffusion length $\mathrm{Re}(\lambda_1)$: $R_{NL} = \frac{P_I^2 R_N}{2}\mathrm{Re}\left(\frac{\lambda_1}{\lambda_N}\right) e^{-L/\lambda_1}$.

As seen from Eq. 8.12, two quantities renormalize the spin-diffusion length: the spin-mixing conductance by means of the real term $2\rho_N G_r \lambda_N^2/t_N$, and the imaginary Hanle term $i(\lambda_N/\lambda_m)^2$ originated from the applied field. While the former leads to a reduction of the spin-diffusion length due to the torque exerted by the NM/FMI interface to the spins, the latter causes, in addition, the precession of the spins when the spin polarization and the magnetic field are non-collinear, *i.e.*, the precession of the spins due to the Hanle effect, which will be discussed in detail in section 8.5.

8.5 Contribution of the Hanle effect to the modulation

At a first glance, one might think that the Hanle term could be enough to explain the observed modulation of R_{NL} as a function of α. However, as shown in Fig. 8.4, a field of 250 Oe in the absence of G_r leads to a modulation of R_{NL} (blue dashed line) which is one order of magnitude smaller than the measured one. Increasing the magnetic field would eventually lead to a Hanle effect of the same order as the G_r effect. Nevertheless, our experiment is limited to low magnetic fields ($H < 400$ Oe), to avoid the magnetization of the Co electrodes being affected by the direction of H, and thus the Hanle term will not be dominant.

Furthermore, Fig. 8.5 shows a R_{NL} measurement as a function of α for H values of 250 Oe and 350 Oe. The results are identical, ruling out the possibility of a non-local modulation induced by the Hanle effect.

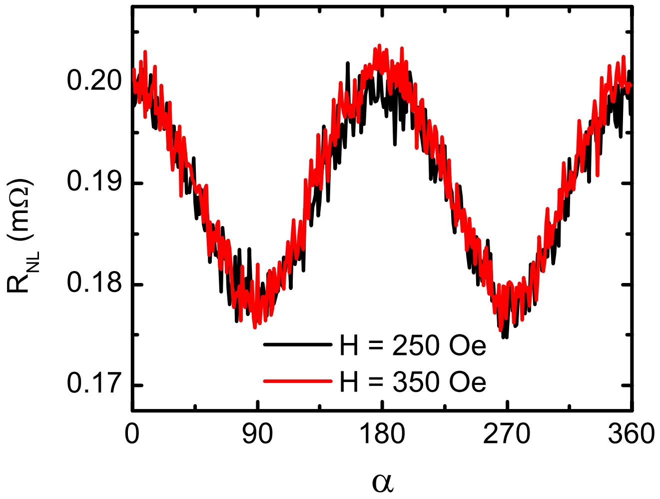

Figure 8.5: R_{NL} as a function of α measured for the P configuration of the FM electrodes, at 150 K, in a LSV with $L = 1.6$ μm. Two measurements have been done for $H = 250$ Oe and $H = 350$ Oe, with identical results.

8.6 Obtaining the spin-mixing conductance of the Cu/YIG interface

Considering both the G_r and Hanle terms, Eq. 8.14 accurately fits the measured R_{NL} (Fig. 8.4), reproducing the observed modulation of the spin current. Note also that Eq. 8.14 reproduces the reflection symmetry between the P and AP configurations, because the product P_I^2 has opposite sign for each configuration. The fact that the modulation is observed in a pure spin current in a metal such as Cu excludes any proximity effect as the origin of the modulation [23, 24], confirming the validity of the G_r concept.

The measured R_{NL} data was fitted to Eq. 8.14 with the parameters G_r and P_I. From the fitting shown in Fig. 8.4 for the LSV with $L = 1.6$ μm, we obtained $P_I = 0.128 \pm 0.001$ and $G_r = (4.28 \pm 0.06) \times 10^{11}$ $\Omega^{-1}\text{m}^{-2}$ for the P state (Fig. 8.4(a)), and $P_I = 0.129 \pm 0.001$ and $G_r = (5.63 \pm 0.07) \times 10^{11}$ $\Omega^{-1}\text{m}^{-2}$ for the AP state (Fig. 8.4(b)), which are almost identical for both magnetic configurations. Therefore, the value of G_r obtained for this particular L is $(4.96 \pm 0.68) \times 10^{11}$ $\Omega^{-1}\text{m}^{-2}$. The same fitting was performed for the LSV with $L = 570$ nm, where it was also possible to measure R_{NL} as a function of α, obtaining $P_I = 0.123 \pm 0.001$ and $G_r = (2.82 \pm 0.66) \times 10^{11}$ $\Omega^{-1}\text{m}^{-2}$.

P_I is slightly lower than the one obtained from NLSV measurements (section 8.2) due to the dispersion of the interface quality between different LSVs. The device with $L = 250$ nm has a higher P_I, which enhances the averaged P_I obtained from the fitting of Eq. 2.13. This is why P_I is left as a free parameter rather than a fixed one, so that Eq. 8.14 accurately fits the data.

G_r is substantially smaller than the values obtained for Pt/YIG (ranging from 1.2×10^{12} $\Omega^{-1}\text{m}^{-2}$ to 6.2×10^{14} $\Omega^{-1}\text{m}^{-2}$) [6–9,14–16], Ta/YIG (4.3×10^{13} $\Omega^{-1}\text{m}^{-2}$) [16] and Au/YIG (between 3.5×10^{13} $\Omega^{-1}\text{m}^{-2}$ and 1.9×10^{14} $\Omega^{-1}\text{m}^{-2}$) [10, 11] either by SMR or spin pumping experiments.

There is a possibility of underestimating G_r if the assumption for Eq. 8.14, $R_I >> R_N$, is not fulfilled. If one allows for an arbitrary value of R_I/R_N, one should take into account the possible backflow of spin current in Eqs. 8.6-8.7. It turns out that the general expression for R_{NL} presented in Eq. 2.18 is also valid in the presence of the FMI layer, if one substitutes λ_m by λ_1 of Eq. 8.12. This result can be used to determine the parameter β using Eq. 8.1. In Fig. 8.6 we show the dependence of β as a function of G_r in both the $R_I >> R_N$ and $R_I = 0$ cases. We see that for the value obtained from our measurements ($\beta \approx 8\%$) G_r is slightly larger (by a factor of ~ 2) in the transparent case. In that case G_r would increase to $\sim 8 \times 10^{11}$ $\Omega^{-1}\text{m}^{-2}$, by considering transparent interfaces, which is still low compared to other NM/YIG interfaces.

Particularities of the grain structure and the growth condition of the evaporated Cu on YIG could also lead to an effective reduction of G_r at the interface. Alternatively, the spin-orbit interaction effects that might exist for Pt/YIG, Au/YIG or Ta/YIG [25] could lead to an overestimation of the obtained G_r in these systems. Such effects are unlikely in Cu/YIG. It is worth noting that the G_r of a NM/YIG interface, for a NM with a negligible spin-orbit coupling, has not been experimentally measured before due to the need of the inverse Spin Hall effect (and thus a high spin-orbit coupling metal) in the experiments made so

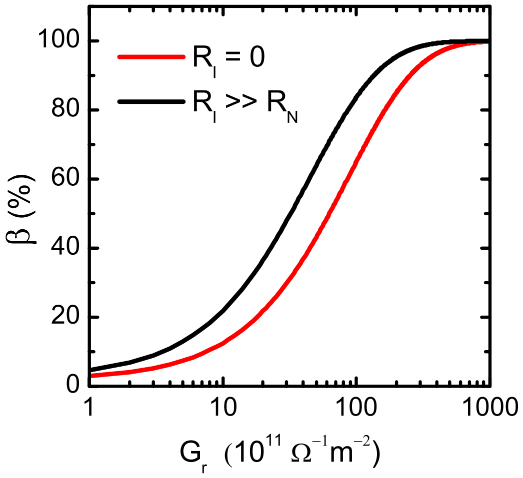

Figure 8.6: β factor as a function of G_r for the $R_I = 0$ and $R_I >> R_N$ cases.

far [6–16].

Another possible reason for the low G_r value could be the Ar-ion milling performed before the Cu deposition [12] or the YIG surface quality. We rule this out by performing a control experiment in Pt/YIG (shown in Appendix 8.C).

8.7 Non-local modulation as a function of temperature

R_{NL} *vs* α measurements were performed for temperatures ranging from 10 K to 200 K for both LSVs with $L = 570$ nm and $L = 1.6$ μm. Fig. 8.7(a) shows the measured data for $L = 570$ nm, where the R_{NL} signal is larger and, thus, the variation is more easily observed. The corresponding non-local modulation δR_{NL} as a function of temperature is plotted in Fig. 8.7. It presents a maximum at 150 K and a sign change at ~ 50 K, which means that below that temperature the non-local modulation is negative (see Fig. 8.7(b)). The unknown origin of this negative sign might be attributed to a local change in the direction of the magnetization, due to the possible roughness of the YIG substrate. The same change of sign at ~ 50 K and a maximum at 150 K is observed in the same Pt/YIG control sample where SMR was measured (see Appendix 8.C). This is an unequivocal observation that both SMR and the non-local modulation of the spin signal have the same origin.

8.8 How to improve magnetic gating

A representation of the β factor, based on Eq. 8.14, is plotted in Fig. 8.8 as a function of different parameters (L, t_N and G_r) which can be controlled in order to improve the efficiency of the magnetic gating. The values of the different parameters used for the representation are listed in the caption and correspond to realistic values taken from our devices. β increases linearly with the length (L) between the FM electrodes, reaching $\sim 30\%$ for $L = 5$ μm (Fig. 8.8(a)). When

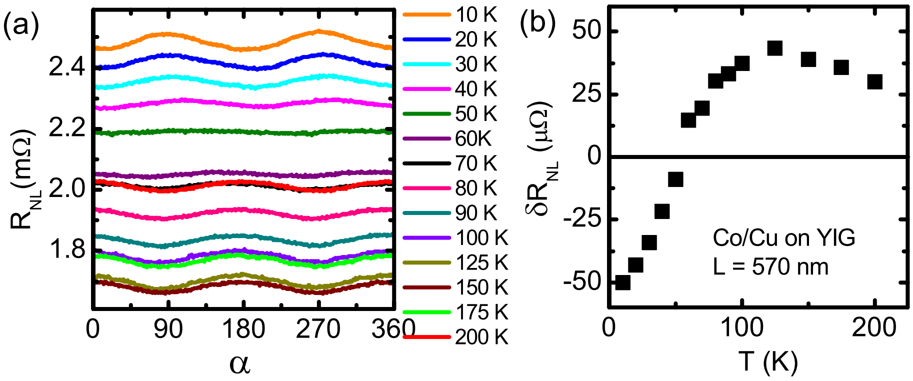

Figure 8.7: (a) R_{NL} as a function of α measured from 10 K to 200 K with $H = 250$ Oe in a LSV with $L = 570$ nm. (b) Its corresponding non-local modulation as a function of temperature.

the spin current flows over a longer distance, the spin scattering and absorption caused by the NM/FMI interface will be enhanced (*i.e.*, β will be larger). This is in agreement with our experimental results discussed above. However, there is an experimental limit, since the non-local signal decays exponentially and will be negligible when $L >> \lambda_N$. By decreasing the thickness (t_N) of the Cu channel, the β factor increases asymptotically when t_N approaches 0 (Fig. 8.8(b)). In this case, by decreasing t_N, the relative contribution of the NM/FMI interface to the spin-flip scattering processes increases, enhancing β. For instance, when $t_N \sim 20$ nm, β already increases to $\sim 50\%$. However, the decrease of λ_N with t_N (section 6.1.2), which has not been taken into account for the representation, will lower β. The most effective way of improving β seems to be increasing G_r (Fig. 8.8(c)). By increasing it by two orders of magnitude, *i.e.*, for a G_r of the order Pt/YIG systems have, β reaches almost up to a 100%, which would lead to a perfect magnetic gating of the pure spin currents. This seems feasible by improving the interface between Cu and YIG or by using another NM material with a high spin-mixing interface conductance with YIG.

8.9 Conclusions

To conclude, we present a new approach to control and manipulate spins in a solid state device, by means of a magnetic gating of pure spin currents in Co/Cu LSV devices on top of YIG. A modulation of the pure spin current is observed as a function of the relative orientation between the magnetization of the FMI and the polarization of the spin current. Such modulation is explained by solving the spin-diffusion equation and considering the spin-mixing conductance at the NM/FMI interface. The accuracy between the measured data and the expected modulation provides an effective way of studying the NM/FMI interface. From our results, a spin-mixing conductance of $G_r \sim 4 \times 10^{11}\ \Omega^{-1}\mathrm{m}^{-2}$ is obtained for the Cu/YIG interface. An increase of this value will enhance the efficiency of the magnetic gating. This can be achieved by carefully tuning the fabrication parameters. Our experiment, thus, paves the way for novel manners of spin manipulation, bringing closer pure spin currents and logic circuits.

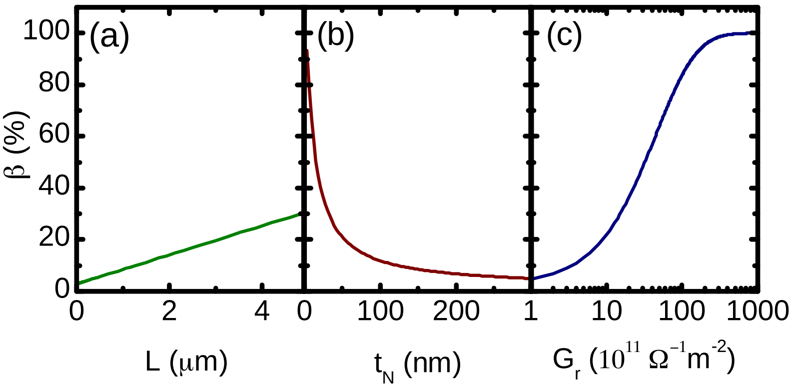

Figure 8.8: Representation (solid lines) of the β factor, based on Eq. 8.14 for an applied magnetic field $H = 250$ Oe, as a function of (a) the distance (L) between FM electrodes, (b) the thickness (t_N) of the NM channel and (c) the spin-mixing conductance (G_r) of the NM/FMI interface. The parameters used for the simulation are: (a) $\lambda_N = 522$ nm, $\rho_N = 2.1$ $\mu\Omega$cm, $G_r = 5 \times 10^{11}$ Ω^{-1}m^{-2} and $t_N = 100$ nm. (b) $\lambda_N = 522$ nm, $\rho_N = 2.1$ $\mu\Omega$cm, $G_r = 5 \times 10^{11}$ Ω^{-1}m^{-2} and $L = 1.6$ μm. (c) $\lambda_N = 522$ nm, $\rho_N = 2.1$ $\mu\Omega$cm, $L = 1.6$ μm and $t_N = 100$ nm.

Appendices

8.A 1st control experiment

In order to exclude a magnetization rotation of the Co electrodes, MOKE microscopy measurements were performed at room temperature directly on the same sample used for the magnetic gating experiment. The capability of the used MOKE microscope to measure the field-induced magnetization reorientation of ultra-small ferromagnetic nanostructures was demonstrated earlier [33]. The MOKE measurements were performed on top of the widest electrode, which is the one whose magnetization can rotate more easily due to shape anisotropy. Given that the thickness of the electrodes (35 nm) is larger than the penetration depth of the light (~15 nm for Co) and that the magneto-optical signal of YIG is one order of magnitude lower than that of Co, the measured signal does not include any contribution from the YIG underneath.

Figure 8.9(a) shows hysteresis loops of the Co electrode (red circles) and of the YIG (black squares), *i.e.*, the projection of the magnetization in the y direction (M_Y), is measured as a function of the magnetic field applied in the y direction, H (with $\alpha = 0°$), and normalized to the saturation magnetization (M_S). In both cases, the MOKE signal was acquired from a subset of the pixels of the CCD detector that corresponds to an area on the sample surface equal to 100 × 800 nm^2 [33]. The coercive field of the Co electrode is 500 Oe, in agreement with the R_{NL} measurements as a function of H shown in Fig. 8.3(c). For the YIG substrate, magnetic saturation around 100 Oe is observed, in agreement with the VSM measurements shown in Fig 8.3(a).

To check for a possible rotation of the magnetization of the Co electrode, its M_Y/M_S was measured while the direction of the magnetic field H, which

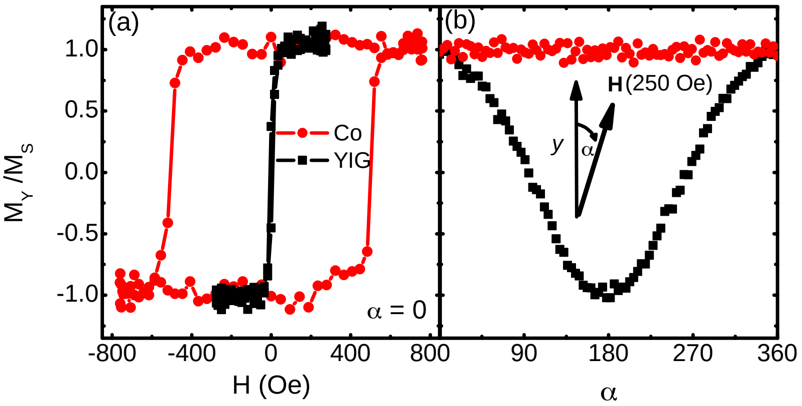

Figure 8.9: (a) Projection of the magnetization in the y direction (M_Y) of the YIG (black squares and line) and of the Co electrodes (red circles and line) normalized to the saturation magnetizations (M_S) measured as a function of the magnetic field H applied in the y direction. (b) M_Y of the YIG (black squares) and of the Co electrodes (red circles) normalized to M_S measured as a function of the angle α between the direction of the Co electrodes (y) and the applied magnetic field, $H = 250$ Oe. Measurements are performed at 300 K.

had a fixed intensity of 250 Oe, was rotated by α, which varied from 0 to 360°. Figure 8.9(b) shows M_Y/M_S of the Co electrode and the YIG substrate. Whereas the magnetization of YIG coherently rotates with the direction of H ($M_Y/M_S \propto \cos\alpha$), given that H is largely exceeding the saturation field of YIG, the magnetization of the Co electrode is constant for every α. Based on the signal-to-noise ratio of our measurements, the smallest detectable change in M_Y/M_S corresponds to a rotation of M_s of less than 5°. Therefore, we can directly conclude that the rotation of the Co magnetization, if any, is less than 5°, which could only explain a variation of less than 0.4% in R_{NL}, well below the experimentally observed ~8%.

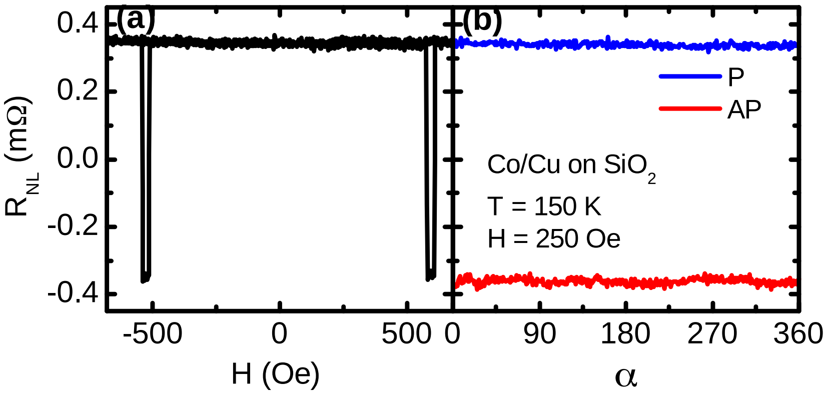

Figure 8.10: (a) R_{NL} measured at 150 K as a function of H with $\alpha = 0°$ for a Co/Cu LSV fabricated on top of SiO$_2$. (b) R_{NL} as a function of α, measured for both the P and AP configuration, at 150 K with H=250 Oe for the same LSV.

8.B 2$^{\text{nd}}$ control experiment

Even though a possible rotation of the FM electrodes is excluded with the previous control experiment (section 8.A), an additional control experiment was performed in order to rule out any other possible artifact. With this purpose, the main experiment was repeated in a LSV fabricated on top of SiO_2 instead of YIG. Fig. 8.10(b) shows R_{NL} measured as a function of α for both the parallel (P) and antiparallel (AP) magnetizations of the FM electrodes with $H = 250$ Oe. As observed in the figure, no periodic modulation of R_{NL} is measured. The noise of the measurements is around 0.015 mΩ, which means that if there is any modulation of R_{NL} it will be certainly smaller than 2% (notice that the measured spin signal is 0.7 mΩ, as seen in Fig. 8.10(a)). This value is smaller than the values of $\beta = 2.96\%$ and $\beta = 8.33\%$ we have observed, which excludes any possible artifact and attributes the measured modulation in R_{NL} solely to the spin-mixing conductance at the NM/FMI interface.

8.C 3$^{\text{rd}}$ control experiment

In order to see if the low G_r value obtained for Cu/YIG interfaces originates from the quality of the YIG substrate or from any effect that might be induced at the YIG substrate for the Ar-ion milling process, we fabricated a Pt/YIG control sample and tested it within the SMR framework [14–18], as explained in section 2.2.2.

With this purpose, a 7-nm-thick Pt Hall bar (with a width $w = 100$ μm and a length $l = 800$ μm) was sputtered on top of a YIG substrate grown as the one used for the fabrication of the LSV. Prior to the Pt deposition, the YIG surface was subjected to the same Ar-ion milling process of 30 s (section 3.1). Angular dependent magnetoresistance (ADMR) measurements were performed by rotating a fixed H along the three main rotation planes of the system: XY, YZ and XZ, with the corresponding angles α, β and γ. A large enough H is applied to ensure the magnetization of the YIG substrate follows the direction of the applied magnetic field. The resistance was measured using both longitudinal (R_L) and transverse (R_T) configurations, yielding to results very similar to those shown in Fig. 2.6. As expected from the SMR theory (section 2.2.2) [14, 17]: (*i*) no modulation is observed in $R_L(\gamma)$, (*ii*) a large modulation is observed in $R_L(\alpha)$ and $R_L(\beta)$, with the same amplitude and a $\cos^2$ dependence, and (*iii*) $R_T(\alpha)$ shows a $\sin\alpha \cdot \cos\alpha$ dependence, with the same amplitude as in $R_L(\alpha)$ but with a l/w factor.

With the measured longitudinal resistance of $R_L = 281.5$ Ω at 150 K, one can determine $\rho_0 = 24.7$ $\mu\Omega$ cm and the SMR signal $\Delta\rho/\rho_0 = 5.48 \times 10^{-5}$. Knowing the values of θ_{SH} and λ_N in Pt, one can extract the G_r value of the Pt/YIG interface using Eq. 2.22. These values cannot be inferred from our measurements, but can be obtained from literature. Despite there is a big dispersion of the given values for θ_{SH} and λ [14,34,35], we will use the ones recently reported in Ref. [35] ($\theta_{SH} = 0.056$ and $\lambda = 3.4$ nm), since they are highly consistent within different methods used to determine them. A $G_r = 3.4 \times 10^{13}$ $\Omega^{-1}m^{-2}$ is obtained for our Pt/YIG interface, which is in agreement with the previously reported range of

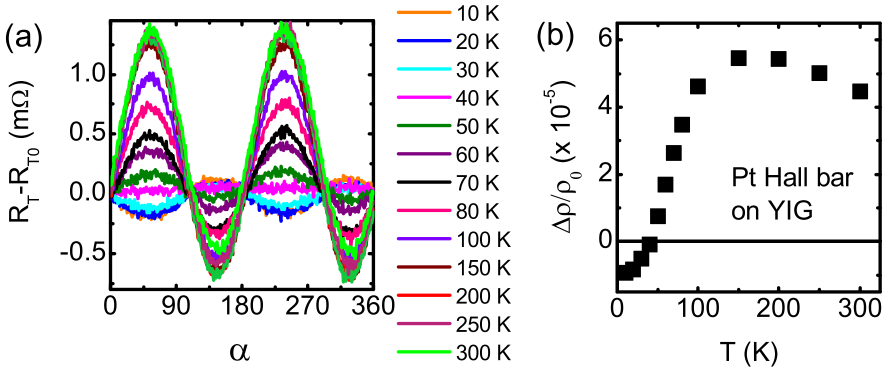

Figure 8.11: (a) Transverse resistance (R_T) as a function of α measured from 10 K to 300 K for $H = 1$ kOe. A small spurious baseline resistance R_{T0} was subtracted. (b) Its corresponding magnetoresistance ($\Delta\rho/\rho_0$) as a function of temperature.

values [6–9, 14–16]. We can take this result as a proof of the good quality of the YIG substrates used in the present experiments and as an indication that the Ar-ion milling process in the LSV experiment is not at the origin of the low G_r obtained.

The transverse resistance $R_T(\alpha)$ was measured at temperatures ranging from 10 K to 300 K in the same device (Fig. 8.11(a)). As observed in Fig. 8.11(b), the SMR signal $\Delta\rho/\rho_0$ is maximum at 150 K and its sign changes below 50 K, which is the same behavior observed for the non-local modulation of the LSVs on top of YIG.

References

[1] B. Behin-Aein, D. Datta, S. Salahuddin, and S. Datta, Nat. Nanotech. **5**, 266 (2010).

[2] S. Datta and B. Das, Appl. Phys. Lett. **56**, 665 (1990).

[3] H. C. Koo, J. H. Kwon, J. Eom, J. Chang, S. H. Han, and M. Johnson, Science **325**, 1515 (2009).

[4] A. Brataas, Y. V. Nazarov, and G. E. W. Bauer, Phys. Rev. Lett. **84**, 2481 (2000).

[5] A. Braatas, Y. V. Nazarov, and G. E. W. Bauer, Eur. Phys. J. B **22**, 99 (2001).

[6] M. Weiler, M. Althammer, M. Schreier, J. Lotze, M. Pernpeintner, S. Meyer, H. Huebl, R. Gross, A. Kamra, J. Xiao, Y.-T. Chen, H. Jiao, G. E W. Bauer, and S. T. B. Goennenwein, Phys. Rev. Lett. **111**, 176601 (2013).

[7] Y. Kajiwara, K. Harii, S. Takahahi, J. Ohe, K. Uchida, M. Mizuguchi, H. Umezawa, H. Kawai, K. Ando, K. Takanashi, S. Maekawa, and E. Saitoh, Nature **464**, 262 (2010).

[8] L. Qiu, K. Ando, K. Uchida, Y. Kajiwara, R. Takahashi, H. Nakayama, T. An, Y. Fujikawa, and E. Saitoh, Appl. Phys. Lett. **103**, 092404 (2013).

[9] V. Castel, N. Vlietstra, B. J. van Wees, and J. B. Youssef, Appl. Phys. Lett. **101**, 132414 (2012).

[10] B. Heinrich, C. Burrowes, E. Montoya, B. Kardasz, E. Girt, Y.-Y- Song, Y. Sun, and M. Wu, Phys. Rev. Lett **107**, 066604 (2011).

[11] C. Burrowes, B. Heinrich, B. Kardasz, E. A. Montoya, E. Girt, Y. Sun, Y.-Y. Song, and M. Wu, Appl. Phys. Lett. **100**, 092403 (2012).

[12] M. B. Jungfleisch, V. Lauer, R. Neb, A. V. Chumak, and B. Hillebrands, Appl. Phys. Lett. **103**, 022411 (2013).

[13] K. Uchida, J. Xiao, H. Adachi, J. Ohe, S. Takahashi, J. Ieda, T. Ota, Y. Kajiwara, H. Umezawa, H. Kawai, G. E. W. Bauer, S. Maekawa, and E. Saitoh, Nat. Mater. **9**, 894 (2010).

[14] H. Nakayama, M. Althammer, Y.-T- Chen, K. Uchida, Y. Kajiwara, D. Kikuchi, T. Ohtani, S. Geprägs, M. Opel, S. Takahashi, R. Gross, G. E. W. Bauer, S. T. B. Goennenwein, and E. Saitoh, Phys. Rev. Lett. **110**, 206601 (2013).

[15] N. Vlietstra, J. Shan, V. Castel, and B. J. van Wees, Phys. Rev. B **87**, 184421 (2013).

[16] C. Hahn, G. de Loubens, O. Klein, M. Viret, V. V. Naletov, and J. Ben Youssef, Phys. Rev. B **87**, 174417 (2013).

[17] Y.-T. Chen, S. Takahashi, H. Nakayama, M. Althammer, S. T. B. Goennenwein, E. Saitoh, and G. E. Bauer, Phys. Rev. B **87**, 144411 (2013).

[18] M. Isasa, A. Bedoya-Pinto, F. Golmar, F. Sánchez, L. E. Hueso, J. Fontcuberta, and F. Casanova, Appl. Phys. Lett. **105**,142402 (20014).

[19] S. O. Valenzuela and M. Tinkham, Nature **442**, 176 (2006).

[20] J. C. Slonczewski, J. Magn. Magn. Mater. **159**, L1 (1996); L. Berger. Phys. Rev. B **54**, 9353 (1996).

[21] D.C. Ralph and M. D. Stiles, J. Mag. Magn. Mater. **320**, 1190 (2008).

[22] X. Jia, K. Liu, K. Xia, and G. E. Bauer, Europhys. Lett. **96**, 17005 (2011).

[23] S. Y. Huang, X. Fan, D. Qu, Y. P. Chen, W. G. Wang, J. Wu, T. Y. Chen, J. Q. Xiao, and C. L. Chien, Phys. Rev. Lett. **109**, 107204 (2012).

[24] Y. M. Lu, J. W. Cai, S. Y. Huang, D. Qu, B. F. Miao, and C. L. Chien, Phys. Rev. B **87**, 220409 (2013).

[25] A. B. Cahaya, O. A. Tretiakov, and G. E. W. Bauer, Appl. Phys. Lett. **104**, 042402 (2014).

[26] Y. Ji, A. Hoffmann, E. Pearson, and S. D. Bader, Appl. Phys. Lett. **88**, 052509 (2006).

[27] F. J. Jedema, H. B. Heersche, A. T. Filip, J. J. A. Baselmans, and B. J. van Wees, Nature **416**, 713 (2002).

[28] X. J. Wang, H. Zou, and Y. Ji, Phys. Rev. B **81**, 104409 (2010).

[29] H. Zou, S. T. Chui, X. J. Wang, and Y. Ji, Phys. Rev. B **83**, 094402 (2011).

[30] S. Takahashi and S. Maekawa, Phys. Rev. B **67**, 052409 (2003).

[31] Y. Fukuma, L. Wang, H. Idzuchi, S. Takahashi, S. Maekawa, and Y. Otani, Nat. Mater. **10**, 527 (2011).

[32] M. Popinciuc, C. Jozsa, P. J. Zomer, N. Tombros, A. Veligura, H. T. Jonkman, and B. J. van Wees, Phys. Rev. B **80**, 214427 (2009).

[33] E. Nikulina, O. Idigoras, P. Vavassori, A. Chuvilin, and A. Berger, Appl. Phys. Lett. **100**, 142401 (2012).

[34] L. Liu, R. A. Buhrman and D. C. Ralph, arXiv: 1111.3702.

[35] J.-C. Rojas-Sánchez, N. Reyren, P. Laczkowski, W. Savero, J.-P. Attané, C. Deranlot, M. Jamet, J.-M. George, L. Vila, and H. Jaffrèès, Phys. Rev. Lett.**112**, 106602 (2014).

Chapter 9

Conclusions and future perspectives

This thesis presents a complete research work devoted to spin injection, transport and manipulation in metals. Such comprehensive study was possible by using lateral spin valves. The high reproducibility of our process to nanofabricate these devices allowed us to systematically compare properties between different samples, as well as present reference values of the spin polarization of FM metals (α_F) and the spin-diffusion length of Cu (λ_{Cu}).

We were able to study the spin-injection properties of Co and Py and to prove that the spin transport properties of Cu are not affected by the election of the FM material. By obtaining α_F as a function of temperature, we showed that the spin polarization of a FM is given by the standard two-channel model, although a correction factor of ~ 2 is detected.

The analysis of resistivity and spin-diffusion length as a function of temperature and thickness in Cu nanowires identified different temperature dependent and independent spin scatterers and attributed the defect scattering to the grain boundaries rather than the surface. In addition, it helped solving the long standing puzzle of the unexpected behavior of λ_{Cu} at low temperatures, by explaining it with the presence of magnetic impurities in the bulk Cu. These results are crucial for an improvement of the spin transport, one of the key points in the operation of a second generation of spintronic nanodevices.

In the same direction, spin manipulation experiments were performed by means of the Hanle effect. Whereas an effective modulation of the non-local resistance was observed by applying an out-of-plane magnetic field, interference effects were identified beyond the current theory.

Finally, a novel approach for spin manipulation was presented, by taking advantage of the NM/FMI interface spin-mixing conductance concept. A magnetic gating of pure spin currents was achieved following this approach. The underlying phenomenon was explained with a solid theoretical ground and, in addition, the value of the Cu/YIG interface spin-mixing conductance was obtained, which can be improved by carefully tuning the fabrication parameters.

We believe that all the results presented throughout this thesis are of great interest for the large spintronics and magnetism community, disclose some fundamental aspects and will surely guide new experiments and further developments. In particular, this research paves the way for novel manners of spin manipulation, bringing closer pure spin currents and logical circuits.

In a next stage, taking advantage of the acquired knowledge, some particular steps can be taken in the direction of improving the performance of the LSVs.

Regarding spin injection, new materials with a higher intrinsic spin polarization can be used, such as half metals, which have a 100% spin polarization at the Fermi level. An example of these materials are the Heusler alloys, which have been already used as FM electrodes in LSVs [1,2], observing a $>$ 10-fold enhancement of the spin signal. A different approach could be the use of FM materials with a higher electrical resistivity, which could be done by using FM metals with a low purity, reducing the backflow of spins and enhancing the spin-injection efficiency.

The spin transport in the NM channel can also be improved by reducing the magnetic impurities as well as the grain boundaries in the NM material, which, as indicated by our results, would result in an increase of the spin-diffusion length.

For optimizing the spin manipulation, it is important to first understand where the observed interference in the Hanle effect comes from. This way, the spin manipulation by applying an out-of-plane magnetic field can be better controlled, from where reliable information can be obtained.

Finally, in Chapter 8 we already mention different parameters that would lead to an enhancement of the magnetic gating of the pure spin currents and of the current modulation β. The most straightforward seems to be the increasing of the NM/FMI interface spin-mixing conductance, G_r, which can be obtained by tuning the Cu/YIG interface properties or by using another NM material which will give a higher G_r with YIG. The increase of β when reducing the thickness of the NM material t_N should also be investigated; although, in the case of metals, λ_N decreases with t_N, it is worth studying the magnetic gating of pure spin currents in LSVs containing 2D materials, such as graphene, as the NM channel. The ultimate goal in spin manipulation is the electric gating of the spin currents. By means of magnetoelectric coupling, electric control of the magnetic gate could be achieved, which would lead to the long sought spin transistor.

References

[1] K. Hamaya, N. Hashimoto, S. Oki, S. Yamada, M. Miyao, and T. Kimura, Phys. Rev. B **85**, 100404(R) (2012).

[2] G. Bridoux, M. V. Costache, J. Van de Vondel, I. Neumann, and S. O. Valenzuela, Appl. Phys. Lett. **99**, 102107 (2011).

10. List of publications

This thesis is based on the following publications:

1. *Contribution of defects to the spin relaxation in copper nanowires*,
   Estitxu Villamor, Miren Isasa, Luis E. Hueso, and Fèlix Casanova,
   Phys. Rev. B **87**, 094417 (2013).
   (Chapter 6)

2. *Temperature dependence of spin polarization in ferromagnetic metals using lateral spin valves*,
   Estitxu Villamor, Miren Isasa, Luis E. Hueso, and Fèlix Casanova,
   Phys. Rev. B **88**, 184411 (2013).
   (Chapters 4, 5 and 6)

3. *Magnetic gating of pure spin currents*,
   Estitxu Villamor, Miren Isasa, Saül Vélez, Amilcar Bedoya-Pinto, Paolo Vavassori, Luis E. Hueso, F. Sebastián Bergeret, and Fèlix Casanova,
   Submitted to Phys. Rev. Lett. (arXiv:1404.2311).
   (Chapter 8)

4. *Effect of the interface resistance in non-local Hanle measurements*,
   Estitxu Villamor, Luis E. Hueso, and Fèlix Casanova,
   In preparation.
   (Chapter 7)

Other publications:

5. *Embedded purification for electron beam induced Pt deposition using MeCpPtMe3*,
   E. Villamor, F. Casanova, P. H. F. Trompenaars, and J. J. L. Mulders,
   Submitted to Nanotechnology.

6. *Temperature dependence of spin diffusion length and spin Hall angle in Au and Pt* ,
   Miren Isasa, Estitxu Villamor, Luis E. Hueso, Martin Gradhand, and Fèlix Casanova,
   Submitted to Phys. Rev. B (arXiv:1407.4770).

7. *Detection of inverse Rashba-Edelstein effect at Cu/Bi interface using lateral spin valves*,
   Miren Isasa, M. Carmen Martínez-Velarte, Estitxu Villamor, Luis Morellón, José M. De Teresa, Manuel R. Ibarra, Luis E. Hueso, and Fèlix Casanova,
   Submitted to Phys. Rev. Lett. (arXiv:1409.8540).

8. *Spin transport enhancement by controlling the Ag growth in lateral spin valves*,
   Miren Isasa, Estitxu Villamor, Lorenzo Fallarino, Olatz Idigoras, Anna K. Suszka, Christopher Tollan, Andreas Berger, Luis E. Hueso, and Fèlix Casanova,
   Submitted to J. Phys. D: Appl. Phys. (arXiv:1410.4001).

9. *Focused electron beam induced deposition of cobalt: secondary electron corrected model and advanced characterization*,
   M.-J. Perez-Roldan, E. Nikulina, O. Idigoras, E. Villamor, F. Casanova, P. Vavassori, H. Mulders, A. Berger, and A. Chuvilin,
   In preparation.

11. Acknowledgements

I do not have enough words to thank my supervisor, Fèlix, for believing in me and for his constant support and guidance throughout these years: although we have not always agreed, overall, I think you have been a great supervisor. I feel lucky because you have always kept in mind that your work was to teach me and you made me feel, specially during this last period, that we were a team. Moltes gràcies!

Thanks also to Luis, it is because of you that I am in the *nanodevices* group, since I did that summer internship in 2009 (so long ago...). I can definitely say that you believed in me, too, and taught me really important lessons.

I would like to thank Prof. Txema Pitarke, the director of CIC nanoGUNE, for giving me the opportunity of carrying out my work here. I would have never imagined this in my first year of university, when you taught me elementary physics.

Not a single experiment described in this thesis could have been done without the help of our technician, Rutx (Super Llopis)! Thanks for all your help in the lab, all the hours we spent together (in and out of work) and for putting a smile in my face almost every time I see you. Ez duzu bazkalduko gaur?

I would also like to thank Dr. Sebastián Bergeret for his support with the theory, which turned out to be an important part of this thesis. Thanks for your enthusiasm and for reminding me the beauty of the physics as a whole, when experiments and theory agree so well. I really enjoyed this last part of my research.

To all the (current and former) members of the *nanodevices* group, it was a real pleasure to work with you: Mariana, Subir, Mario, Pablo, Wenjing, Luca, Amilcar, Saulillo, Dr. Zazpe, Ainhoa, Edurne, Dr. Sun, Mano, Conde de Valdepeñas, Dr. Gobbi, Boludo, Laif and very specially to Miren and Oihana (thanks *angels* for all those laughs, cries, gossips... all those beautiful, crazy, sad, funny and profound moments that we shared!).

Thanks to all the technicians from nanoGUNE for you help in the labs and the moments outside the labs, specially at lunch-time: Gorka, Ralph, Chris, Aitziber, Charly, Garbayo (you are like a technician to me), Amaia, Oulatz, Cesar Antonio, Maritxu...

To the people surrounding me: Karmon, David, Mikel, Roger again... for those stupid Friday afternoons (and Mondays, Tuesdays, Wednesdays and Thursdays!) and for making me laugh so loud that it could be heard from the other side of the offices.

To Joni and Paulo, I'm really proud of the journey that the three of us traveled together since September 2005 (*annus mirabilis*).

Joni, you need to be acknowledged twice (or maybe three, four... a hundred

times) for being the best flatmate (together with Jokintroniks!) I could have during my years in Donosti. We shared so many things in this period and I feel you are one of my best friends now, which is much more important than any thesis.

In reality, I should thank all the nanoGUNE and Graphenea people (Jacqueline, you know you are included in the nanopeople!) for making me want to go to work every day, for the parties out of work and for making my PhD years such an intense experience. I would like to say something special about each of you, cause each of you is really special to me!

I would also like to thank the people from Grenoble, for what I learned there and for making me feel at home during my short stay: Laurent, Will, Carlos, Celine, Murat, Matthieu, Jean-Philippe... merci beaucoup!

To Rosa, thanks for making me remember the time in Eindhoven with a smile in my face. You know I admire you and I wish you the best luck and tons of love, because that's what you deserve!

Prof. Hans Peter Oepen also needs to be acknowledged. I really appreciate that you accepted reading this thesis and giving me your feedback for the international PhD mention.

Thanks to the Basque Government for the program ”Programas de ayudas para formación y perfeccionamiento de personal investigador”, responsible for my PhD grant. I hope they can form a lot of generations of scientists.

Nire lagun minek (*Kuadrilla power!* Jacqueline, a tí también te debería incluir aquí ocasionalmente... ;)) ere aipamen berezia merezi dute: Aini, Moren, Aintz, Hodi, Mai eta Di, badakit (nik bezala pentsatzen duzuelako) badakizuela zelako zortea dudan zuek bezalako lagun batzuk izateaz, Koldo-ko garaietatik nigan sinetsi dutenak! Mila esker neskak (eta mutil)! Onenak zarete! :)

Azkenik, esker berezienak nire gurasoentzako dira, nola ez! Patxiko eta Milika, zuen babesari esker beti sentitu izan dut egiten nuen guztia (profesionalki zein pertsonalki) ondo zegoela, ta hori jende ugarik ezin du esan! Izugarri maite zaituztet!